On the relevance of rotational and divergent modes of motion to mesoscale dynamics and upscale error growth

Lotte Beata Bierdel

München 2017

On the relevance of rotational and divergent modes of motion to mesoscale dynamics and upscale error growth

Lotte Beata Bierdel

Dissertation
an der Fakultät für Physik
der Ludwig–Maximilians–Universität
München

vorgelegt von
Lotte Beata Bierdel
aus Bensheim

München, 15. Mai 2017

"Among the innumerable processes which take place in the universe, there are many whose future behavior we often wish to predict."

E. Lorenz (1963), *The predictability of hydrodynamic flow*

Parts of this thesis are contained in:

L. Bierdel, C. Snyder, S.-H. Park and W. C. Skamarock (2016):
"Accuracy of rotational and divergent kinetic energy spectra diagnosed from flight track winds", *J. Atmos. Sci.*, 73, 3273-3286

Zusammenfassung

Die atmosphärischen Mesoskalen beinhalten dynamische und thermodynamische Prozesse, die durch Längenskalen von einigen bis zu einigen hundert Kilometern und Zeitskalen von Minuten bis zu einem Tag charakterisiert werden. Atmosphärische Strömungen auf diesem Skalenbereich werden als Wetter der mittleren Breiten verstanden und ihre verlässliche Vorhersage ist ein Hauptziel meteorologischer Forschung. Dabei treten zwei grundlegende Probleme auf: Erstens besteht kein Konsens darüber, welcher Prozess die mesoskalige Dynamik dominiert und insbesondere dem beobachteten horizontalen kinetischen Energiespektrum zugrunde liegt. Zweitens konnte bisher kein dominanter Skalenwechselwirkungsmechanismus bestimmt werden, auf dem das Anwachsen zunächst kleinskaliger Fehler zu großen Skalen basiert. Die vorliegende Dissertation trägt zu einem verbesserten Verständnis dieser beiden Aspekte bei, wobei der Fokus auf dem relativen Beitrag rotationeller und divergenter Moden des horizontalen Geschwindigkeitsfeldes und deren Wechselwirkung liegt.

Eine fundamentale Überprüfung existierender Theorien bezüglich des horizontalen mesoskaligen Energiespektrums wird durch die Aufspaltung eindimensionaler atmosphärischer Windmessungen in rotationelle und divergente Anteile ermöglicht. Eine dementsprechende eindimensionale Helmholtz-Zerlegungsmethode wurde kürzlich veröffentlicht. Diese Aufspaltung basiert auf den mathematischen Annahmen der Homogenität und Isotropie, deren Gültigkeit im ersten Teil der vorliegenden Dissertation getestet wird. Dazu werden neue, hochaufgelöste globale numerische Simulationen der Atmosphäre verwendet. Die rotationellen- und divergenten Strömungsanteile werden mit der Helmholtz-Zerlegungsmethode aus eindimensionalen Segmenten des Windfeldes abgeleitet. Diese werden dann mit den rotationellen und divergenten Beiträgen des zweidimensionalen Windfeldes, welche als Referenz verwendet werden, verglichen. Die mathematischen Annahmen der eindimensionalen Helmholtz-Zerlegungsmethode sind auf den Mesoskalen hinreichend gut erfüllt, so dass hier das mesoskalige Verhältnis rotationeller zu divergenten Geschwindigkeitsmoden korrekt reproduziert werden kann. Beide Anteile des horizontalen Windfeldes zeigen des Weiteren eine signifikante Abhängigkeit von dem betrachteten Höhen- und Breitengradbereich. Die Ergebnisse deuten darauf hin, dass die mesoskalige Dynamik und das damit verbundene horizontale kinetische Energiespektrum nicht universell sind.

Aktuelle Studien zeigen, dass das schnelle Anwachsen kleinskaliger Fehler in numerischen Wettervorhersagen vor allem mit der konvektiven Instabilität und dem Freisetzen latenter Kondensationswärme in Wolken zusammenhängt. Während die Fehler auf größere Skalen expandieren, ändert sich die dominante Dynamik von signifikant divergent zu primär rotationell. Der zweite Teil dieser Dissertation erforscht, ob diesem dynamischen Übergang die

geostrophische Anpassung nach dem Einsetzen von Feuchtkonvektion zugrunde liegt. Dabei wird sowohl ein analytischer- als auch ein numerischer Ansatz verfolgt. Zunächst wird ein analytisches Modell für die geostrophische Anpassung einer instantanen Wärmefreisetzung (repräsentativ für den Fehler innerhalb der Vorhersage einer Wolke) entwickelt. Die gefundene Lösung ist die Greensche Funktion der betrachteten linearisierten, hydrostatischen Boussinesq-Gleichungen und enthält explizit die zeitliche Entwicklung aller transienten und balancierten Strömungsanteile. Die charakteristischen Raum- und Zeitskalen des geostrophischen Anpassungsprozesses werden aus dieser Lösung bestimmt. Ferner werden drei Diagnostiken entwickelt, mithilfe derer dieser Mechanismus in numerischen Simulationen identifiziert werden kann. Die analytischen Ergebnisse werden danach mit Fehlerwachstumsexperimenten in idealisierten numerischen Simulationen eines konvektiven Wolkenfeldes in einer rotierenden Umgebung getestet. Die gefundenen Eigenschaften des Fehlerwachstums stimmen sehr gut mit den Vorhersagen des analytischen Modells überein. Damit unterstützen die Ergebnisse dieser Dissertation die Hypothese, dass die geostrophische Anpassung konvektiver Wärmefreisetzung das Fehlerwachstum durch die atmosphärischen Mesoskalen bestimmt.

Abstract

The atmospheric mesoscales encompass dynamical and thermodynamical processes that are characterized by length scales between a few and a couple of hundred kilometers and temporal scales of several minutes to one day. These processes are associated with mid-latitudinal weather and their skillful prediction is a major aim of meteorological research. In there, two fundamental issues arise: first, there is no consensus about the principal dynamical agent on the mesoscales that gives rise to the observed kinetic energy spectrum. Second, a dominant scale-interaction mechanism that governs the growth of initially small-scale errors to large scales remains undetermined. This thesis contributes to an improved understanding of these two aspects with an emphasis on the relevance of rotational and divergent modes of motion and their interplay.

An important observational test of theoretical studies regarding the horizontal mesoscale kinetic energy spectrum is decoupling its rotational and divergent constituents from one-dimensional atmospheric wind measurements. Such a one-dimensional Helmholtz-decomposition method was recently suggested. The first part of this dissertation addresses the validity of the strong mathematical homogeneity and isotropy assumptions underlying this method. To that end, new high-resolution global atmospheric numerical simulations are employed. Rotational and divergent modes of motion are derived by applying the one-dimensional Helmholtz-decomposition method to one-dimensional transects of the horizontal wind field. The results are then compared to the divergent and rotational components obtained from the unambiguous decomposition of the two-dimensional wind field. The mathematical assumptions are found to be fulfilled such that the mesoscale ratio of divergent to rotational kinetic energy can be derived correctly with the one-dimensional Helmholtz-decomposition method. The results suggest a significant dependence of the horizontal divergent- and rotational kinetic energy spectra on the considered height- and latitude ranges. This finding points to the non-universality of the dynamics governing the mesoscale kinetic energy spectrum.

Recent studies suggest that small-scale errors in numerical weather predictions quickly amplify through the convective instability and the release of latent heat of condensation within clouds. These errors then propagate to larger scales, whereby their dynamics transition from significantly divergent to mainly rotational. The second part of this dissertation explores the possibility that geostrophic adjustment following deep moist convection is the dominant dynamical process governing this transition with an analytical- and a numerical approach. An analytical framework for the geostrophic adjustment of an initial point-like pulse of heat (representing the error within the prediction of a cloud) is developed based on the linearized, hydrostatic Boussinesq-equations. The solution includes the Green's function of the problem

and contains the full temporal evolution of all transient and balanced flow components. Characteristic spatial and temporal scales of the geostrophic adjustment mechanism are deduced and three diagnostics that can be used to identify this process in numerical simulations are proposed. These predictions are then tested in the framework of error growth experiments in highly idealized numerical simulations of a convective cloud field in a rotating environment. The error growth characteristics feature a high level of agreement with the analytical predictions. The results of this thesis suggest that the geostrophic adjustment following convective heating governs upscale error growth through the atmospheric mesoscales.

Contents

Chapter 1

Introduction

1.1   Scales of atmospheric motion

The earth's atmosphere is a nonlinear, chaotic dynamical system where a variety of dynamical and thermodynamical processes of different spatial- and temporal scales interact. From a global perspective, the whole spectrum of atmospheric motion encompasses 10 orders of magnitude in horizontal length scales (from the mean free path length scale to the earth's circumference) and 20 orders of magnitude in temporal scales (from the dissipation timescale to the age of the earth) (Emanuel, 1986). This multi-scale character of atmospheric flow can for example be anticipated from satellite images (see Fig. 1.1). The different modes of atmospheric motion manifest themselves in cloud structures of varying horizontal scale $\mathcal{L}_h$ (e.g. relatively large-scale cloud-band associated with ascending air in warm-sector of cyclone Vladiana, convection of notably smaller horizontal scale over the free ocean to the West of the storm). Atmospheric processes of different scales $\mathcal{L}_h$ are associated with temporal scales $\mathcal{T}$ and their ratio gives the associated velocity scale $\mathcal{V}$.

In Fig. 1.2, various atmospheric modes of motion are displayed with the associated temporal and spatial scales. Note that in this work mainly processes in the troposphere will be considered. The troposphere is the vertical atmospheric layer ranging from the ground to the tropopause in 7 to 20 km altitude. It is characterized by a decrease in temperature with height and almost all weather relevant dynamic processes take place within that layer. Processes from upper layers play a minor role in weather dynamics and will be referred to if necessary. The velocity scale $\mathcal{V}$ of atmospheric dynamical processes is shown to take a somewhat universal value over a wide range of temporal and spatial scales, indicating that $\mathcal{L}_h$ and $\mathcal{T}$ are not independent (i.e. phenomena of large horizontal spatial scale feature a large temporal scale and vice versa).

Historically, different approaches have been introduced to define classes of spatial and temporal scales of the continuous spectrum of dynamical atmospheric phenomena (e.g. sizes/resolution of observational networks, theoretical inferences and observations of atmospheric phenomena; for a detailed discussion see Emanuel, 1986). In the following, the general classification of atmospheric motion into micro-, meso- and macro-scales (and associated α-, β- and γ-subranges put forward by Orlanski, 1975) will be employed. Note that while processes attributed to
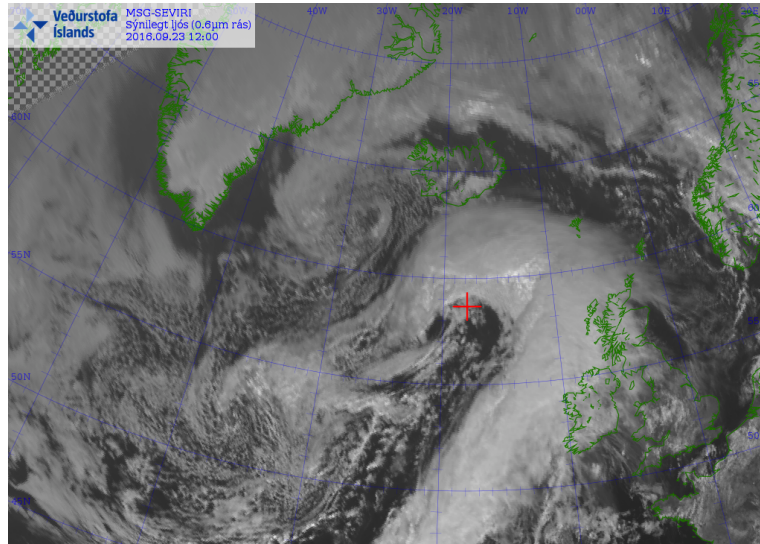
Figure 1.1: Meteosat Second Generation (MSG) Spinning Enhanced Visible and InfraRed Imager (SEVIRI) image in the visible 0.6 μ m channel. Storm *Vladiana* (center indicated with red cross) located in the North Atlantic region on September 23 2016 12 UTC (`http://brunnur.vedur.is`, courtesy of the Icelandic MetOffice and EUMETSAT).

either the micro-, meso- or macro-scale preferably occur on different atmospheric heights, motions on all three scales can in principle feature different characteristic vertical length scales rendering a general scale separation in the vertical unfeasible (Fiedler and Panofsky, 1970).

The microscale is the small-scale end of the displayed spectrum (Fig. 1.2) and encompasses processes with a horizontal scale smaller than a few kilometers and a timescale shorter than an hour. It thus contains fully three-dimensional turbulent motion in the planetary boundary layer, tornadoes and small-scale cumulus clouds. Major instabilities in the atmosphere, such as thermal- (e.g. convective instability that converts potential to kinetic energy) and shear instabilities (e.g. Kelvin-Helmholtz-instability) act on the microscales (Lin, 2007, p. 7). Furthermore, viscous dissipation acts within the microscale to reduce the atmospheres total energy.

On the large-scale end of the spectrum, processes with spatial scales larger than a few thousands kilometers and timescales larger than a day are assigned to the macro- or more commonly referred to as the synoptic scale. Examples of such motions are planetary waves and large mid-latitudinal low- and high pressure systems. Mid-latitudinal synoptic-scale motion is mainly driven by baroclinic instability, i.e. the instability arising in the mean wind caused by the North-South temperature gradient in the atmosphere due to differential warming by the sun.

The third scale range in Fig. 1.2, the mesoscales, was first mentioned in a study evaluating the use of radar measurements (Ligda, 1951) and was defined as the scale range between the microscales ("*scale too gross to be observed from a single station*") and the synoptic scales ("*yet too small to appear on sectional synoptic charts*"). The mesoscales thus contain processes on spatial scales between a few to a few thousand kilometers that are associated with temporal

scales of several minutes to one day. Such processes are for example lee waves, clear-air turbulence, slope winds (meso-γ), squall lines, severe storms, mountain wave disturbances, diurnal variations such as land-sea winds and cloud clusters (meso-β). In addition it includes surface and upper level fronts, hurricanes and jet stream features (meso-α)(Lin, 2007, p. 2). Importantly, while mesoscale flow can be driven by a variety of instabilities (e.g. static-, centrifugal-, inertial-, symmetric and shear instability; Markowski and Richardson, 2010, p. 41 ff.), there is no dominant instability corresponding to the convective- and baroclinic instabilities on the micro- and synoptic scales respectively.
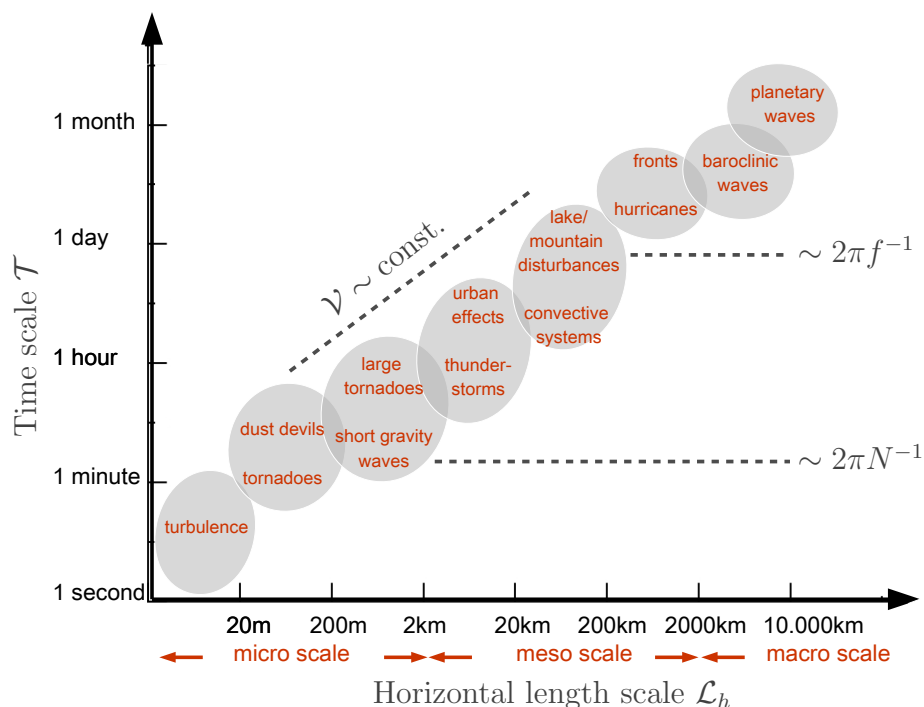
Figure 1.2: Classification of atmospheric processes according to their associated horizontal spatial- and temporal scales. Dashed lines indicate a constant characteristic velocity scale and characteristic limits imposed by the Coriolis parameter f and the Brunt-Väisälä frequency N: mid-latitudinal mesoscales motion ranges from the period of a pure buoyancy oscillation $2\pi/N$ (gravity wave motion; $\sim 10\,\text{mins}$) to a pendulum day (inertial oscillations; $\sim 17\,\text{h}$) (following Markowski and Richardson, 2010, p. 4).

The mesoscales particularly contain weather phenomena that can have a significant impact on human life, i.e. that are accompanied by strong mean winds, wind gusts and heavy precipitation (referred to as high-impact weather; Craig et al., 2010). These processes are especially in summer often associated with deep moist convection. Thus, a profound understanding of dynamical processes acting on the mesoscale range is of great concern for various applications (particularly related to skillful numerical weather forecasts) and are the topic of this thesis.

The introduced various atmospheric processes are mathematically described by the so called primitive equations. This set of nonlinear partial differential equations bases on basic conservation principles of momentum, thermodynamic energy and mass. The horizontal wind described by the momentum equation is generally composed of a rotational and divergent component, which are associated with vertical vorticity and horizontal divergence respectively. In the scale-analysis technique, magnitudes of terms contained in the governing equations are estimated and compared for various types of motion acting on different scale ranges. Certain terms are then found to be of major or minor importance to the considered scale range, whereby neglecting the latter might be a valid simplification to the set of equations describing the respective dynamics. In there, balances, i.e. diagnostic relationships between certain terms, arise (e.g. Holton, 2004, p. 40). Micro-, meso- and synoptic-scale phenomena are—besides their classification according to their spatial and temporal scales—found to be characterized by distinct leading order dominant dynamics (e.g. Markowski and Richardson, 2010, p. 5 ff.). Examples for such simplifications on the different scales will be given in the following.

Microscale flow is three-dimensional in nature which implies that horizontal and vertical scales are comparable in magnitude. In particular, dynamical pressure gradients in the horizontal and vertical direction play a principle role. Motion on these scales is generally unbalanced (i.e. no dominant balance relation holds) and vertical velocities and horizontal divergence are a significant part of the underlying dynamics. On these scales the disregard of the Coriolis force arising from the earth's rotation is a valid approximation to the underlying equations.

On the other hand, synoptic-scale dynamics feature horizontal scales much larger than vertical scales and are thus to a good approximation two-dimensional (Charney, 1948). On these scales, two major balance relations hold: first, the pressure can be considered hydrostatic, i.e. the vertical pressure gradient and the gravitational acceleration balance. Second, the horizontal wind field is to a good approximation in geostrophic balance, i.e. horizontal pressure gradient balances Coriolis acceleration. This geostrophic wind characteristic for synoptic-scale flow is purely rotational and divergence-free. The mathematical equations that describe synoptic-scale flow can thus be approximated by neglecting vertical accelerations and advection by non-geostrophic wind to leading order.

Mesoscale flow encompasses dynamical systems that contain a variety of spatial and temporal scales. A typical example are long-lived mesoscale convective systems, which feature large pressure gradients and horizontal and vertical accelerations of air. They are furthermore influenced by micro-physical processes through latent heating and cooling and in addition the Coriolis force and radiative transfer might play a role. Thus, the underlying equations retain their full complexity and simplifications generally do not apply to the full mesoscale range (Markowski and Richardson, 2010, p. 10). In particular, the nature of dominant motion transitions through the mesoscales, from small- to large scales, from predominantly unbalanced and divergent to predominantly balanced and rotational. Rotational and divergent mesoscale modes *"intermingle in a non-linear jigsaw puzzle"* (Bühler et al., 2014), rendering a general identification of either process as dominant unfeasible.

1.1.1 Scale interaction processes

The complexity of atmospheric flow not only arises from the variety of dynamical processes included in the scales of atmospheric motion. These modes of atmospheric flow furthermore interact and exchange energy. This scale-interaction mathematically arises from the fundamental non-linearity of the advection-term contained in the underlying primitive equations.

The concept of atmospheric scale interactions can be illustrated by considering a simple flow system where a weak disturbance is imposed on a slowly varying mean flow (Emanuel, 1986). Initially, the dominant scale interaction process is the impact of the mean flow on the small perturbation (e.g. through advection). As the disturbance grows, however, it exerts an increasing influence on the mean flow and other scales of motion develop through secondary instabilities. While this process continues, increasingly more scales of the flow are excited, which enhances the degree of disorder in the flow and ultimately leads to a highly non-linear flow system. Fully developed turbulence is such a flow regime, where the chaotic interaction between numerous scales is usually treated statistically (Pope, 2000, p. 34 ff.). The question, to which extent mesoscale motion is disordered, i.e. whether it is chaotic enough to be treated statistically (i.e. homogeneous turbulence theory; Kolmogorov, 1941), or if dynamics can and have to be treated explicitly (e.g. wave-mean flow interactions; Grimshaw, 1975), is a subject of current research (e.g. Achatz et al., 2017).

Mesoscale circulations can be forced locally through instabilities and interactions with the lower boundary such as thermal- and orographic surface inhomogeneities. They are, however, also significantly energized by scale-interaction processes with micro- and synoptic-scale flows. Such mechanisms are for example interactions of cloud and precipitation processes with mesoscale systems and internal adjustment of larger-scale flow systems such as fronts, cyclones and jet streaks, respectively. One scale interaction mechanism whereby energy is transferred from small (micro-) scales to large (synoptic-) scales through the mesoscales is the geostrophic adjustment following convective heating. This mechanism proves particularly relevant to this dissertation.

The geostrophic adjustment process

Latent heat release within a single convective cloud introduces an imbalance into the atmosphere on a typical horizontal length scale $\mathcal{O}(1\,\mathrm{km})$ (Raymond, 1986). The response in the surrounding free atmosphere is twofold: on the one hand, transient inertia-gravity waves (IGWs), i.e. internal wave modes modified by the effect of rotation with frequencies between the Brunt-Väisälä-frequency N and the inertial frequency f are excited (Fritts and Alexander, 2003). These waves quickly propagate out of the cloud region, a process whereby energy is radiated away (see Fig. 1.3a and Nicholls et al., 1991). On the other hand, a synoptic-scale balanced response is spun up by means of the geostrophic adjustment process (Rossby, 1937, 1938) on longer timescales (for a review see Blumen, 1972).

Here, the physical mechanism depicted schematically in Fig. 1.3b is understood as follows: the latent heat release within a convective cloud generates a positive buoyancy anomaly that strengthens an updraft (blue arrow in the center of the cloud). The upward motion causes a positive pressure anomaly above the heating, which in turn drives a divergent outflow in

the upper half of the troposphere (i.e. below the upper boundary imposed by the tropopause). For continuity, the upper-level horizontally divergent motion (light blue arrows) is associated with compensating subsidence (white arrows) and lower level convergence (gray arrows). The Coriolis force that acts on the divergent outward motion increases the azimuthal wind. Ultimately, the horizontal wind field reaches a balance between the horizontal pressure gradient $\nabla_h p$ and the Coriolis force $f \boldsymbol{v}_h$. This state is referred to as *geostrophic balance* and the associated spun-up balanced rotational wind is centered around the location of the cloud. This geostrophically balanced anticyclonic (i.e. clockwise rotating) vortex features a much larger horizontal scale than the length scale of the forcing (i.e. cloud-scale), namely the first baroclinic Rossby radius of deformation $R_d = N\mathcal{L}_v/f$ (with $\mathcal{L}_v$ characteristic vertical length scale of the forcing, here the tropopause height) with a typical mid-latitudinal value $\mathcal{O}(1000\,\text{km})$ (Gill, 1982, p. 207). At lower levels, as indicated in gray in Fig. 1.3b, a balanced vortex of the same scale and opposite sign (i.e. cyclonic rotation) is spun up where the Coriolis force and pressure gradient balance the convergent motion. Note that in the real atmosphere, the lower-level convergence and -cyclone can be weakened by interactions with the lower boundary (e.g. surface friction), as opposed to the divergence and anticyclone in upper levels where the flow evolves more freely.
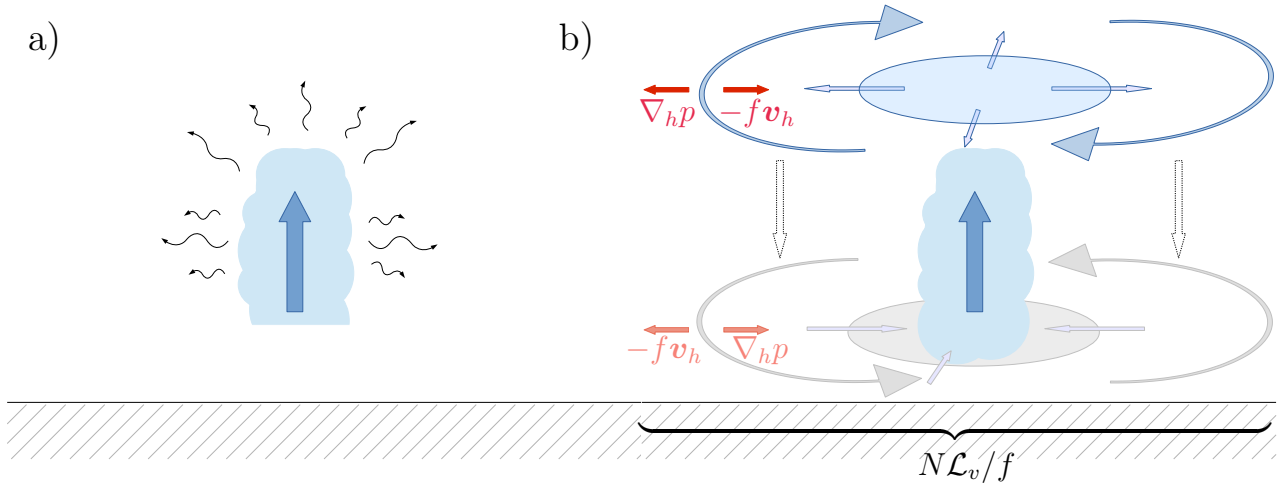
Figure 1.3: Schematic illustration of the impact of a convective cloud on the free atmosphere. a) Radiation of transient gravity waves. b) Spin-up of balanced flow through geostrophic adjustment process. $f\boldsymbol{v}_h$ is the Coriolis force with the Coriolis parameter f and the horizontal wind field $\boldsymbol{v}_h = u\boldsymbol{e}_x + v\boldsymbol{e}_y$ with components (u, v) and unit vectors of the two-dimensional cartesian coordinate system $(\mathbf{e}_x, \mathbf{e}_y)$. $\nabla_h p$ is the pressure gradient force with p pressure and ∇_h denotes the horizontal gradient operator $\nabla_h = \partial_x \boldsymbol{e}_x + \partial_y \boldsymbol{e}_y$ with partial derivatives in the x- and y-direction, ∂_x and ∂_y, respectively.

In this section the complex dynamical and thermodynamical processes of the earth's atmosphere that feature various spatial and temporal scales were introduced. Large-scale atmospheric dynamics are influenced by the Coriolis force and predominantly balanced and rotational. Small-scale dynamics are not driven by the Coriolis force and mainly unbalanced and divergent. On the mesoscale range, which is of particular concern in the current thesis, neither mode of motion can be regarded as generally predominant. Whether or not scale

interaction processes on the mesoscales between rotational and divergent modes of motion are sufficiently disordered and chaotic that a statistical treatment is justified, or if they should be treated dynamically explicit remains currently ambiguous. An example of the latter is the geostrophic adjustment process following an imbalance imposed on the atmosphere by latent heating within a convective cloud. Energy is thereby transferred from a kilometer-(micro)-scale disturbance to the large synoptic scales in a non-turbulent manner. While being transitioned from small- to large scales through the mesoscales, the nature of dominant motion changes from predominantly unbalanced and divergent to predominantly balanced and rotational.

1.2 The atmospheric kinetic energy spectrum

One particularly intriguing property of fully turbulent, statistically homogeneous and isotropic flows is the power-law shape of the energy spectrum (Kolmogorov, 1941; Obukhov, 1949). While atmospheric flow on scales larger than the microscales is not characterized by fully developed homogeneous turbulence, various atmospheric processes are known to feature a spectral power-law behavior. One example is the size distribution of shallow cumulus clouds (Neggers et al., 2002; Zaho and Girolamo, 2007). Another particularly relevant example to the present study is the one-dimensional horizontal atmospheric kinetic energy spectrum, i.e. the distribution of variance of the wind velocity components over spatial scales (e.g. Fiedler and Panofsky, 1970). It is formally defined as (e.g. Blažica et al., 2013)

$$E_K(k) = \frac{1}{2}(\hat{u}\hat{u}^* + \hat{v}\hat{v}^*)\,, \tag{1.1}$$

where $\hat{u}$ and $\hat{v}$ are the Fourier-transformed components of the horizontal wind field. Their complex-conjugated counterparts are denoted by the asterisk. The Fourier-transform decomposes a field in real space into harmonic waves characterized by wavenumber k. The associated wavelength $\lambda = 2\pi/k$ can be understood as the horizontal spatial scale $\mathcal{L}_h$ introduced in section 1.1. In the remainder of this chapter, the term *kinetic energy spectrum* will refer to the one-dimensional horizontal kinetic energy spectrum if not explicitly stated otherwise.

1.2.1 Measurement data

In a series of highly recognized papers, Nastrom and Gage (1983), Nastrom et al. (1984) and Nastrom and Gage (1985) published the first examination of the atmospheric kinetic energy spectrum covering the whole mesoscale range based on wind measurements taken in the course of the *Global Atmospheric Sampling Program* (GASP). The evaluated comprehensive GASP data set contains almost 7000 flights from commercial airplanes over a four year period (1975 - 1979) and allowed for an extensive evaluation of statistics of atmospheric kinetic energy as well as the variability of the kinetic energy spectrum.

In Fig. 1.4 the spectrum of horizontal kinetic energy (averaged over all flight segments) is displayed as a function of horizontal wavenumber k (lower x-axis) and wavelength λ (upper x-axis). The spectrum shows a power-law behavior on two scale ranges: on the synoptic scales ($1000\,\text{km} < \lambda < 3000\,\text{km}$) the spectrum follows an approximate k^{-3}-dependence. On the mesoscale range (here $2.6\,\text{km} < \lambda < 300\,\text{km}$), the slope of the observed spectrum flattens notably and features an approximate $k^{-5/3}$-dependence. Since spectral power-law behaviors are characteristic for self-similar systems (e.g. Pope, 2000, p. 99), the discovery of the k^{-3} and $k^{-5/3}$ spectral ranges as universal statistical features of tropospheric dynamics constituted a milestone in the progress of research on mesoscale dynamics and associated scale interaction processes.
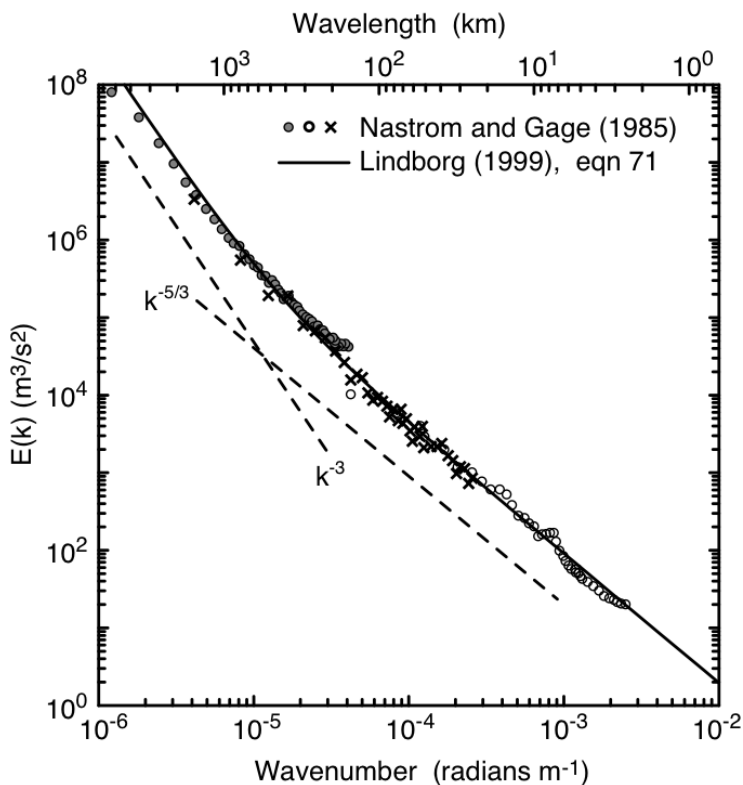
Figure 1.4: Horizontal atmospheric kinetic energy spectrum (in m^3/s^2) derived from GASP aircraft measurements (symbols; Nastrom and Gage, 1985) and functional fit to *Measurements of Ozone and Water Vapor by Airbus In-Service Aircraft* (MOZAIC) aircraft measurements by (solid lines; Lindborg, 1999). Figure taken from Skamarock (2004).

The large spatial and temporal extent of the data analyzed by Nastrom and Gage (1985) allowed for an examination of the variability of the obtained results with season, height and location. They found a general increase of measured spectral amplitude with latitude and height, higher values for winter than for summer and a significant (up to 4 times) higher mesoscale energy over the ocean than over land. The established paradigm of the universality of the atmospheric kinetic energy spectrum (Lindborg, 1999; Tung and Orlando, 2003; Ska-

marock, 2004), however, outclassed the associated significant variability found in the GASP data. The universality of the observed spectral slopes is subject of ongoing research (Waite and Snyder, 2013; Fang and Kuo, 2015; Bierdel et al., 2016; Sun et al., 2017).

1.2.2 Prevailing explanations

As indicated above, the power-law behavior of the atmospheric kinetic energy spectrum suggests that the underlying dynamics are self-similar. Isotropic, two- and three-dimensional turbulent flows are found to be self-similar on the so-called inertial subrange (see schematic in Fig. 1.5). This is the scale range of a turbulent flow with a stationary spectrum that is located between the injection- and dissipation scales (Frisch, 2004, p. 86). There, conserved quantities of the underlying equations such as energy are neither injected nor diminished. They are solely transferred through non-linear interactions between eddies, i.e. isotropic turbulent motion associated with a length scale $\mathcal{L}_h$, a timescale $\mathcal{T}$ and velocity scale $\mathcal{V}$ (Richardson, 1922). In there, eddies of similar magnitude interact, rendering the scale-interaction local in wavenumber space. The concept of the inertial subrange plays a crucial role in theoretical studies of the atmospheric kinetic energy spectrum, since it allows for a statistical treatment of the underlying flow (see paragraph 1.1.1) and particularly the derivation of spectral slopes from simple dimensional arguments (Kolmogorov, 1941; Obukhov, 1949; Garrett and Munk, 1972). The kinetic energy spectrum of three-dimensional turbulence is thereby found as (Frisch, 2004, p. 92)

$$E(k) \sim \epsilon^{2/3} k^{-5/3} \, , \tag{1.2}$$

where ϵ is the energy injection-, dissipation- and transfer rate and k is the wavenumber.
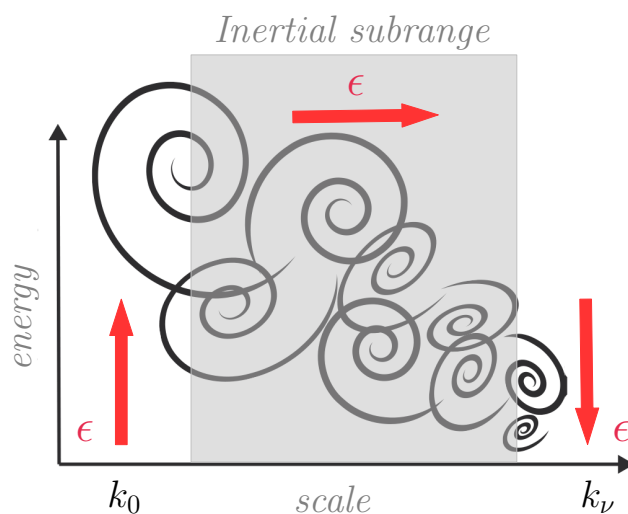
Figure 1.5: Schematic illustration of the inertial subrange and energy cascade established in a stationary energy spectrum according to Kolmogorov (1941) and Richardson (1922). The energy is injected at rate ϵ on large scales (k_0) and dissipated through molecular dissipation at the same rate on small scales (k_ν). On intermediate scales (the inertial subrange) energy is transferred at rate ϵ from the large injection- to the small dissipation scale through non-linear interactions (i.e. breakup of larger eddies into smaller ones).

Additionally, a flow only consisting of waves is thought to feature a similar inertial region between a spectrally-separated source and sink in a saturated (i.e. source and sink in equilibrium) spectrum. Owing to the fundamentally distinct underlying dynamics (waves as opposed to eddies), however, the energy sources, sinks and transfer mechanism are radically different.

Synoptic-scale k^{-3} -slope

Synoptic-scale flow is quasi-two-dimensional in nature and is dominated by rotational modes of motion (see paragraph 1.1). Two-dimensional flows conserve the enstrophy (i.e. the square of the vorticity) in addition to the total kinetic energy. The k^{-3} spectral slope on the large synoptic scales has been found to be in good agreement with dimensional considerations in the framework of barotropic quasi-two-dimensional (Kraichnan, 1967) or quasi-geostrophic (Charney, 1971) turbulence theory. In there, a direct or downscale (i.e. from large to small scales) enstrophy cascade underlies the horizontal kinetic energy spectrum. Physically, the cascade arises from the collapse of horizontal vortical structures that are energized on the large scales by baroclinic instability (Boer and Shepherd, 1983). This theory regarding the observed k^{-3} spectral slope is well-established (Waite and Snyder, 2013; Fang and Kuo, 2015; Sun et al., 2017).

Mesoscale $k^{-5/3}$ -slope

Owing to the wide spectral range covered by the mesoscales it contains processes with distinct dominant underlying dynamics. Attributing the observed spectral slope to a single dynamical mechanism thus appears much more complicated than on the synoptic scales (for a review see Gkioulekas, 2006). Dimensional arguments for the energy-cascading inertial subrange in three-dimensional isotropic turbulence result in a $k^{-5/3}$ spectral slope (Kolmogorov, 1941; Obukhov, 1949). While three-dimensional turbulence theory is, as observations and modeling studies show, appropriate for cloud-scale and below, mesoscale flow is highly stratified and clearly not characterized by a three-dimensional, isotropic turbulent inertial subrange (Skamarock, 2004). Over the last three decades various theories about the dynamical origin of the $k^{-5/3}$ mesoscale slope have been suggested. They can be divided according to the relative importance of rotational and divergent energy as well as the degree of their interaction into three categories, namely

1. eddies interacting non-linearly in a turbulent manner, i.e. purely rotational

2. IGWs interacting linearly through shear, i.e. purely divergent

3. eddies and IGWs interact non-linearly, i.e. both rotational and divergent

Besides the mentioned k^{-3} enstrophy subrange, two-dimensional turbulence features two energy subranges that exhibit a $k^{-5/3}$ power-law behavior. They are located on the smaller- and larger-scale side of the source region and are associated with a direct and inverse energy cascade respectively (Merilees and Warn, 1972; Tung and Welch, 2001; Gkioulekas and Tung, 2007). The physical mechanism that sets up a direct and inverse cascade is the collapse and merging respectively of two-dimensional vortices. Based on the understanding that two-dimensional

flow is the lowest order balanced approximation for mesoscale motion (i.e. geostrophic and hydrostatic balance hold, see section 1.1), theories of the first category interpret the mesoscales as an inertial subrange of quasi-two-dimensional turbulence. In there, energy is injected either on small-scales (e.g. through convective instability and associated thunderstorm anvil outflows) and cascaded inversely (Gage, 1979; Lilly, 1983). Energy might also be injected on large scales (i.e. through baroclinic instability) and cascaded directly (Tung and Orlando, 2003; Tulloch and Smith, 2006).

Theories of the second category attribute the mesoscale energy spectrum to primarily divergent, quasi-linear IGWs (Dewan, 1979; VanZandt, 1982). This directly opposes the first category, where rotational modes establish an energy cascade. Gravity waves are forced by various atmospheric processes (e.g. deep moist convection, orography and baroclinic flows; Fritts and Alexander, 2003) and can be dissipated on small scales by shear instabilities such as Kelvin-Helmholtz instability (Dewan, 1994, 1997). Based on studies analyzing oceanic wave spectra (Garrett and Munk, 1972, 1975), theories of the second category regard the mesoscales as an inertial subrange, and dimensional considerations predict a $k^{-5/3}$ spectral power-law dependence. A self-similar direct cascade is set up through the generation of shear by larger-scale waves and smaller-scale waves that extract energy from this shear. Note that the IGW-theory does not postulate the absence of balanced vortical structures, it merely states that rotational modes of motion and divergent IGWs interact weakly (Callies et al., 2014, 2016).

The third category addressing the mesoscale $k^{-5/3}$-regime is stratified turbulence (Lilly, 1983; Lindborg, 2006), i.e. turbulent flows that are subject to a stabilizing density gradient. In these flows, quasi-horizontal meandering motions (see category 1, carrying all the flow's vertical vorticity) and internal waves (see category 2, carrying all the flow's horizontal divergence) interact in a non-linear manner (Riley and Lelong, 2000; Riley and Lindborg, 2008). An energy-cascading inertial subrange with a $k^{-5/3}$ slope is established by flow instabilities arising from vertical shearing of horizontal winds (e.g. onset of decorrelation instability and zigzag instability; Lilly, 1983; Billant and Chomaz, 2000) by means of two processes: through the break up of larger rotational structures in the horizontal in a two-dimensional turbulence sense (see category 1) as well as through the development of local patches of three-dimensional turbulence in local regions of strong shear (Riley and Lindborg, 2008).

All theories for the dynamical origin underlying the mesoscale kinetic spectrum mentioned above have the major assumption in common that the mesoscales can be treated statistically as an inertial subrange (either in a turbulence- or wave sense). However, real atmospheric mesoscale flow can be directly energized by highly intermittent processes such as fronts and organized moist convection. The concept of a turbulent inertial subrange thus renders the mathematical description of the mesoscale kinetic energy spectrum tractable, but its applicability to real atmospheric mesoscale flow is a topic of current research (Zhang et al., 2007; Waite and Snyder, 2013; Sun and Zhang, 2016; Weyn and Durran, 2017). All established theories furthermore focus on the prediction of the $k^{-5/3}$ power-law dependence of the mesoscale kinetic energy spectrum, whereby little is known about the governing dynamical processes. However, gaining a deeper understanding of the dynamics and scale interaction processes is of fundamental importance to advance research in this field. To that end the separation of

mesoscale wind velocities, as for example measured in the comprehensive GASP or MOZAIC aircraft campaigns (see paragraph 1.2.1) into rotational and divergent flow components is a key factor.

1.2.3   Relevance of rotational and divergent modes

Wind fields that are characteristic for real atmospheric mesoscale flow are usually associated with rotational and divergent modes of motion, where the relative importance as well as the nature of their interaction are crucial to understanding the dynamics underlying the $k^{-5/3}$-inertial range. The horizontal wind field and kinetic energy spectrum can be decomposed into rotational and divergent components by means of the two-dimensional Helmholtz-decomposition (e.g. Bühler et al., 2014, for details see chapter 2).

Rotational and divergent modes of motion have been derived from numerical model simulations where the u- and v-wind fields are known and the application of the Helmholtz-decomposition is straightforward. An approximate $k^{-5/3}$ mesoscale spectral slope is found to be a feature of many global circulation models (Koshyk and Hamilton, 2001; Hamilton et al., 2008; Brune and Becker, 2013; Burgess et al., 2013; Skamarock et al., 2014), local numerical weather prediction models (Skamarock, 2004; Bierdel et al., 2012; Blažica et al., 2013; Ricard et al., 2013) and more idealized numerical simulations of atmospheric flow (Waite and Snyder, 2013; Sun et al., 2017; Weyn and Durran, 2017). The Helmholtz-decomposition, however, leads to ambiguous results: the mesoscale kinetic energy spectrum is found to be governed by predominantly rotational (Hamilton et al., 2008) or predominantly divergent (Weyn and Durran, 2017) dynamics, or by an approximate equipartition of both components (Skamarock et al., 2014). However, while simulated spectra and energy budgets can be sensitive to the model configuration (e.g. horizontal and vertical resolution and strength of dissipation) a decomposition of measurement data into rotational and divergent modes is desirable (Koshyk and Hamilton, 2001; Skamarock, 2004; Frehlich and Sharman, 2008; Augier and Lindborg, 2013; Brune and Becker, 2013).

Large data sets taken by commercial aircraft (e.g. GASP and MOZAIC, see section 1.2.1) contain line-measurements of the longitudinal (along-track) and transverse (across-track) wind components (Callies et al., 2014; Lindborg, 2015). Since for the standard Helmholtz-decomposition the two-dimensional u- and v-components of the wind field have to be known, the separation of measurement data into rotational and divergent modes long remained unfeasible. Recently, Bühler et al. (2014) proposed a method that allows the extraction of rotational and divergent kinetic energy spectra from one-dimensional measurement data of the horizontal velocity components that was further extended by Lindborg (2015). While this one-dimensional Helmholtz-decomposition method has been applied to measurement data, it is based on strong assumptions (e.g. homogeneity and isotropy of the underlying flow field) that do not necessarily hold for atmospheric flow.

In this section the measured horizontal atmospheric kinetic energy spectrum has been introduced. It features two distinct power-law ranges that are separated by a transition on a scale of a few hundred kilometers: a k^{-3}-spectral range on the large scales and a mesoscale $k^{-5/3}$-regime. Despite the significant variability found particularly in the mesoscale part of

the spectrum, the discovery of the $k^{-5/3}$ power-law spectrum initiated research that aimed at determining a *universal* dynamical mechanism governing mesoscale flow. There is a wide consensus about the k^{-3} spectral regime being associated with quasi-two-dimensional turbulence. The origin of the mesoscale $k^{-5/3}$ slope, however, is less clear. All so far established theories treat the mesoscales as a spectral inertial subrange and are thus statistical in nature. The theories do, however, make fundamentally different assumptions regarding whether the dominant scale-interaction mechanism is primarily between rotational or divergent modes of motion. The extraction of rotational and divergent contributions to the horizontal wind field and the associated kinetic energy spectrum from measurement data is thus a fundamental test of these prevailing theories. While such a one-dimensional Helmholtz-decomposition method has recently been proposed, it bases on strong mathematical assumptions on the underlying flow field that need to be validated.

Scale-interaction mechanisms in atmospheric flow, however, not only shape the observed horizontal kinetic energy spectrum. They also determine how errors are exchanged between different modes of atmospheric motion. Particularly the growth of initially small errors in the numerical weather prediction process potentially renders a weather forecasts erroneous. The general problem of *predictability* of atmospheric flow is the topic of the next section.

1.3   Predictability

The skillful prediction of weather, i.e. dynamical and thermodynamical processes of the mid-latitudinal mesoscales, is one major aim of meteorological research. In the numerical weather prediction (NWP) process, an approximated initial state of the atmosphere is determined from observations and is integrated in time with a discretized form of the hydrodynamical partial differential equations describing atmospheric flow (Bjerknes, 1904). The predictability time is thereby defined as the time interval within which the variance of two solutions that begin with slightly different initial conditions reaches some prechosen magnitude (bounded by the error variance of two random atmospheric states) (Lorenz, 1969). In the NWP process two aspects are found to limit the predictability of atmospheric flow: first, the employed NWP system is imperfect. Examples of inaccuracies in the NWP model are the numerical representation (i.e. discretization) of the governing equations and subgrid-scale processes as well as the quality and coverage of employed observations (Sun and Zhang, 2016). The finite horizon of a skillful weather forecast that arises from an imperfect forecasting system is referred to as *practical* predictability limit (Melhauser and Zhang, 2012). The continuous increase of computing power led together with an improvement of numerical aspects of the forecasting system to an extension of the forecast horizon by one day per decade over the last thirty years (Bauer et al., 2015). Second, there is a limit of predictability even if the NWP model and the initial conditions were nearly perfect (Lorenz, 1969). This *intrinsic* predictability limit originates from the basic chaotic nature of atmospheric flow (Poincaré, 1914, p. 68). As will be explained shortly, the intrinsic predictability limit is a non-alterable characteristic of the dynamics of the underlying flow which can in particular not be extended by improving the employed NWP system.

In this dissertation the intrinsic predictability limit will be assessed. Before the predictability of real atmospheric flows will be discussed, a simple example of limited predictability that is relevant to the NWP process will be given.

1.3.1 Deterministic chaos in low-dimensional systems

A salient step in research on predictability of dynamical systems was taken by Lorenz (1963, in the following L63). In L63, the temporal evolution of a small perturbation introduced into a low-dimensional (i.e. three degrees of freedom) flow system is examined. Here and in the following, the term "error" will be used to describe the difference between an unperturbed- and a perturbed flow. The studied system itself is deterministic, i.e. the initial conditions and underlying mathematical equations are known and do not contain any stochastic element. The error is found to grow exponentially, such that the evolution of the unperturbed and of the perturbed flow rapidly diverge until they are indistinguishable from random states of the system after a finite period of time. This chaotic behavior of the flow that originates from the sensitive dependence of the flow evolution on the initial conditions is referred to as deterministic chaos (Frisch, 2004, p. 27 ff.). It arises even if the underlying mathematical equations (i.e. laws of physics) are perfectly known. The limit of predictability in the L63-system depends on the magnitude of the initial condition error such that a reduction of the initial error amplitude leads to an extended predictability time (Palmer et al., 2014).

An application of the simple L63-model to the earth's atmosphere suggests that a slight error in the initial-conditions leads to significantly different, and possibly useless, weather forecasts (i.e. one major reason for the failure of the first weather forecast by Richardson, 1922). Owing to the vast amount of observations required to determine the atmosphere's state (e.g. alone 10^{43} in the earth's troposphere if 10 variables are determined up to the mean free path of molecules $\mathcal{O}(1\,\mathrm{nm})$), the *exact* initial condition of a system like the earth's atmosphere will never be known. Small inaccuracies in the initial state will always grow and lead to erroneous forecasts.

1.3.2 Predictability of atmospheric flow

The fundamental insights gained through the L63-model constitute a major step in understanding atmospheric predictability and error growth. The earth's atmosphere is, however, as indicated above not a low-dimensional dynamical system, but rather chaotic and multiscale in nature. In there, the interaction of various modes of motion adds additional complexity to the predictability problem. Predictability limits in atmospheric flow arise from an error propagation between different scales of motion that emerges from the non-linear nature of the underlying equations (see paragraph 1.1.1).

Thus, for understanding the predictability of atmospheric flow the nature of the dominant underlying scale interactions needs to be assessed first. On the mesoscales, this major dynamical agent remains undetermined and so does the quantitative limit of mesoscale predictability. Estimates of the latter range from couple tens of hours to several days (Anthes et al., 1985; Zhang et al., 2007). Certain components of atmospheric flow are tied to either constant or periodic external forcings, such as solar radiation ("summer is always warmer than winter")

that enable seasonal and climate predictions. These processes feature a relatively high predictive skill that is potentially inherited to mesoscale flow and extends the horizon of a skillful forecast (Anthes, 1986). Other processes, however, such as the upscale growth of inevitable initial condition errors shorten the horizon of a skillful mesoscale forecast (Anthes et al., 1985; Zhang et al., 2007). This thesis focuses on processes of the latter category that intrinsically limit the horizon of a skillful weather forecast. In the following, two fundamentally different theories for the nature of the scale interactions that lead to upscale growth of small initial condition errors will be introduced.

The homogeneous turbulence approach

The predictability horizon arising from the upscale growth of errors in a fully turbulent flow can be assessed with simple dimensional arguments (Lilly, 1972; Vallis, 2006, p. 363 ff.). In there, the error is thought to be transferred between eddies of similar temporal and spatial scales (see cascade process that governs the turbulent kinetic energy spectrum in Fig. 1.5). Note that properties of the basic or background flow's kinetic energy spectrum and the error spectrum are not identical. Particularly a forward cascade underlying the background kinetic energy spectrum can well coexist with an inverse cascade of errors. An initially small error of a certain scale is transferred to the next larger scale in the local eddy turnover time defined as

$$\mathcal{T}(k) \sim (\mathcal{V}(k)k)^{-1}\,, \tag{1.3}$$

where $\mathcal{T}(k)$ and $\mathcal{V}(k)$ are the characteristic time- and velocity scales of the eddy characterized by wavenumber k. The velocity scale is given by the background kinetic energy spectrum E_K through the relationship

$$\mathcal{V}(k) \sim (E_K(k)k)^{1/2}\,. \tag{1.4}$$

According to the standard local cascade hypothesis, the predictability time T_p (i.e. the time it takes for the errors to propagate from the small scale k_0 to the larger scale k_1) is given by the integral of the eddy turnover time $\mathcal{T}(k)$ over the given scale range, reading

$$T_p \sim \int_{k_0}^{k_1} \frac{\mathcal{T}(k)}{k} dk\,. \tag{1.5}$$

Omitting $\mathcal{O}(1)$ constants and the dependency on the energy flux ϵ (see (1.2)), it follows for a three-dimensional turbulent flow with a $k^{-5/3}$ background E_K spectrum

$$T_{3D} \sim k_1^{-2/3} - k_0^{-2/3}\,. \tag{1.6}$$

An important implication of (1.6) is the *intrinsic predictability* limit for the considered flow, i.e. an initial confinement of the error to ever smaller scales (i.e. $k_0 \rightarrow \infty$) does not imply $T_{3D} \rightarrow \infty$. The predictability time remains instead finite. This result highlights a fundamental difference between fully turbulent flows (predictability time intrinsically limited) and the deterministic chaos case (ever-increasing predictability time for decreased initial errors). For flows such as two-dimensional barotropic turbulence, which feature a background spectrum equal or steeper than k^{-3} (as observed for the synoptic-scale flow, see paragraph 1.2.1),

however, an analogous dimensional argument as outlined in (1.3)-(1.6) leads to a significantly different result. In this case, the predictability time can be extended arbitrarily by making the initial error sufficiently small. Thus, the slope of the background kinetic energy spectrum in which the errors grow plays a fundamental role for the nature of a flow's predictability limit.

As an extension to the dimensional considerations introduced above, Lorenz (1969, in the following L69) examined predictability limits and growth of errors of different initial scale in a simple model based on the barotropic vorticity equation. In barotropic, two-dimensional statistically homogeneous and isotropic turbulence, energy is exchanged between different scales of motion through nonlinear interactions of vortical horizontal structures (Kraichnan, 1967). L69 derives a fundamental equation for error growth as a function of time and spatial scale. In L69, a full matrix containing the scale-interaction coefficients between all scales of motion quantitatively is considered (as opposed to the *upscale* growth of errors through *local* scale-interactions in the dimensional example above). The slope of the background spectrum is—as in the dimensional argument—found to play a crucial role for the error growth characteristics. The dynamics underlying the spectral slope, however, play a minor role (Rotunno and Snyder, 2008).

In Fig. 1.6, two example scenarios of intrinsic predictability examined by L69 are displayed. The mean background kinetic energy spectrum, i.e. averaged over an ensemble of realizations that evolve freely from different initial conditions, is assumed to feature a $k^{-5/3}$ slope (solid gray line). The evolution of the error introduced into the model initially either on small (experiment A) or on large scales (experiment B) is displayed for a time up to three days (dashed lines). All predictability of a process associated with a length scale or wavelength λ is lost when the error kinetic energy spectrum saturates, i.e. reaches the magnitude of the background kinetic energy spectrum.
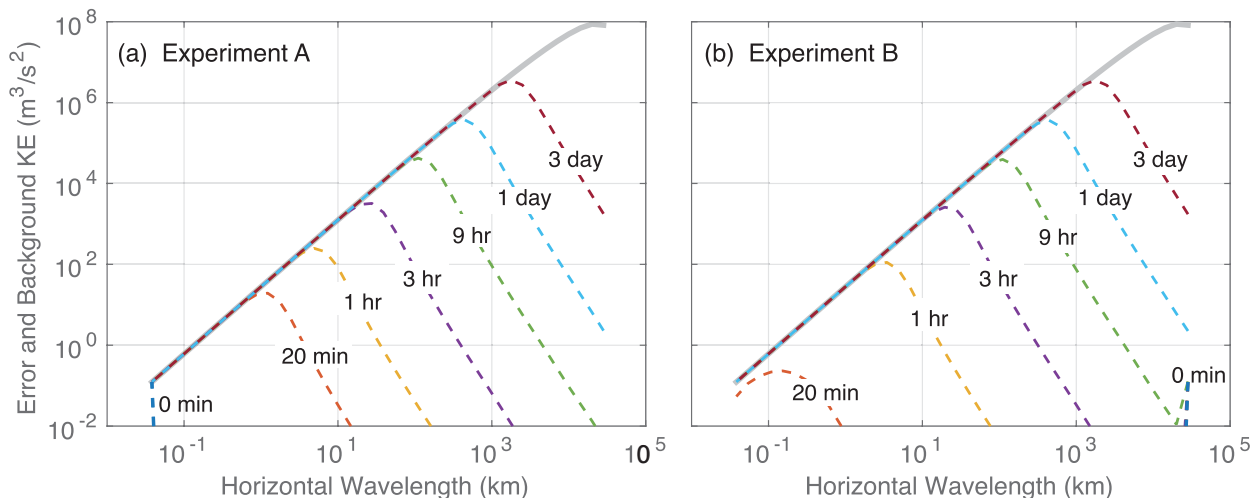

Figure 1.6: L69-experiments A (left) and B (right): error-kinetic energy as a function of the horizontal scale for times ranging from 0 minutes to 3 days (dashed colored lines). Thick gray line: mean background kinetic energy spectrum with the $k^{-5/3}$ slope assumed by L69. The scale increases on x-axis from left to right. Figure taken from Durran and Weyn (2016).

When the error is initially confined to the smallest scale (here 38 m, left panel of Fig. 1.6) and saturated, it directly interacts with larger scales of the flow such that after 20 minutes all predictability on scales smaller than 1 km is lost (red dashed line). The non-linear turbulent cascade of error kinetic energy proceeds upscale, where after three days all predictability of scales smaller 2000 km is lost.

If an error of the same amplitude as in the previous experiment is, however, initially confined to the largest scales ($\lambda \sim 30.000$ km, Fig. 1.6b), the evolution of the error spectrum is intriguingly similar to experiment A: the small-amplitude large scale error immediately perturbs the small scales and the following upscale evolution of the error is almost indistinguishable from the case where the errors were imposed directly on the small scales. This behavior is attributed to the decreasing background kinetic energy with decreasing scale, where the error imposed on the large scales becomes significant on small scales first.

In agreement with the dimensional considerations given above, L69 finds that the slope of the background kinetic energy spectrum plays a decisive role in determining the possibility to extend the forecast horizon by confining initial errors to infinitely smaller scales: the predictability time of flows with background spectra equal or steeper than k^{-3} can be extended arbitrarily by making the initial error sufficiently small. In flows with shallower background spectra, however, restricting errors to increasingly (up to infinitesimally) small scales adds ever decreasing increments to the skillful forecast horizon. With the measured $k^{-5/3}$ slope of the horizontal kinetic energy spectrum, mesoscale atmospheric flow falls in the latter category where "*the flap of a sea gull's wings would alter the behavior of all cumulus clouds within about one hour*" (L69) and which thus features limited intrinsic predictability. Note that owing to the homogeneity assumption that underlays the L69-model, this statement in fact only holds for seagulls that are homogeneously distributed over the globe.

The L69-model is—since it is solely based on the barotropic vorticity equation—highly idealized. However, an example of the application of a slightly modified L69-model (Rotunno and Snyder, 2008; Durran and Gingrich, 2014) to the real atmosphere is given in Fig. 1.7. In there, forecasts were computed with the full atmospheric COAMPS (Coupled Ocean-Atmosphere Mesoscale Prediction System; Hodur, 1997) model. 100 simulations were performed with slightly altered initial- and boundary conditions, a so called ensemble forecast. The details of the model configuration are given in Durran and Gingrich (2014). Here, the reader's attention is drawn to the fact that the spectra shown in Fig. 1.7b result from a real-case, full atmospheric model simulations that were initialized with real-atmospheric data. Figure 1.7b shows the mean background (solid) and perturbation (dashed) kinetic energy spectrum. The background kinetic energy spectrum features both the k^{-3} and $k^{-5/3}$ spectral ranges that are also apparent in observational data (see section 1.2.1). The initial error spectrum (here the perturbation is the difference between one ensemble member and the ensemble mean) is depicted a dashed blue line. The error quickly grows in amplitude and scale, whereby successively larger scales are saturated.

Figure 1.7a shows a modified version of the analytical L69-model that can be quantitatively compared to the COAMPS results. In there, the background kinetic energy spectrum as well as the initial error spectrum have been formulated analytically to mimic the real-case COAMPS forecast.
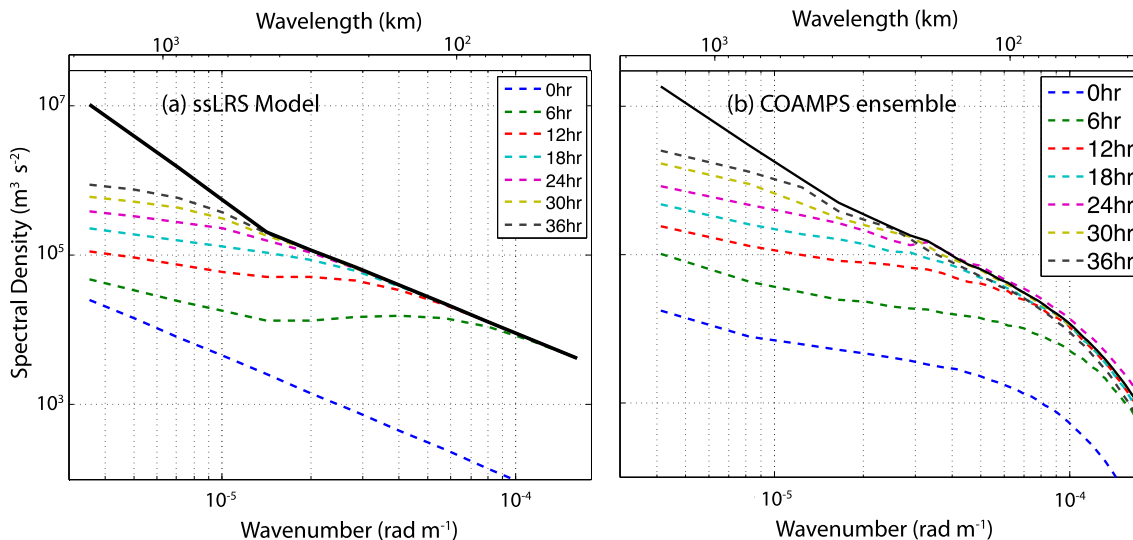
Figure 1.7: Temporal evolution of the spectral error kinetic energy density as a function of wavenumber k in a) a slightly altered and dimensional version of the L69-model and b) COAMPS ensemble-and meridional averaged kinetic energy spectra at 500 hPa initialized at 12 UTC 25 Dec 2010. Background spectra are depicted as solid lines, perturbation spectra are depicted as dashed lines. Figure taken from Durran and Gingrich (2014).

The prediction of the upscale growth of errors with time is again displayed as dashed lines. For this case study, the temporal evolution of the error spectrum of the L69-model (Fig. 1.7a) and the simulation with the full atmospheric model (Fig. 1.7b) compare well. In particular when the simplicity of the L69-model (e.g. solely 24 degrees of freedom) is taken into account.

The three-stage error growth model

Like for the dynamics underlying the atmospheric kinetic energy spectrum (see section 1.2.2), it is not clear to what extent homogeneous turbulence (as introduced in the previous paragraph) is a valid framework to describe error growth in the real atmosphere. In particular, several recent idealized and real-case numerical studies on atmospheric error growth indicate that errors are initially confined to precipitating regions (i.e. the convective scale) and seem to grow much faster in the presence of a convective instability and associated latent heat release at early forecast lead times (Zhang et al., 2002, 2003; Tan et al., 2004; Hohenegger and Schär, 2007; Leoncini et al., 2010; Selz and Craig, 2015a; Sun and Zhang, 2016). This observation suggests that atmospheric error growth may be explicitly tied to the dynamical processes acting on the respective scale range, which are possibly intermittent and localized in nature (e.g. deep moist convection), and to the dominant scale interaction processes (e.g. the interplay between rotational and divergent modes of motion). This notion directly opposes the homogeneity assumption and the unique importance of the slope of the background kinetic energy spectrum in the L69 error growth model.

Based on this understanding and on numerical error growth experiments within a moist baroclinic wave, Zhang et al. (2007, in the following Z07) suggested a three-stage model for atmospheric error growth (see schematic in Fig. 1.8). Note that the explicit dependence of the error growth process on the underlying dominant dynamics renders a mathematical description difficult, as opposed to turbulence models where fundamental simplifications allow for the formulation of a statistical model. Hence, the model proposed by Z07 is at this stage conceptual.

After introducing a small-scale white noise error, Z07 found that errors initially grow in the area of strong precipitating convection associated with diabatic heating. This fast error growth on small convective scales is driven by the convective instability and quickly ($\mathcal{O}(1\,\mathrm{h})$) saturates locally due to a complete displacement of individual convective cells (stage 1, see Fig. 1.8). Starting from moist convection, the small-scale unbalanced errors expand. After around $\mathcal{O}(10\,\mathrm{h})$ errors are apparent in the large-scale balanced (i.e. larger than $1000\,\mathrm{km}$) flow field with a small but significant amplitude (i.e. comparable to differences between 6-12 h forecasts and observations in the global model employed by Zhu and Thorpe, 2006). The errors then grow slowly within the background baroclinic instability (stage 3). More recent results, however, suggest that barotropic interactions might also play a role (Teubler and Riemer, 2016).
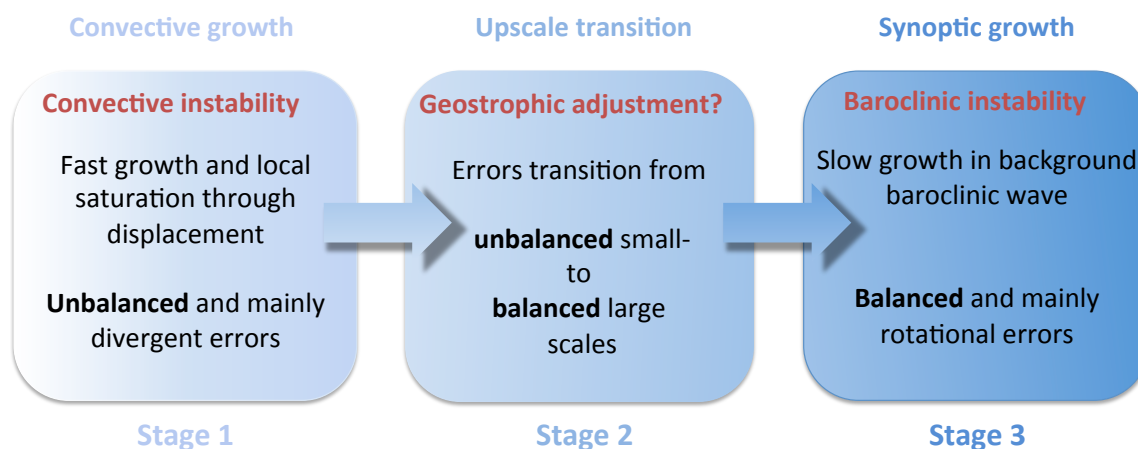
Figure 1.8: Summary of the three-stage conceptual error growth model suggested by Z07.

While error growth properties of stage 1 and 3 seem to be dominated by the convective and baroclinic atmospheric instabilities acting on the small- and large scales respectively, there is no dominant instability acting on the mesoscales (e.g. Markowski and Richardson, 2010, p. 41) and the dynamical mechanism underlying stage 2 of the error growth model as the link between stage 1 and 3 is less clear. However, as introduced in section 1.1.1, small- and large-scale atmospheric motion is characterized by significantly unbalanced, divergent and mainly balanced, rotational modes of motion, respectively. Thus, in the second stage of the upscale error growth process suggested by Z07 the predominant nature of the error transforms from unbalanced and divergent to balanced and rotational. Z07 suggest several mechanisms that potentially underlie the mesoscale error growth dynamics. Examples of such are cold pools at

low levels, instabilities of the front itself and geostrophic adjustment (GA) following convective heating (see section 1.1.1). For the latter possibility, which is examined in this thesis, indications have been found in idealized (Z07) and more realistic (Selz and Craig, 2015b) modeling studies.

Z07 examine the temporal evolution of the ratio of the domain-averaged root-mean square difference (between a perturbed an an unperturbed simulation) of the horizontal divergence and the vertical vorticity. This ratio is also referred to as (bulk) Rossby number Ro and displayed in Fig. 1.9. The field, where small unbalanced scales have been filtered out, initially features a Ro larger than unity (solid black line), indicating that the errors are dominated by unbalanced divergent motion. After around 10 h, however, Ro drops below one, which Z07 interpret as a sign for the growth of a geostrophically balanced flow component to a significant amplitude (i.e. slightly larger than the divergent part). Z07 hypothesize that the geostrophic adjustment might govern this this evolution of a large-scale, balanced flow from an initially unbalanced, small-scale perturbation. The drop of the large-scale (i.e. scales larger 1000 km) Ro below unity at later times (after around 20 h) furthermore emphasizes the nature of the observed error growth as an upscale process.
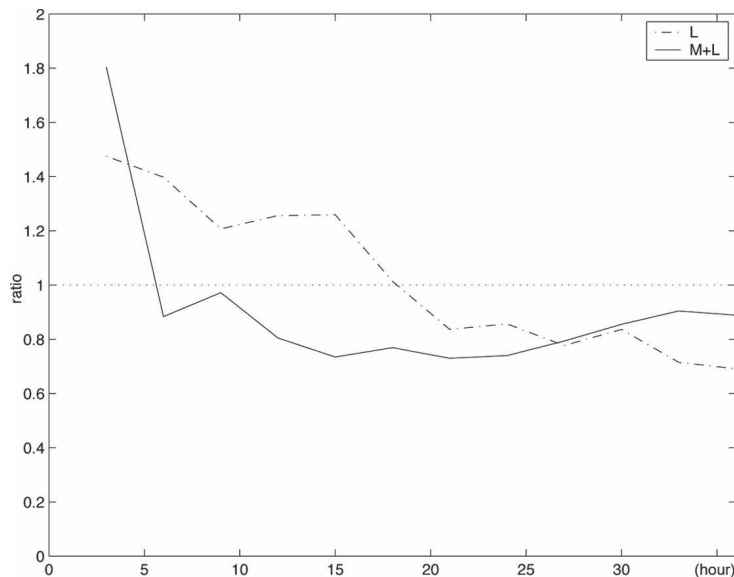
Figure 1.9: Ratio of domain-averaged root-mean square difference of horizontal divergence and domain-averaged root-mean square difference of vertical vorticity as a function of perturbation lead time in a simulation of a moist baroclinic wave (for details see Z07). Solid: scales larger 200 km (M+L). Dashed-dotted: scales larger 1000 km (L). Figure taken from Z07.

Apart from the spin-up of a balanced flow component as found by Z07 (see also section 1.1.1) the impact of a small-scale convective cloud on the surrounding atmosphere consists of a transient gravity wave response. In real-case numerical error growth experiments, Selz and Craig (2015b, in the following SC15) examine the difference total energy (DTE). The DTE is a simple measure for the difference between two fields (as before perturbed and unperturbed) in the vicinity of a cloud (see Fig. 1.10). In the difference field, the black circle indicates the
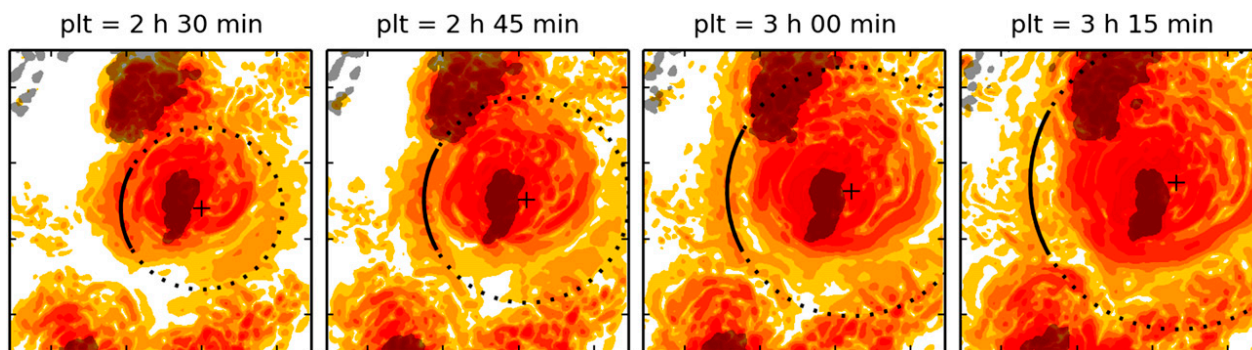
Figure 1.10: Logarithm of difference total energy at $500\,\mathrm{hPa}$ around a convective cell for perturbation lead times $2\,\mathrm{h}\,30\,\mathrm{mins}$ to $3\,\mathrm{h}\,15\,\mathrm{mins}$ in the real-case weather simulation by SC15. The black cross indicates the advection of the center of the convective cell with the background wind. The associated black circle depicts a visual fit to the spreading of the error in a gravity-wave front. Figure taken from SC15.

visual fit of a gravity wave front excited by a convective cloud (black cross). The coincidence of the spreading of the error (red areas of high DTE) from a convective cloud (black cross) with the theoretical typical speed of a gravity wave response (black circle) found by SC15 is interpreted as additional evidence that the GA mechanism might play a major role for the stage 2 of the conceptual error growth model of Z07.

In this section the general problem of predictability of atmospheric flow, particularly in the numerical weather prediction process was introduced. Initially small errors in low-dimensional, simple dynamical systems were shown to grow exponentially and lead to rapidly diverging forecasts. However, in these systems a reduction of the initial error amplitude significantly expands the time interval over which a skillful prediction of the flow evolution is possible. The earth's atmosphere is a much more complex, high-dimensional and non-linear dynamical system. In there, errors of successively smaller amplitude and scale grow increasingly fast. This implies, that a reduction of the initial condition error adds ever smaller increments to the forecast horizon, i.e. the predictability is intrinsically limited. Two theories assessing atmospheric upscale error growth have been introduced: on the one hand, errors are understood to grow in a local cascade in homogeneous, turbulent flow. In there, the predictability time is solely determined by the slope of the background kinetic energy spectrum. On the other hand, atmospheric error growth is interpreted as a three-stage process where each stage is dominated by different underlying dynamics. While the first and last stage of this model appear to be related to the convective and baroclinic instabilities respectively, the dynamical process governing the intermediate stage remains unclear. This thesis explores the geostrophic adjustment following latent heat release within a convective cloud as possibly governing the intermediate stage of the error growth model.

1.4   Summary and Thesis Outline

This chapter described the complexity of atmospheric flow as a chaotic multi-scale dynamical system. In there, processes of various temporal and spatial scales that are characterized by distinct major underlying dynamics interact through the non-linear nature of equations governing atmospheric flow. Micro-scale processes are mainly driven by the convective instability and the dynamics are associated with a significant divergent and unbalanced component. The large synoptic scales, on the other hand, are mainly energized by the baroclinic instability and the dynamics are to a good approximation balanced and rotational. On the intermediate scales, the mesoscales, no major instability acts and neither rotational nor divergent modes of motion are generally predominant. Mesoscale motion is partly forced by scale-interaction processes with the micro- and synoptic-scales. These interactions might be chaotic and turbulent or explicitly dependent on the underlying dynamics. One scale interaction mechanism of the latter kind is the geostrophic adjustment process, whereby a small-scale feature that is associated with a divergent flow component (such as a convective cloud) spins up a balanced rotational flow on much larger scales.

One particularly intriguing feature of the mesoscales is the observed universal power-law behavior of the horizontal kinetic energy spectrum, which is a known feature of homogeneous isotropic turbulence. While mesoscale flow is not characterized by fully developed three-dimensional turbulence, the major dynamics underlying the observed spectral shape remain uncertain. Until now, progress could be made exclusively with statistical theories owing to the lack of a conclusive mathematical approach accounting explicitly for the underlying dynamics. Prevailing theories are particularly in contention about whether the major underlying dynamical agent is predominantly rotational or divergent in nature and to what degree the respective modes of motion interact. In order to further understand the principal dynamics governing the observed kinetic energy spectrum, it is thus essential to decouple rotational and divergent modes of motion from large existing observational data sets. To that end, a one-dimensional Helmholtz-decomposition method has recently been proposed which, however, bases on strong mathematical assumptions of homogeneity and isotropy that do not necessarily hold for atmospheric flow. Before full use can be made of the great potential of this method, the validity of the underlying assumptions needs to be tested.

One major application of meteorological research is the skillful numerical weather prediction which is intrinsically intricate. Low-dimensional nonlinear deterministic systems are known to show a sensitive dependence on the initial condition accuracy through the fast growth of initially small errors. The assessment of atmospheric predictability is further complicated by its chaotic multiscale nature. The problem of predictability of atmospheric flow and the nature of the underlying scale interactions is currently considered from two main perspectives. One approach bases on statistical closure models and homogeneous and isotropic turbulent flow. In there, the slope of the kinetic energy spectrum within which the errors grow exclusively determines the predictability time. For the measured mesoscale slope it is shown, that predictability is intrinsically limited by fast upscale growth of small-amplitude errors. Another, dynamically motivated approach is based on current studies which suggest that small-scale error growth in the atmosphere is not a spatially homogeneous, but rather an inhomogeneous

and intermittent process tied to localized regions of active deep moist convection. Initially small-scale errors are found to expand and attain the large synoptic scales where they grow within the background baroclinic instability. In an intermediate stage, which bridges the convective and baroclinic error growth, the nature of the differences has to transition from small-scale unbalanced (significantly divergent) to larger-scale balanced (mainly rotational). The dynamical mechanism underlying this transition could thus far not conclusively be determined. It was, however, suggested, that the geostrophic adjustment process might play a major role.

This thesis contributes to the presented open research questions regarding the dynamics underlying the atmospheric mesoscale kinetic energy spectrum and the upscale error growth in the following way: in chapter 2 of the present thesis, the suggested method to infer rotational and divergent modes from (one-dimensional) flight-track data is tested in the framework of new high-resolution global model simulations. The study presented in this chapter has mainly been conducted during the authors' six-month stay at the National Center for Atmospheric Research (NCAR) in Boulder, Colorado which was supported by the Advanced Study Program (ASP). Parts of this chapter have been published in Bierdel et al. (2016). In chapters 3 and 4 the relevance of the geostrophic adjustment process to error growth in the atmosphere is assessed. To that end, first an analytical model is developed for an unbalanced buoyancy or divergence forcing that creates a balanced rotational flow (chapter 3). In there, characteristic spatial and temporal scales of the geostrophic adjustment mechanism are deduced and three diagnostics that can be used to identify this process in numerical simulations are proposed. These diagnostics are then employed to extract the geostrophic adjustment process from idealized error growth experiments in a full numerical model of the atmosphere (chapter 4). In a final chapter, the results of the present thesis are summarized and discussed and possible succeeding studies that build on the results of the present thesis are suggested (chapter 5).

Chapter 2

Rotational and Divergent Kinetic Energy Spectra derived from flight-track winds

2.1 Introduction

As elaborated in paragraph 1.2.2 in the introduction, it remains an open question whether the mesoscale horizontal kinetic energy spectrum arises mainly from inertia gravity waves (Van-Zandt, 1982; Dewan, 1997), from two-dimensional vortical flow (Gage, 1979; Lilly, 1983) or stratified turbulence (Lindborg, 2006). To a first approximation, a flow dominated by gravity waves can be distinguished from the other possibilities by an examination of the extent to which the horizontal velocity is associated mainly with horizontal divergence rather than vertical vorticity. The relative contribution of divergent and rotational energy to total kinetic energy is thus a key to understanding the main dynamical agent underlying the mesoscale energy spectrum.

While a variety of atmospheric models, including both general circulation models and models used for numerical weather prediction, exhibit a shallowing of the mesoscale energy spectrum that is in reasonable agreement with the observed energy spectrum (Koshyk and Hamilton, 2001; Skamarock, 2004; Hamilton et al., 2008; Bierdel et al., 2012; Blažica et al., 2013; Brune and Becker, 2013; Burgess et al., 2013; Ricard et al., 2013; Skamarock et al., 2014), these spectra can be sensitive to details of the model configuration (vertical resolution or strength of dissipation; Skamarock, 2004; Brune and Becker, 2013). Particularly the comparison of the spectral energy budgets between different models has shown marked differences (Frehlich and Sharman, 2008; Augier and Lindborg, 2013). Moreover, various models differ widely in their predictions for the relative magnitudes of rotational and divergent velocities at the tropospheric mesoscale. Blažica et al. (2013) examine the numerical weather prediction model ALADIN (Aire Limitée Adaptation Dynamique Développement International; Fischer et al., 2005) and find an equipartition of mesoscale rotational and divergent kinetic energy in the free troposphere of the midlatitudes. These findings are supported by the evaluation of data from global circulation models (GCMs) in Skamarock et al. (2014) and Koshyk and Hamilton (2001). Contrarily, Hamilton et al. (2008) and Koshyk et al. (1999) find in several (high

resolution) GCM simulations that upper tropospheric kinetic energy is dominated by the rotational component. Thus, observational estimates of the energy spectra for the rotational and divergent flow will also be useful in identifying which numerical models produce mesoscale shallowing of the kinetic energy for the correct dynamical reasons.

Many observational studies addressing different aspects of the mesoscale energy spectrum with respect to geographical region and vertical levels found signs of mesoscale spectra dominated by either quasi two-dimensional motion (Gage and Nastrom, 1985; Cho et al., 1999) or unbalanced gravity wave motions (Vincent and Eckermann, 1990; Bacmeister et al., 1996; Cho et al., 1999). Commercial aircraft observations such as the Measurement of Ozone and Water Vapor by Airbus In-Service Aircraft (MOZAIC; Marenco et al., 1998) provide large global datasets of along- and across-track wind velocity measurements. Perhaps surprisingly, one-dimensional transects of horizontal wind components are useful for estimating the spectra of the divergent and rotational velocities. A method for doing this was first suggested by Lindborg (2007, hereafter L07), though basic results are also implicit in early work such as Charney (1971). More recently, Bühler et al. (2014, hereafter B14) and Lindborg (2015, hereafter L15) have proposed approaches that are computationally simpler to implement than L07 and do not involve second-order differentiation of measurement data which might introduce errors in the results. Both approaches have been applied to MOZAIC observations (Callies et al., 2014; Lindborg, 2015).

The B14 and L15 approaches follow from relations between the longitudinal-transverse and Helmholtz decompositions, which in turn require strong assumptions on the underlying flow, namely horizontal homogeneity and isotropy. In the real atmosphere, these assumptions of course hold only approximately and the two approaches may be relatively more or less sensitive to violations of the assumptions of homogeneity and isotropy. In this chapter, the the accuracy of the B14 and L15 approaches for realistic flows is evaluated by applying them to numerical output from the global atmospheric Model for Prediction Across Scales (MPAS, Skamarock et al., 2012), where the decomposition of the velocity into rotational and divergent components may be done unambiguously. When applied to aircraft observations (as in Callies et al. (2014) and L15), these techniques require an additional assumption, which are not tested here, namely that measured velocity time series can be converted to spatial transects using the mean air speed of the plane.

The comparison of the two approaches presented in this chapter is also motivated by the different ratios of divergent to rotational spectral energy on the mesoscales that have been found when applying the B14 and L15 implementations to MOZAIC data. Callies et al. (2014, hereafter C14) apply the B14 approach and find that velocity spectra at the mesoscales are dominated by the divergent contribution, which leads them to the conclusion that inertia-gravity waves likely account for the mesoscale energy spectrum. Contrarily, L15 finds the opposite result, with mesoscale spectra dominated by the rotational contribution, and concludes that inertia-gravity waves can be ruled out as important to the atmospheric mesoscale energy spectrum. Besides the differences in the details of their implementations, C14 and L15 also make different choices in their handling and processing of the observations. Thus, the sensitivity of the decomposition to some of these choices in the context of numerical simulations is explored, though a detailed reconstruction of either study is not attempted.

This chapter is structured as follows: in section 2.2, the configuration of the MPAS model and the simulated period as well as the procedure of the spectral calculations and the B14 and L15 approaches are described. The results of this study for global data are presented in section 2.3. General features of the kinetic, rotational and divergent energy spectra in the MPAS model are reviewed and the estimates of the respective energy components by B14 and L15 and the according errors are discussed. In section 2.4, it is shown that the different results of C14 and L15 for the dominance of rotational or divergent energies on the mesoscales in the MOZAIC data can be qualitatively reproduced by considering different subsets of the MPAS data. This chapter concludes with a summary in section 2.5. The results of this chapter have partly been published in Bierdel et al. (2016).

2.2 Data and methods

The B14 and L15 approaches are tested by applying them to output from global atmospheric simulations. This section describes the numerical simulations, the various spectra that are computed from them and the B14 and L15 implementations of the decomposition method.

2.2.1 The numerical simulation and computation of its spectra

In order to test the B14 and L15 approaches, output produced by the fully compressible non-hydrostatic atmospheric global Model for Prediction Across Scales (MPAS), which is described in detail in Skamarock et al. (2012), is used. The MPAS solver is discretized on a spherical centroidal Voronoi mesh. The results presented in this chapter are computed over days 5-14 of a 15 day MPAS simulation initialized at 0000 UTC 15 January 2009, using a quasi-uniform mesh with an average cell-center spacing of 15 km. Spectra from the model generally spin up within 18 h and omitting the first 5 days of simulations insures that the results are not influenced by such spin up. The simulation is identical to the 15-km simulation of Skamarock et al. (2014, hereafter S14) and a detailed description of the model configuration, the physical parameterizations, the integration scheme and the numerical diffusion used can be found there.

The B14 and L15 approaches provide estimates of the spectra of rotational and divergent energy, using one-dimensional power spectra of across- and along-track wind velocities as input. These spectra will be denoted by $E_R(p)$, $E_D(p)$, $E_T(p)$ and $E_L(p)$ respectively, where p is the along-track wavenumber. In the present chapter those spectra are calculated from the MPAS output as follows: the data is available on an unstructured grid that lacks a global coordinate system and is in a first step interpolated to a regular latitude-longitude grid. To that end, the Delaunay triangular mesh as the dual of the Voronoi mesh is used, and barycentric interpolation is used within the Delaunay triangle that contains a given latitude-longitude point (as described in S14). This interpolation is performed on the interpolated height levels 8.5 km, 9.5 km, 10.5 km, 16 km, 17 km and 18 km, where model height surfaces are considered almost horizontal. Tropospheric results (TROP) are averaged over the first three levels. In this chapter stratospheric heights are furthermore included in order to assess the height-dependence of the obtained spectra. The stratosphere is the atmospheric layer between the tropopause

and around $50\,\mathrm{km}$ height. In there, dynamics are fundamentally distinct from the troposphere and mainly determined by zonal winds that interact with waves that propagate upward from the troposphere (e.g. Ruzmaikin et al., 2003). An average over the latter three levels is in this chapter denoted as STRAT ($16 - 18\,\mathrm{km}$). As a second step, the gridded one-dimensional transects are extracted from the model output along constant latitude or longitude and these are rendered periodic following Errico (1985). A discrete one-dimensional Fourier transform is then applied along the transects and the resulting spectra are averaged over all longitudes or latitudes respectively. In this chapter, longitudinal and latitudinal wavenumbers will be denoted by k and l, respectively. All spectra displayed as a function of k will result from one-dimensional Fourier transforms taken along circles of constant latitude averaged over all latitudes. A dependence on l will indicate that spectra have been calculated along circles of constant latitudes, and along constant longitudes and averaged (scales larger than the minimum l are neglected in k-spectra). All spectra presented in this chapter are computed at 6-hourly intervals and further averaged over the 10 days of simulation (40 time slots in total).

In order to compare the results of B14 and L15 to E_R and E_D obtained from full model output, the velocity field is decomposed globally into rotational and divergent contributions. To that end, a spherical harmonics transform is applied to the fields of vertical vorticity and horizontal divergence on the regular latitude-longitude grid. The associated spectral representation of the stream function and the velocity potential, and of the rotational and divergent components of the horizontal wind can then be easily calculated and an inverse spherical harmonic transform gives the rotational and divergent wind components in real space. Those fields are then detrended in the latitudinal direction (even for global data the latitude range is restricted, see explanation below) and a two-dimensional Fourier transform is applied. In order to obtain a one-dimensional spectrum as a function of the along-track wavenumber, a direction for the one-dimensional spectrum (either latitudinal or longitudinal) is chosen and the squared absolute values of the Fourier coefficients for both along- and across-track velocities are summed over the wavenumber in the across-track direction.

When taking discrete Fourier transforms of one-dimensional transects along circles of constant latitude of the interpolated regular latitude-longitude grid, issues related to the stretching of segments at higher latitudes to longer physical distances will arise. The influence of this geometric effect has been checked by comparing results from spectral calculations on the full, global latitude-longitude grid (including regions at high latitudes where the effect is expected to be significantly more pronounced) to those from a grid restricted to latitudes between 60°S and 60°N. Comparing the obtained spectra with spectra computed from spherical harmonic coefficients for the full global fields, however, indicates that this effect changes neither the results nor the performance of the method qualitatively. The results shown in the present chapter are nevertheless restricted to the latitude range $60°\,\mathrm{S}$ to $60°\,\mathrm{N}$ to assure that the geometric effect near the poles is neglected.

2.2.2   The Bühler and Lindborg approaches

On the sphere, the two-dimensional Helmholtz-decomposition allows for the representation of any horizontal flow field $\boldsymbol{v}_h$ in terms of components associated with the divergence and the rotation of the flow. It reads (e.g. Bott and Zdunkowski, 2003, p. 217)

$$\boldsymbol{v}_h = \boldsymbol{v}_{h,R} + \boldsymbol{v}_{h,D} = -\nabla \times (\boldsymbol{e}_z \psi) + \nabla \phi \,,$$

where $\boldsymbol{v}_{h,R}$ and $\boldsymbol{v}_{h,D}$ are the rotational and divergent components of the horizontal wind, ∇ denotes the horizontal gradient operator, $\boldsymbol{e}_z$ is the vertical unit vector and ψ and ϕ are the stream function and velocity potential. All velocity components are defined in the x-y-plane with associated wavenumbers p and q (in order to avoid confusion with the wavenumbers k and l that will denote longitudinal and latitudinal wavenumbers in the MPAS data), where x is the along-track direction. Furthermore, the altitude z as well as the time t are considered constant. Apart from the decomposition into rotational and divergent modes, a horizontal flow field sampled along a one-dimensional flight track can also be regarded as composed of an along- and across-track wind component, $\boldsymbol{v}_L$ and $\boldsymbol{v}_T$. The one-dimensional kinetic energy spectrum $E_K(p)$, can thus be expressed as

$$E_K(p) = E_T(p) + E_L(p) = E_D(p) + E_R(p) \,. \tag{2.1}$$

The p-dependence of one-dimensional spectral quantities will be omitted in the remainder of this chapter for simplicity. Dependencies other than on p will be denoted explicitly. Assuming the flow is horizontally homogeneous and isotropic, and given the unique and exact decomposition (2.1), then E_R and E_D can be related to E_T and E_L. The equations from B14 and L15, given in the next sections, are mathematically equivalent formulations of these relations and thus the B14 and L15 approaches can be considered different implementations of the same method.

The Bühler approach

Under the assumption that the stream function ψ and velocity potential ϕ are isotropic random functions, B14 derive relationships between E_L and E_T and the two-dimensional isotropic spectra of ψ and ϕ. The resulting coupled ordinary differential equations (ODEs) take a simpler form when the y-derivatives of the velocity potential and stream function spectra, D^ϕ and D^ψ, are introduced as auxiliary functions, with the result

$$p\frac{d}{dp}D^\psi(p) = D^\phi(p) - E_T(p) \tag{2.2}$$

$$p\frac{d}{dp}D^\phi(p) = D^\psi(p) - E_L(p) \,, \tag{2.3}$$

where the subscripts L and T denote quantities derived from along- and across-track wind velocities as before.

The ODE system (2.2)-(2.3) is solved for D^ψ and D^ϕ numerically under the boundary condition that D^ψ and D^ϕ tend to zero for $p \to \infty$. Note that B14 also suggest a closed form solution

which implies the interpolation of the input E_L and E_T spectra to a logarithmic grid. However, to avoid the potential errors arising from this additional step (2.2)-(2.3) are solved numerically on the regular p-grid. The required amount of smoothing depends on the level of noise in the data (i.e. sample size) and an averaging over wavenumber bins of width $5 \cdot 10^{-8}\,\mathrm{m}^{-1}$ is found to be sufficient for the utilized data.

Adding (2.2) and (2.3) and regrouping the terms to components only associated with the stream function or velocity potential leads to the kinetic energy spectra of rotational and divergent winds

$$E_R(p) = D^{\psi}(p) - p\frac{d}{dp}D^{\psi}(p) \tag{2.4}$$

$$E_D(p) = D^{\phi}(p) - p\frac{d}{dp}D^{\phi}(p)\,, \tag{2.5}$$

where the subscripts R and D denote quantities derived from rotational and divergent wind velocities (see (2.27) in B14). Note that the boundary condition that D^{ψ} and D^{ϕ} tend to zero for $p \to \infty$ implies that E_R and E_D tend to zero for largest wavenumbers. The described additional smoothing of the input E_L and E_T spectra has a negligible impact on the results (see paragraph 2.3.2).

The Lindborg approach

The original approach of L07 begins from relationships between the two-point correlation function of vertical vorticity and horizontal divergence and the along- and across-track velocity correlation. As in B14, statistical isotropy and homogeneity are assumed. The desired relationships between the longitudinal-transverse and Helmholtz decompositions are derived in L07, but the calculation of the two-point correlation functions of vertical vorticity and horizontal divergence involves second-order differentiation of measurement data, leaving the estimate sensitive to noise.

L15 revisits the formulas found in L07 and derives two coupled ODEs that relate the two-point correlation functions of rotational and divergent velocities (R_{rr} and R_{dd}) to the correlation of longitudinal and transverse velocities (R_{ll} and R_{tt}). Under the boundary condition that the correlation functions tend to zero for infinite separation distances r, the respective relationships can be integrated over r and L15 finds

$$R_{rr} = R_{tt} - \int_r^{\infty} \frac{1}{r}(R_{tt} - R_{ll})\,dr$$

$$R_{dd} = R_{ll} + \int_r^{\infty} \frac{1}{r}(R_{tt} - R_{ll})\,dr\,.$$

Using the relation between structure functions and spectra for isotropic, homogeneous fields then gives formulas relating the rotational and divergent energy spectra to the spectra of horizontal wind velocities ((2.11) and (2.12) in L15)

$$E_R(p) = E_T(p) + \frac{1}{p} \int_p^\infty (E_T(p) - E_L(p)) \, dp \qquad (2.6)$$

$$E_D(p) = E_L(p) - \frac{1}{p} \int_p^\infty (E_T(p) - E_L(p)) \, dp \,, \qquad (2.7)$$

where definitions are as before. The relationships established by L15 relate E_R and E_D to E_L and E_T in a simpler way than L07 and B14 and can be implemented with a simple trapezoidal rule where no preprocessing of the input data is necessary. For comparison with the B14 approach the spectral formulas (2.6) and (2.7) will be examined in the present chapter.

2.3 Spectra obtained from global data

In the following, general characteristics of E_K, E_D and E_R as calculated from MPAS data (i.e. two-dimensional fields) are discussed first. $E_{D,R}^B$ refer to results obtained from solving (2.4) and (2.5) (as derived in B14) numerically and $E_{D,R}^L$ are calculated from (2.6) and (2.7) using a trapezoidal rule as in L15. Quantities without the superscript 'L' or 'B' refer to results obtained from the two-dimensional data and are then compared to the respective $E_{D,R}^{B,L}$. In a third part the large scale error of the two approaches is assessed.

E_K, E_D and E_R calculated for the considered period of time have already been presented in S14. S14 discuss in detail the fully global results of MPAS simulations with 3 km horizontal resolution as opposed to this study where 15 km data is calculated on a narrower latitude band (60°S − 60°N) and rendered periodic in latitudinal direction. S14 furthermore use a global spherical harmonic decomposition and a summation over spherical harmonics with the same total wavenumber. Since the examined data is on a limited area a two-dimensional Fourier transform is applied to the fields and results are displayed as a function of along-track wavenumber for comparability with the B14 and L15 studies. The S14 methodology for the calculation of one-dimensional spectra is thus slightly different from the approach utilized here and general features of the spectra will be briefly reviewed.

2.3.1 General features of the spectra

E_K is displayed as a function of longitudinal wavenumber k as red line in Fig. 2.1 for TROP (left) and STRAT (right). As in S14, the observed features of the atmospheric energy spectrum, with a −3 scaling at larger scales that merges into a shallower spectrum for scales smaller than around 500 km, is well reproduced in both height regimes. The model's accurate reproduction of the flow on small scales is bounded by the effective resolution, i.e. the scale at which model filter effects become important. From a comparison with higher resolved MPAS simulations, S14 estimate the effective resolution of the model in this configuration as 4 − 6
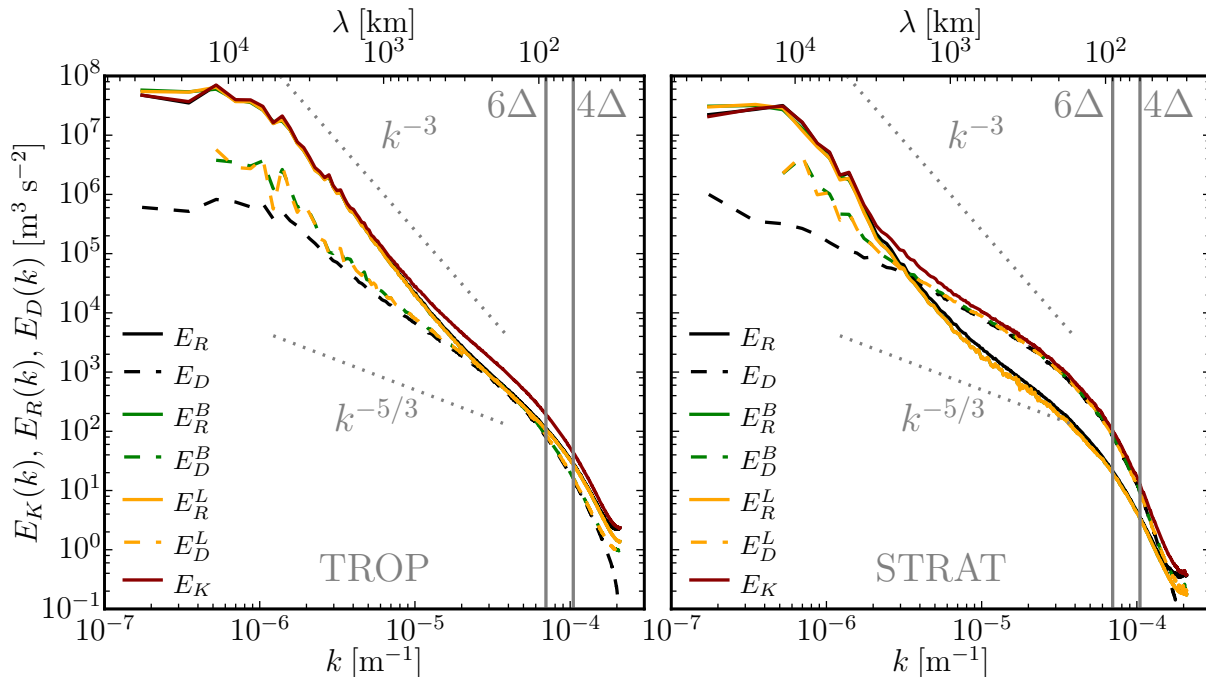
Figure 2.1: E_K, E_R and E_D as calculated from the full MPAS data set and $E_{D,R}^{B,L}$ for TROP (left) and STRAT (right) as a function of k in double logarithmic space. The spectra are taken along longitudinal bands and then averaged over latitudes between 60°S and 60°N.

times the horizontal grid spacing Δ (see solid gray vertical lines in Fig. 2.1). Thus, spectra for the evaluated MPAS data will not be considered accurate on scales smaller than 100 km and the term 'mesoscales' will in the remainder of this chapter refer to the wavelength range from 100 km to 1000 km. As discussed in previous modeling studies (e.g.. Hamilton et al., 2008), the shallowing of E_K on largest (global) scales is considered a physical feature of the energy spectrum of the real atmosphere (Boer and Shepherd, 1983), but should be interpreted with care since the shape of the spectrum results from an average over few Fourier modes and is thus highly variable.

As seen in S14, the mesoscale transition, i.e. the scale where the shape of the E_K spectrum changes from a steeper synoptic scale to a shallower mesoscale slope, is at somewhat longer wavelengths in STRAT ($600 - 800$km) than in TROP ($300 - 500$ km). This shift of the transition to larger scales with height is consistent with previous studies with global models (Koshyk and Hamilton, 2001; Burgess et al., 2013) and with idealized simulations of baroclinic waves (Waite and Snyder, 2013). It appears to arise from upward propagating inertia-gravity waves, where the divergent component of the flow maintains its amplitude while the rotational component decays.

In Fig. 2.2, the fraction of E_D of E_K is displayed in percentage terms as a function of longitudinal wavenumber for TROP (left) and STRAT (right). In TROP, E_R dominates E_K for all wavenumbers. For scales larger than 1000 km, E_D amounts to about 10% of E_K. The associated dominance of E_R leads to the observed -3 wavenumber dependence of E_K on the large scales. From Fig. 2.1 it can be seen that the E_D spectrum features a significantly shal-
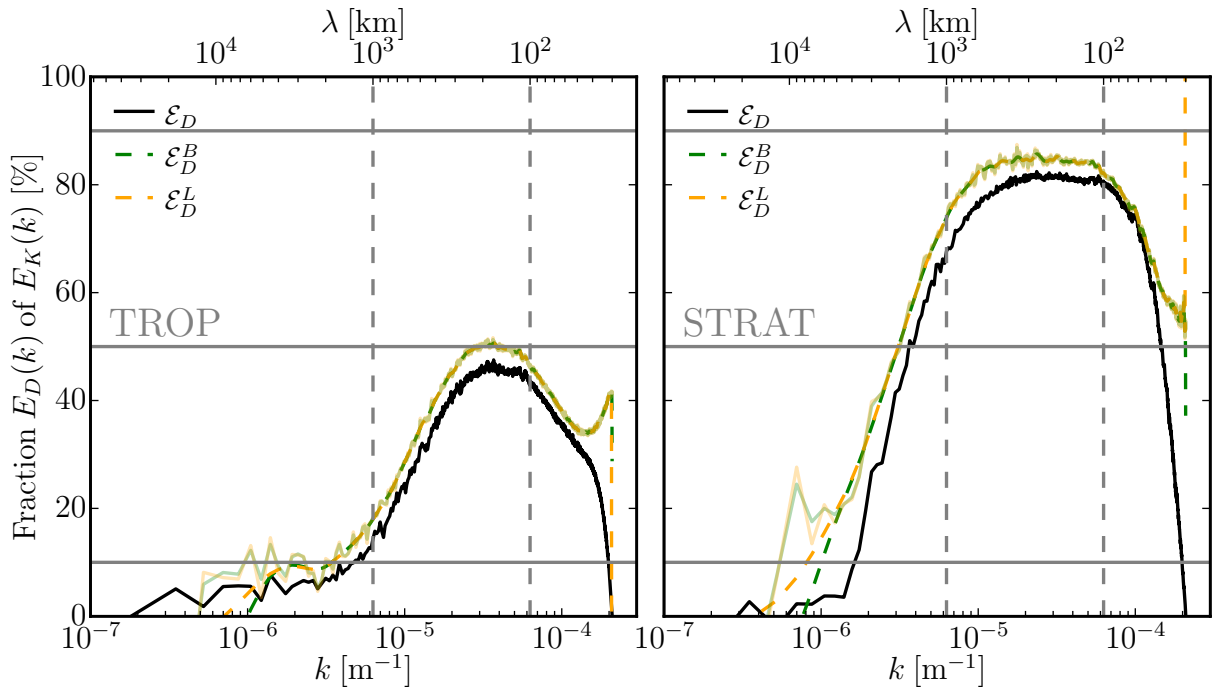
Figure 2.2: Fraction of E_D of E_K ($\mathcal{E}$) in % from Fig. 2.1 for TROP (left) and STRAT (right). Solid gray horizontal lines demark 10%, 50% and 90%, dashed vertical gray lines indicate horizontal scales of 100 km and 1000 km for orientation. Dashed green and yellow lines are moving averages over three wavenumber bins of associated opaque solid lines.

lower slope (closer to $-5/3$). On the mesoscales, the contribution of E_D to E_K increases with decreasing scale and accounts for up to 45% of E_K with an average ratio $E_D/E_R \sim 0.7$. In contrast, the STRAT mesoscales are characterized by a dominance of divergent motions, where E_D makes up 80% of E_K on scales of a couple of hundreds of kilometers. The STRAT E_R and E_D spectra cross at a scale of around 2000 km, leading to a sharper mesoscale transition that occurs at longer wavelengths than in TROP. The mean mesoscale (i.e. averaged over all wavenumbers in the mesoscale range 100 km − 1000 km) ratio E_D/E_R is found to be 4.1.

Previous modeling studies disagree concerning the ratio of E_D to E_R on the atmospheric mesoscales. As in this study, S14 find an equipartition of energy between E_D and E_R in the upper tropospheric mesoscales; earlier studies, such as Koshyk and Hamilton (2001), hint at a similar result though they do not resolve the majority of the mesoscale range. Blažica et al. (2013) examine the height dependence of the contribution of divergent to kinetic energy in the numerical weather prediction model ALADIN and find that divergent energy amounts to about 50% of kinetic energy in the free troposphere. Hamilton et al. (2008), in contrast, find in simulations of a high resolution GCM that near the tropopause the rotational dominates over the divergent energy on the mesoscales, with $E_R \sim 4\,E_D$. In the stratosphere, model simulations generally agree that transition to a flatter mesoscale spectrum occurs at larger scales than in the troposphere and that E_D increases relative to E_R (Koshyk and Hamilton, 2001; Hamilton et al., 2008; Blažica et al., 2013; Burgess et al., 2013; Waite and Snyder, 2013; Skamarock et al., 2014). Several studies (Koshyk and Hamilton, 2001; Burgess et al., 2013;

Waite and Snyder, 2013) attribute these characteristics of the stratospheric energy spectrum to mesoscale inertia-gravity waves propagating upward from the troposphere, though Augier and Lindborg (2013) compare the spectral energy budgets in two different models and show that vertical propagation of mesoscale waves is important in only one of them.

2.3.2   Estimate from B14 and L15

$E_D^{B,L}$ and $E_R^{B,L}$ are displayed as green and yellow lines in Fig. 2.1. The two approaches produce almost identical results and work very well. Due to the different solution technique and the required smoothness of the input data, $E_{D,R}^B$ are marginally smoother than $E_{D,R}^L$. When plotted on a traditional log-log scale the results are almost indistinguishable from the correct answer (black lines). The underlying mathematical assumptions of isotropy and homogeneity must be well satisfied, at least when data is aggregated over large areas.
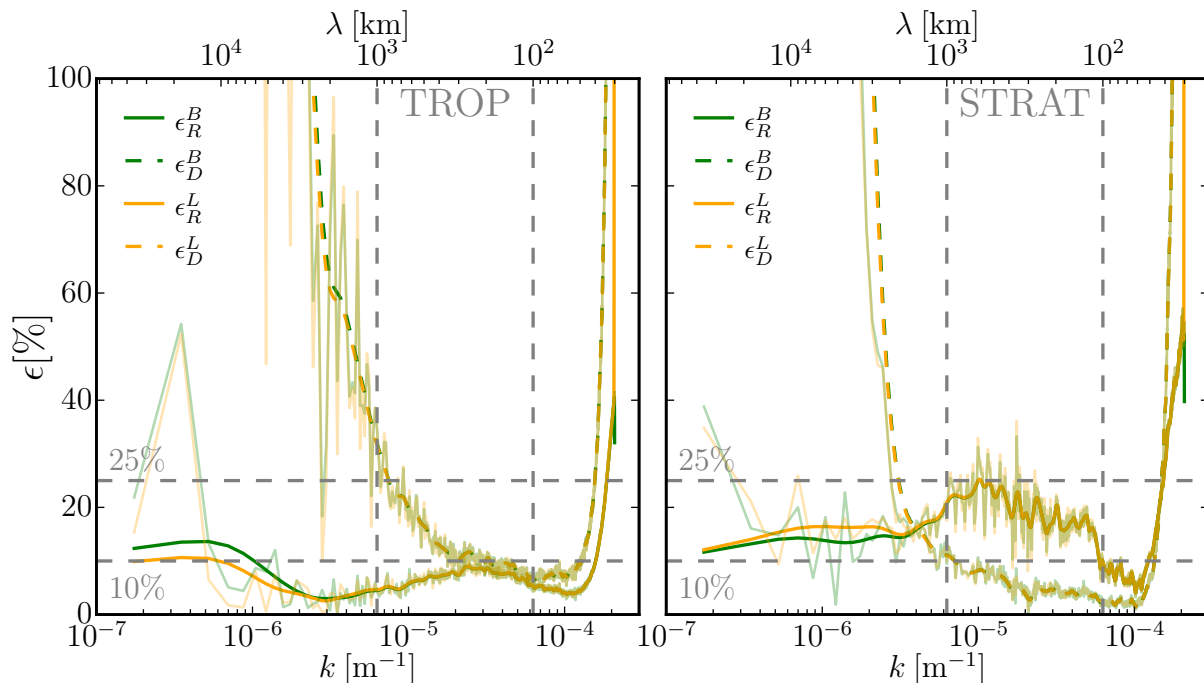
Figure 2.3: Absolute error ϵ (in %) of $E_{D,R}^{B,L}$ from Fig. 2.1 for TROP (left) and STRAT (right). Gray horizontal lines indicate 10% and 25%. Dashed and solid green and yellow lines are moving averages as in Fig. 2.2.

The absolute errors of B14 and L15 are displayed in Fig. 2.3. The error is defined as the absolute value of the difference between $E_D^{B,L}$ and $E_R^{B,L}$ and the corresponding energy component from MPAS data, normalized by the latter, and provides a quantitative view on the quality of the estimates of B14 and L15. Mean mesoscale errors of $E_D^{B,L}$ and $E_R^{B,L}$ amount to 11.0% and 7.2% (TROP) and 4.7% and 17.7% (STRAT) respectively. The largest errors are found in $E_D^{B,L}$ on the largest scales and in both energy components near the grid scale. It furthermore appears that the smaller energy component is estimated systematically worse.

In Fig. 2.1, $E_D^{B,L}$ takes negative values for the two largest Fourier modes and is thus not displayed on the log-log scaled plot. L15 also noticed this unphysical behavior and this issue will be addressed in paragraph 2.3.3. The errors on the small-scale end of the spectra in Fig. 2.1 arise for Fourier modes on the grid scale. Since, as pointed out before, evaluated MPAS spectra are not accurate on scales smaller than 100 km due to the strong impact of model filter effects these errors will not be discussed further.

In Fig. 2.2 the ratio E_D/E_K is displayed for TROP (left) and STRAT (right). The discussed errors are in fact small enough that the ratio is also estimated well with values $E_D^{B,L}/E_K^{B,L} \sim 0.9$ in TROP and 5.2 in STRAT (compared to 0.7 and 4.1, respectively in the MPAS data). The B14 and L15 techniques should thus be able to provide a strong observational check on the mesoscale behavior of numerical models. As will be discussed in section 2.4, however, careful attention must be paid to which subset (i.e. latitude and height) of observations is considered.

2.3.3   Assessment of errors

A striking feature of Figs. 2.1 and 2.3 is the relatively large error of $E_D^{B,L}$ on large scales. This might result from violation of the underlying assumptions of B14 and L15 (see paragraph 2.2.2), but another possibility is that, because of the small amplitude of E_D relative to E_R, $E_D^{B,L}$ may be contaminated by small noise in E_R. This issue is addressed by calculating $E_D^{B,L}$ as in paragraph 2.3.2, but beginning from either purely rotational ($\boldsymbol{v}_h = \boldsymbol{v}_{h,R}$) or purely divergent ($\boldsymbol{v}_h = \boldsymbol{v}_{h,D}$) components of the original MPAS velocities.

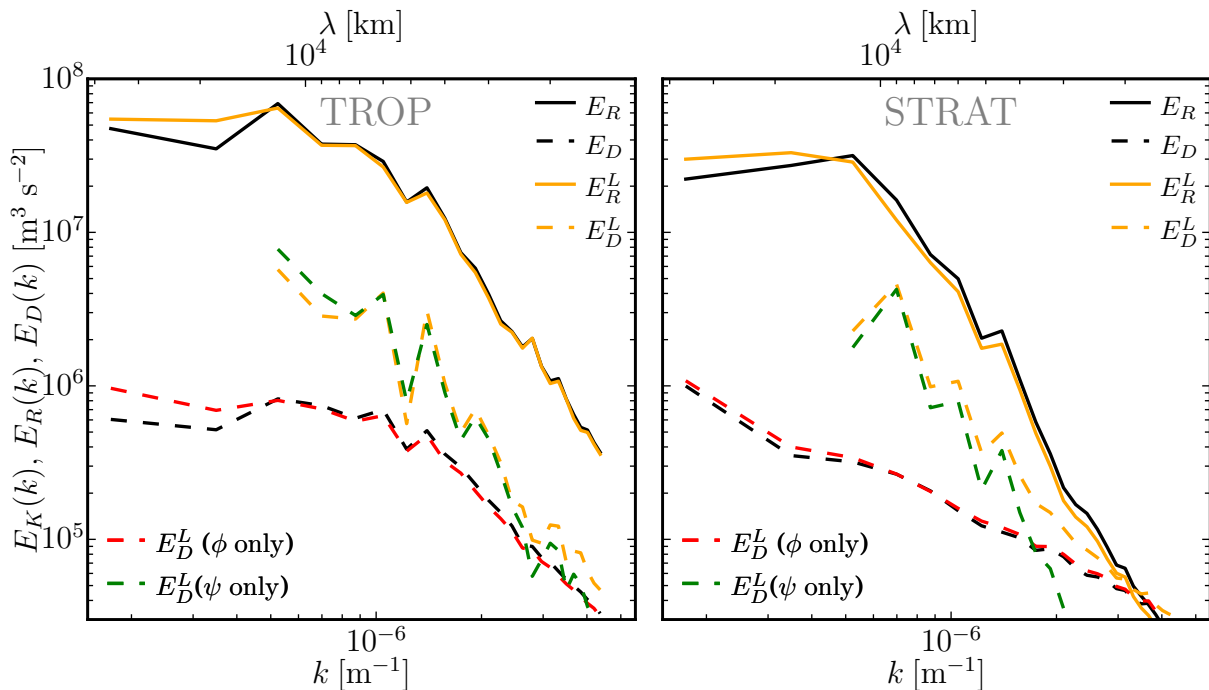**Figure 2.4:** E_R and E_D as calculated from the full MPAS dataset and $E_{D,R}^L$ from the full flow field as well as $E_{D,R}^L$ from $\boldsymbol{v}_{h,D}$ alone or $\boldsymbol{v}_{h,R}$ alone, for TROP (left) and STRAT (right). Scales larger ~ 1000 km are shown.

If the large-scale error of $E_D^{B,L}$ is related to a bad signal-to-noise ratio it is expected to be significantly reduced for the purely divergent flow.

In Fig. 2.4, $E_{D,R}$ and $E_{D,R}^L$ are displayed for scales larger than $\sim 1000\,\mathrm{km}$ for the full flow field (as Fig. 2.1) and E_D^L from $\boldsymbol{v}_{h,D}$ alone or $\boldsymbol{v}_{h,R}$ alone. All estimates of the B14 technique are quantitatively and qualitatively almost identical to the corresponding L15 estimates and are not shown for reasons of clarity. As discussed in paragraph 2.3.2, the difference between $E_D^{B,L}$ and E_D grows with increasing scale in TROP and STRAT (see black and yellow dashed lines in Fig. 2.4). When computed from $\boldsymbol{v}_{h,R}$ alone (dashed green line), E_D^L qualitatively resembles the estimate from the full flow field (dashed yellow line). Note especially that $E_D^{B,L}$ is estimated with significant amplitude although the divergent wind is set to zero in the input data. $E_D^{B,L}$ computed from $\boldsymbol{v}_{h,D}$ alone (dashed red line), however, compares significantly better to E_D. These results clearly show that the poor retrieval of E_D by B14 and L15 on large scales is related to a bad signal-to-noise ratio: the big error of $E_D^{B,L}$ is caused by small errors in E_R on large scales that contaminate the divergent component, which is small compared to the rotational component, and not by errors arising from violations of the underlying assumptions on the flow, such as isotropy and homogeneity.

An analogous test of the dependence of errors of the E_R estimate for from either $\boldsymbol{v}_{h,R}$ or $\boldsymbol{v}_{h,D}$ alone (not shown) does not give results as clear as those for E_D. The error of the E_R estimate is in particular neither in general nor on a certain scale range drastically reduced if E_R is computed from $\boldsymbol{v}_{h,R}$ alone. This points to other error sources being more relevant to the E_R estimate than the signal-to-noise-ratio. This issue warrants further investigation.

2.4   Exploring the results of C14 and L15

C14 and L15 applied the B14 and L15 approaches respectively to the global MOZAIC commercial aircraft data set. They found different ratios E_D/E_R on the atmospheric mesoscales and drew differing conclusions regarding the dominant dynamical character on this scale range. In this section, the different results of C14 and L15 are assessed with the MPAS data.

2.4.1   Comparing C14 and L15

C14 find from the application of B14 to MOZAIC data, that the rotational component dominates the energy spectrum on the synoptic scales and that E_D becomes of the same order of magnitude as E_R near the transition scale. On the mesoscales, C14 find a slight dominance of E_D over E_R. The authors conclude from this that mesoscale dynamics are governed by unbalanced ageostrophic inertia gravity wave (IGW) motions and that the transition in the E_K spectrum originates from IGWs becoming dominant on the respective scales. According to C14, an IGW field that is dominated by near inertial waves is expected to feature a ratio $E_D/E_R \sim \omega^2/f^2$ of about unity (with f Coriolis parameter and frequency ω). The dynamic picture that emerges from the C14 results is a forward enstrophy cascade forced by geostrophic synoptic scale baroclinic disturbances, which is masked by inertia gravity waves for scales smaller than about $500\,\mathrm{km}$. In contrast, L15 finds, based on a structure function analysis of MOZAIC data that E_R dominates over E_D on the mesoscales at all heights and

with largest values $E_D/E_R \sim 0.33$ in the upper troposphere. Arguing that any realistic IGW frequency distribution features a ratio E_D/E_R significantly larger than unity, L15 concludes that gravity waves can be ruled out as being the major dynamical feature leading to the observed atmospheric energy spectrum. There are two potential causes of the disagreement between the C14 and L15 results: first, the different results can arise from different estimates $E_{D,R}^{B,L}$ from given E_T and E_L, i.e. there are inherent limitations in the accuracy of the diagnostic methods. This possibility is ruled out by the results of paragraph 2.3.2. In what follows, the second possibility, that the difference between the results of C14 and L15 arises from differences in their processing of the MOZAIC measurement data, is examined.

C14 use MOZAIC data obtained in 2002-2010 and utilize only flight segments that are longer than 6000 km and lie completely in the northern hemispheric midlatitudes (30°N-60°N). These criteria reduce the number of evaluated segments to 458 and select mainly flights that are more or less along tracks at constant latitude. The data are not separated into upper-tropospheric and lower-stratospheric portions, but rather all flight levels are averaged together. L15 uses the 1994-1997 MOZAIC data set without restrictions concerning the segment length (leading to a smaller evaluated scale range than in C14) or location of the flight track. The resulting 7630 randomly oriented flight segments are separated according to ozone levels into nominally tropospheric (< 100 ppbv) and stratospheric (> 200 ppbv) heights and averaged globally.

2.4.2 MPAS results

Since C14 and L15 use different subsets of the MOZAIC data, their different conclusions with regard to the mesoscale ratio E_D/E_R are not necessarily contradictory. By evaluating only long flights in a narrow latitude band, C14 only include spectra with a longitudinal wavenumber dependence in a rather homogeneous flow field. The discussion of the vertical dependence of E_D/E_R and the transition scale from synoptic to mesoscale flow regimes in paragraph 2.3.1 further indicates that averaging over tropospheric and stratospheric height regions might lead to different results than separating those heights. Furthermore, L15 averages over 16 times more flight segments which are more randomly oriented and distributed over the globe. This might render the evaluated data more isotropic and smooth. The latitudinal dependence of energy spectra and the accuracy of the isotropy assumption on the flow (Nastrom and Gage, 1985; Cho and Lindborg, 2001) might also lead to different results when spectra are averaged over the globe as opposed to a narrow latitudinal band.

Next, spectral shapes and estimates of E_D/E_R computed by applying the B14 or L15 techniques to subsets of the MPAS data that mimic those used by C14 and L15 are compared. To mimic the C14 setup, one-dimensional spectra are taken along constant latitudes and averaged over latitudes in the range 30°N-60°N and TROP (C14 setup). For the L15 setup, the input spectra are calculated globally along bands of constant latitude and longitude and averaged separately for TROP and STRAT. Note that for the L15 setup the resulting spectra are displayed over a smaller range of wavenumbers, since the latitudinal tracks are shorter than the longitudinal.
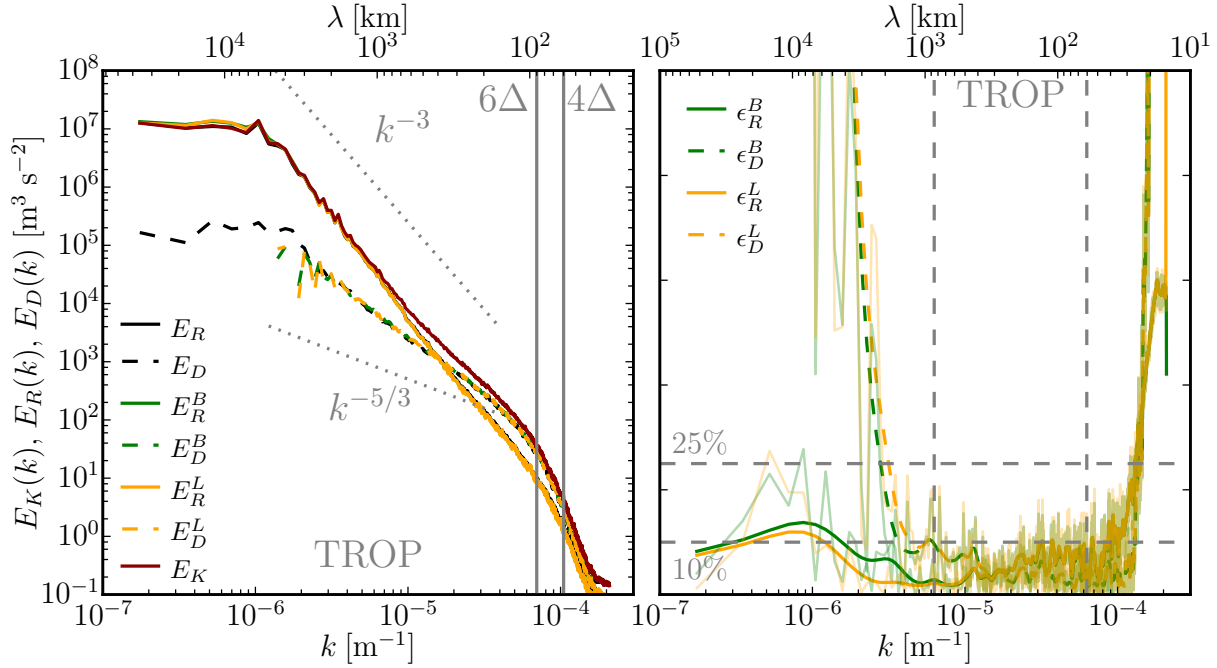
Figure 2.5: Left: as Fig. 2.1 for the C14 setup. Right: as Fig. 2.3 for the C14 setup.

The left panel of Fig. 2.5 displays E_K, E_D and E_R for the full MPAS data, as well as $E_{D,R}^{B,L}$ for the C14 setup. E_D dominates over E_R up to a transition scale at around $400 - 500$km. Beyond that scale, the spectra cross and E_R dominates E_D for larger scales. The scale where E_R and E_D cross also marks the transition of the E_K spectrum from a shallower mesoscale slope to a steeper slope on synoptic scales. This agrees well with the transition scale of $500\,\mathrm{km}$ found by C14.

The errors for $E_{D,R}^{B,L}$ shown in the left panel of Fig. 2.5 as defined in paragraph 2.3.2 are displayed in the right panel of Fig. 2.5. As before, the approaches show matching results and error dependence on along-track wavenumber. $E_D^{B,L}$ compares well to E_D up to a certain scale (here around $2000\,\mathrm{km}$) and becomes very noisy and takes non-physical negative values on the largest scales (see paragraph 2.3.3). The errors of $E_D^{B,L}$ and $E_R^{B,L}$ show, in contrast to the global data, no variation with scale and take small mean mesoscale values of 6.2% ($E_R^{B,L}$) and 3.8% ($E_D^{B,L}$).

The contribution of E_D to E_K is displayed in percentage terms in Fig. 2.6. For MPAS data, the fraction of E_D to E_K gradually drops from roughly 70% at scales near $100\,\mathrm{km}$ to 50% at $400-500\,\mathrm{km}$. The mean ratio E_D/E_R amounts to 1.8 on the mesoscales. The results based on the full MPAS data as well as $E_{D,R}^{B,L}$ reproduce the dominance of E_D over E_R on the mesoscale in the C14 setup. While the MPAS data features $E_D/E_R \sim 1.8$ on the mesoscales, B14 and L15 estimate a value of 2.0 (see Fig. 2.6). Note additionally that due to limitations in the height levels of the available MPAS data, the C14 setup only contains upper tropospheric height levels $8.5, 9.5$ and $10.5\,\mathrm{km}$. Due to the increase of mesoscale E_D with increasing height as reported in the current as well as earlier model studies the dominance of E_D on the mesoscales is expected to be more pronounced if lower stratospheric data were included.
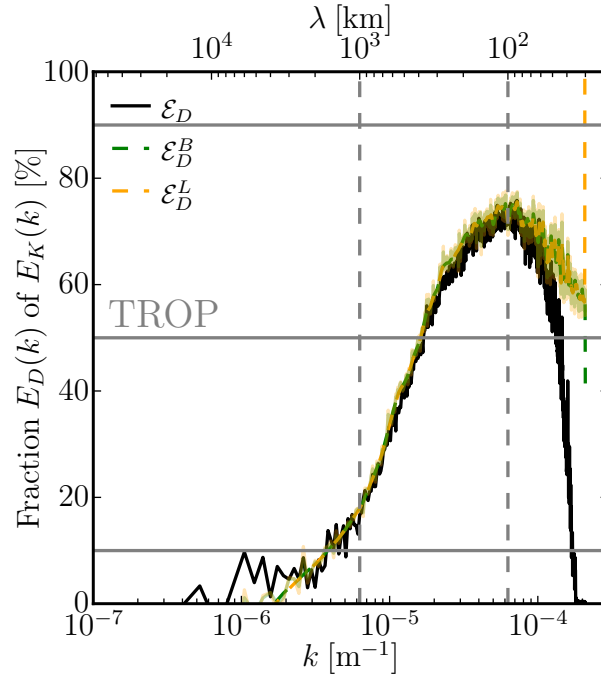
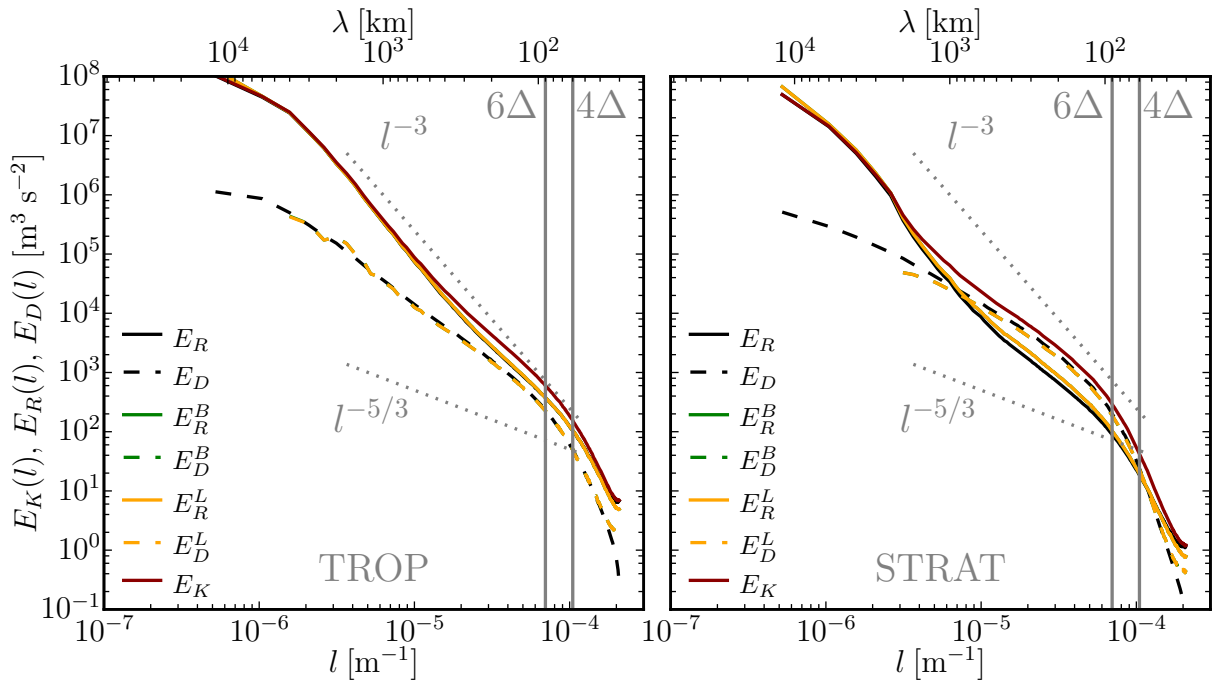**Figure 2.6:** As Fig. 2.2 for the C14 setup.

Figure 2.7: As Fig. 2.1 for the L15 setup for TROP (left) and STRAT (right).

In Fig. 2.7 E_K, E_D and E_R for full MPAS data, as well as $E_{D,R}^{B,L}$ are displayed for the L15 setup and TROP (left) and STRAT (right). The TROP spectra calculated from MPAS data show a dominance of E_R over E_D across the entire scale range with an increasing dominance with increasing scale. E_K again flattens from a steep synoptic scale to a shallower slope on the mesoscale. Contrarily, in STRAT, E_D dominates E_R on scales up to a horizontal scale of around 1000 km where the spectra cross. While E_D has a shallow slope close to a $-5/3$ wavenumber dependence, E_R features a steep approximately -3 dependence on horizontal wavenumber.

The errors according to $E_{D,R}^{B,L}$ shown in Fig. 2.7 are displayed in Fig. 2.8. In TROP, the errors for E_D and E_R do not exceed values of around 10% up to scales of 1000 km with mean values of 3.3% ($E_R^{B,L}$) and 6.7% ($E_D^{B,L}$) on the mesoscales. In STRAT, the errors of the estimate of E_D and E_R take significantly larger values than the previously discussed C14 and global data results. For the L15 setup, B14 and L15 find mean mesoscale ratios E_D/E_R of 0.5 (TROP) and 1.6 (STRAT). The fraction E_D/E_K as calculated from MPAS data as well as for the B14 and L15 estimates and TROP (left) and STRAT (right) are displayed in Fig. 2.9. In TROP, E_D contributes the most to E_K on scales of a few hundreds of kilometers (45%) and drops continuously to a couple of percent on scales around 1000 km. The mean mesoscale ratio E_D/E_R amounts to 0.5. In STRAT (right panel of Fig. 2.9), E_D dominates E_R on the mesoscales. On larger scales the amplitude of E_D decreases rapidly with increasing scale. For the full MPAS data, the mean mesoscale ratio E_D/E_R is 1.8. From Figs. 2.7 and 2.9 it is obvious that the dynamics governing the mesoscales differ significantly in tropospheric and stratospheric heights.
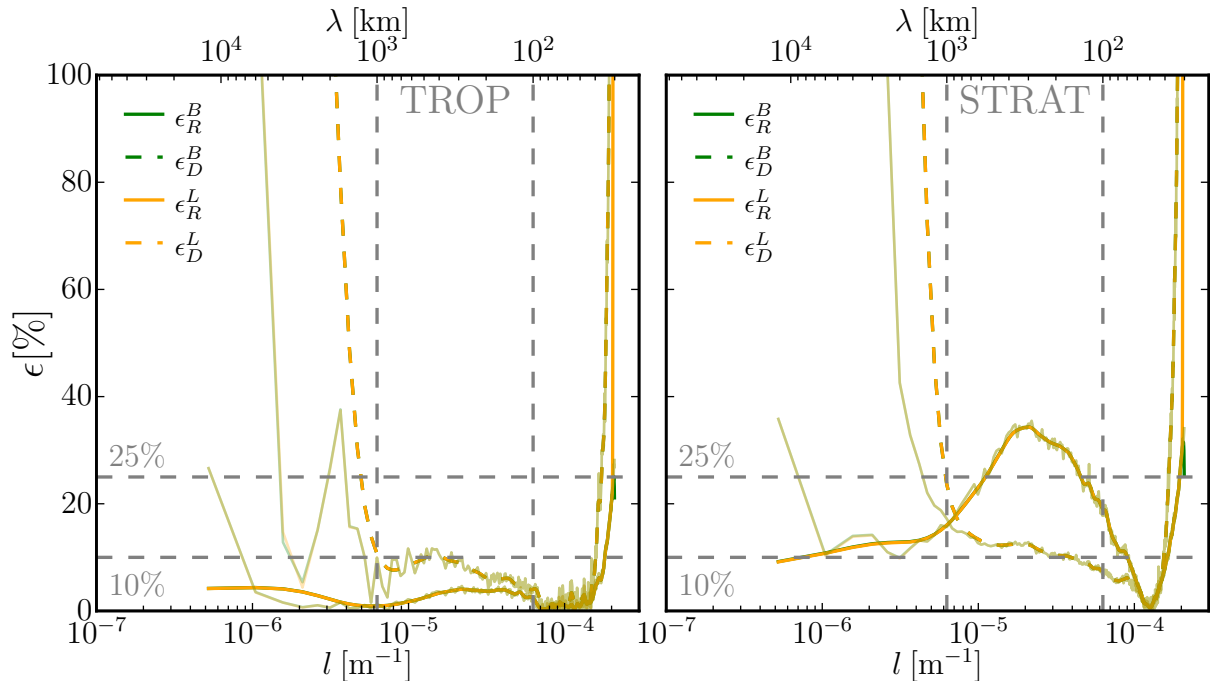
Figure 2.8: As Fig. 2.3 for the L15 setup and TROP (left) and STRAT (right).

In summary, the mesoscale ratio E_D/E_R larger than unity found by C14 for vertically averaged MOZAIC data between 30°N and 60°N is reproduced by the B14 and L15 approaches for a similar subset of MPAS data and the evaluated time span. Using global data averaged over spectra aligned along constant longitudes and latitudes and separating tropospheric and stratospheric heights with the available MPAS data and applying the B14 and L15 method reproduces the L15 result of a dominance of mesoscale E_R over E_D. The errors for B14 and L15 in comparison with MPAS data are too small to account for differences in the dominance of E_D and E_R on the mesoscales. The divergent deductions drawn in C14 and L15 concerning the ratio E_D/E_R on the atmospheric mesoscales do not result from differences or limitations in the B14 and L15 approaches, but rather from the evaluation of different subsets of the MOZAIC data. This finding is furthermore supported by the mesoscale equipartition of E_D and E_R found by L07 for averaged tropospheric and stratospheric global data.
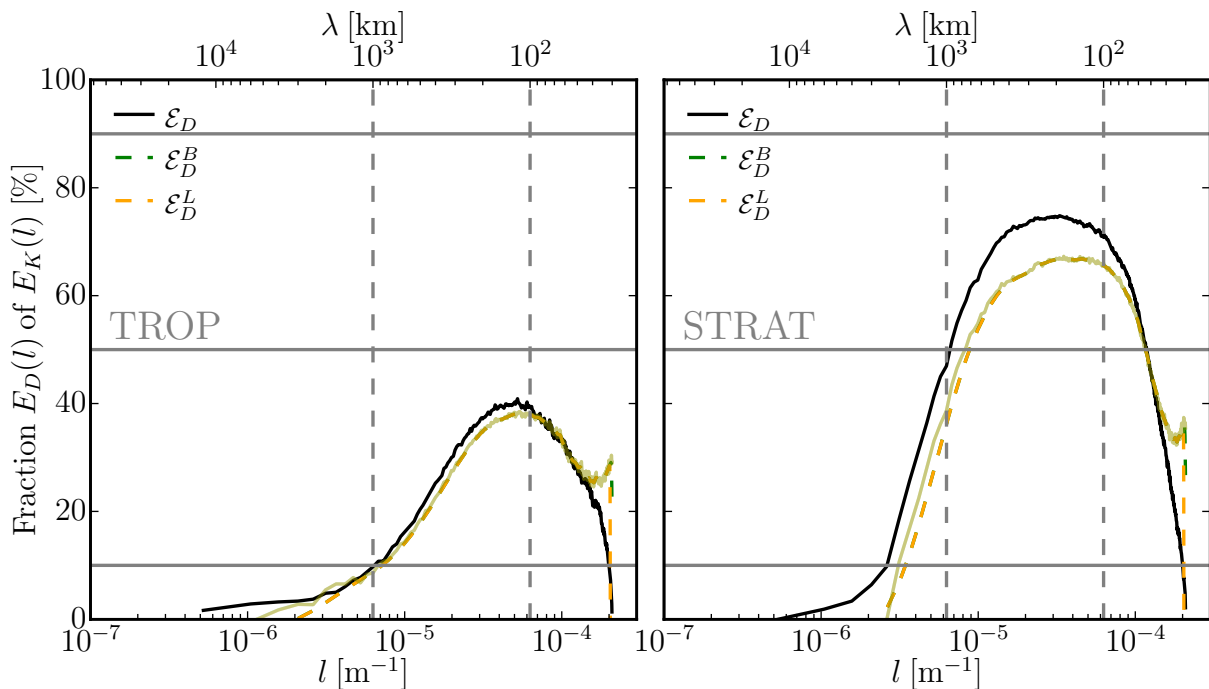
Figure 2.9: As Fig. 2.2 for the L15 setup and TROP (left) and STRAT (right).

2.4.3 Comparison of different latitudinal regions

In the previous paragraphs the consideration of distinct height levels was found to play a major role in the differences arising in C14 and L15. The impact of the evaluated latitudinal region on the spectra and the relevance of rotational and divergent modes is not contained in Bierdel et al. (2016) and will briefly be considered in the following.

In Fig. 2.10, E_K, E_R and E_D calculated from the full MPAS data and the L15 approach are displayed as a function of longitudinal wavenumber k for the TROP height range. While the estimate from the L15 approach is shown for completeness, it is similar to the results from paragraphs 2.3.2 and 2.3.3 and will thus not be discussed explicitly. The associated results from the B14 approach and latitudinal wavenumber spectra are similar and omitted for clarity. As in paragraph 2.3.1, the spectra are taken along longitudinal bands, but not subsequently averaged over the full latitudinal range (60°S and 60°N), but rather over three different subsets: a northern hemispheric band (NHB, latitudes between 20°N and 60°N), a Southern hemispheric band (SHB, latitudes between 60°S and 20°S) and a band centered around the equator (CB, latitudes between 20°S and 20°N). The spectra for all regions are qualitatively similar to the spectra averaged over the global region in paragraph 2.3.1 and general features are discussed therein. Particularly the large-scale part of the NHB and SHB spectra is similar. This resemblance may arise from the presence of atmospheric Rossby waves that are a prominent feature of large-scale dynamics in both latitudinal ranges. There are, however, noteworthy differences that will be briefly discussed in the following.
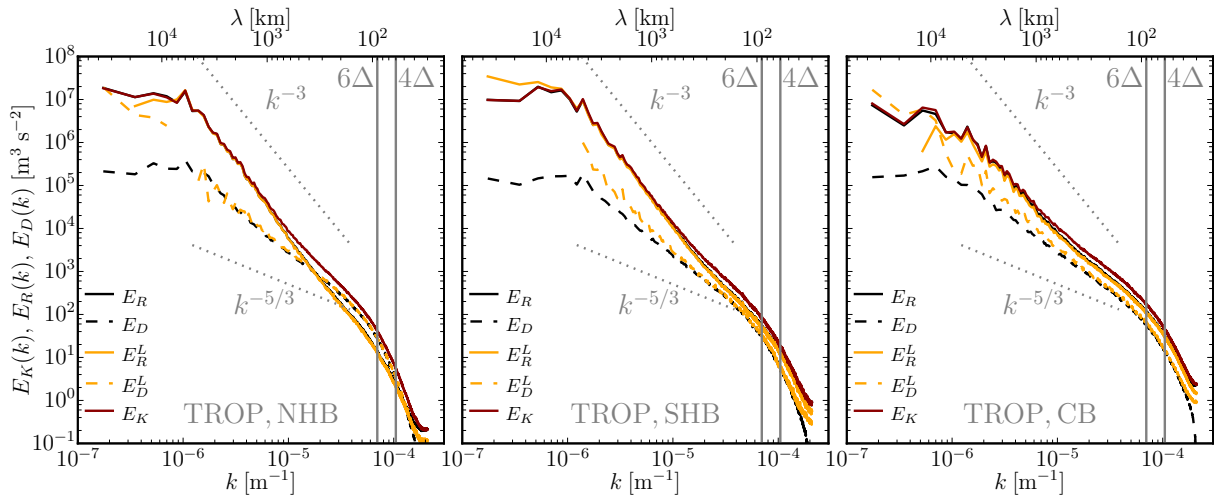
Figure 2.10: As Fig. 2.1 for the L15 method and TROP region only and (from left to right) NHB (Northern Hemispheric Band), SHB (Southern Hemispheric Band) and CB (Central Band). For details see text.

The NHB and SHB spectra differ quantitatively with regard to E_D: in the NHB region E_D dominates E_R up to scales of around 400 km, where the spectra cross and E_R dominates E_D on larger scales. Contrarily, in the SHB region, E_R is dominant on the whole spectral range. The dissimilarity on the small scales in the E_D component might be related to the comparatively higher fraction of NHB that is covered with land and an associated stronger orographically forced gravity wave component than in SHB.

In the equatorial CB region the spectra are generally more different from the NHB and SHB regions: while the large-scale E_K is, as for the other regions, dominated by E_R, the amplitude of both components is lower on the large scales and the spectral slope is shallower. Since the slope of E_D is not significantly altered, E_D has a relatively higher contributions to E_K on

the large scales compared to the other regions. While E_R dominates E_D on the whole scale range, the relative contribution of E_D to E_K in the CB region is not as clearly increasing with decreasing scale as for the other regions. E_R and E_D are rather parallel on a broad scale range (from small scales up to $\mathcal{O}(1000\,\mathrm{km})$) with E_R having twice the amplitude of E_D. Particularly the amplitude of E_K on small-scales is increased compared to the NHB and SHB regions. Generally, the reduced energy and dominance of E_R on large scales in the CB region is understood to arise from a lack of predominant large-scale dynamical mechanisms such as Rossby waves and baroclinic instability that are apparent in mid-latitudinal regions. The shallower slope of the large-scale E_R is understood to result from the absence of a Coriolis force and the associated absence of the enstrophy-cascade in two-dimensional turbulence (see paragraph 1.2.2). However, complex tropical dynamical and thermodynamical processes such as the Hadley cell and organized deep moist convection in the Madden-Julian oscillation may contribute to the horizontal kinetic energy spectrum in the CB region.

In this paragraph E_K and particularly the decomposition into E_R and E_D was shown to feature differences depending on the latitudinal region that the spectra are calculated on. This result furthermore supports the hypothesis that differences in the spectra between the C14 and L15 setups arise mainly from variations in the mesoscale spectra with latitude. For TROP, the mesoscale energy is dominated by E_D in the northern hemisphere and tropics and E_R in the southern hemisphere. This result is in agreement with observational studies that find a dependence of mesoscale spectral variability on the latitudinal range (e.g. Nastrom et al., 1984). Considering transects only in the zonal or meridional direction has little effect (not shown). A detailed dynamical understanding of the presented spectra is beyond the scope of the present study. The results, however, indicate that the dominance of either E_R or E_D might depend on the geographical region and is not globally universal.

2.5   Summary

Two approaches (Bühler et al., 2014; Lindborg, 2015, B14 and L15 respectively) for estimating rotational and divergent kinetic energy spectra from one-dimensional measurements of across- and along-track wind components were evaluated. Both approaches are based on relations between rotational or divergent spectra and velocity along one-dimensional tracks that follow when the flow is homogeneous and isotropic. While B14 requires prior smoothing of the data and the solution of a set of coupled ODEs, L15 is implemented with a simple trapezoidal rule for solving their equations without pre-processing of the data. One-dimensional transects of horizontal velocity fields simulated by the Model for Prediction Across Scales (MPAS) taken along circles of constant latitudes and longitudes serve as an input to the proposed approaches. The resulting spectra of divergent and kinetic energy are then compared to the respective spectra calculated from two-dimensional fields from MPAS, where the decomposition may be done unambiguously.

The two implementations of the decomposition method are very accurate and yield results almost indistinguishable from the correct solution when plotted on the traditional log-log scale. Their errors are largest for the divergent energy on the largest scales and for both energy components near the grid scale. At the mesoscale, errors are 11% and 7% for divergent and

rotational components, respectively, in the troposphere, and 5% and 18% in the stratosphere. The errors on the small-scale end of the spectrum are not further discussed since they are on scales smaller than the effective resolution of the model. The large errors, as well as unphysical negative values of the estimate of the divergent kinetic energy component by both approaches, are also found by L15. While L15 relates those errors to violations of large-scale isotropy, it is found through an examination of purely divergent flows that the cause is most likely a contamination of the divergent-kinetic-energy estimate by small errors in the dominant rotational energy.

Attributing mesoscale errors and their variation with scale to the violation of certain underlying assumptions is not straightforward and beyond the scope of the study presented in this chapter. On the mesoscales, however, the errors of B14 and L15 are small enough that the mesoscale ratio of divergent to rotational kinetic energy (i.e. whether the flow is mainly governed by quasi-two dimensional motions or inertia gravity waves) can be estimated accurately. It is thus concluded that, at least when data are aggregated over large areas, the underlying assumptions of isotropy and homogeneity must be well satisfied.

The application of the B14 and L15 approaches to MOZAIC data by Callies et al. (2014, C14) and L15 led to differing conclusions concerning the mesoscale ratio of divergent to rotational energy components. This issue was assessed by applying the B14 and L15 implementations to various subsets of the MPAS data. Although it was not attempted to reproduce either study in detail, a critical sensitivity of the results on the evaluated latitudinal and height range was found: using upper-tropospheric transects aligned along circles of constant latitude in the range from 30°N to 60°N gave a ratio of divergent to rotational energy of around 2, while averaging over transects along both constant latitudes and constant longitudes, and separated into tropospheric and stratospheric heights, showed an equipartition of rotational and divergent energy in the upper-tropospheric mesoscale.

This result is consistent with the much larger ratio of divergent to rotational energy found by C14 ($E_D/E_R \sim 2$) compared to that found by L15 ($E_D/E_R \sim 1/3$); C14 used long transects of MOZAIC data in the same latitudinal band averaged over upper-tropospheric and lower-stratospheric heights, while L15 considered transects with random orientation and length, and separated data between upper-tropospheric and lower-stratospheric heights. The sensitivity on the latitudinal region has furthermore been assessed by an examination of E_K, E_D and E_R in three different latitudinal regions, which led to different results regarding the dominance of E_D and E_R on the mesoscales. Particularly the found dominance of E_D over E_R in the Northern hemisphere, but not in the Southern hemisphere, is in well agreement with the general observation that atmospheric kinetic energy spectra depend on latitude and if they are taken over ocean or over land (Nastrom et al., 1984; Cho et al., 1999). One reason for the increased mesoscale variability over land, as speculated by Cho et al. (1999), are orographically generated gravity waves. The presented results are not in disagreement with this hypothesis, since land covers a higher percentage of the area in the Northern hemisphere than in the Southern hemisphere.

It is concluded that the results of C14 and L15 differ not because of inherent limitations or differences in the approaches they use but rather from their choices of which subset of the MOZAIC data to examine and the sensitivity of E_D/E_R to the selected latitude and height

region. A more detailed discussion of the results presented in this chapter, limitations of the conducted study as well as suggestions for subsequent research can be found in chapter 5.

In this chapter the relevance of horizontal rotational and divergent modes of motion as signatures of governing mesoscale dynamics have been discussed. Understanding the relative dominance and interplay of these two contributions plays thus an important role in comprehending the mesoscale kinetic energy spectrum (see paragraph 1.2.2). However, this decomposition of the horizontal wind is furthermore relevant to identify the dynamical agent that governs upscale error growth through the mesoscale range: as mesoscale dynamics transition from small- to large scales from significantly divergent to mainly rotational, errors that are initially confined to small atmospheric scales have to transform accordingly when expanding to the large scales. This is the topic of the following chapters 3 and 3.

Chapter 3

Upscale error growth from convection through geostrophic adjustment: An analytical model

3.1 Introduction

The current literature discussing predictability of atmospheric flows and the nature of the underlying scale interactions considers the problem from two main perspectives (see paragraph 1.3.2). One approach is based on early research where the energy transfer between different scales of motions is discussed in terms of local interactions between wavenumber triads in the framework of the two-dimensional vorticity equation (Lorenz, 1969; Leith and Kraichnan, 1972). In these models the predictability time is determined solely by the background kinetic energy spectrum, independent of other details of the underlying dynamical model (Rotunno and Snyder, 2008). However, due to the direct energizing of the mesoscales by processes such as deep moist convection (Waite and Snyder, 2013), the relevance of predictability estimates based on models of homogeneous turbulence to the real atmosphere is not clear (Zhang et al., 2002, 2003; Sun and Zhang, 2016).

An alternative approach introduced in paragraph 1.3.2 is based on results from numerical weather prediction models which suggest that error growth in the atmosphere is an initially localized, highly intermittent phenomenon that expands upscale and plays a significant role in contaminating the larger scale flow at longer forecast lead times (e.g. Hohenegger and Schär, 2007; Zhang et al., 2007; Rodwell et al., 2013; Selz and Craig, 2015b). In particular it has been found that latent heat release associated with deep moist convection is a primary mechanism for small-scale error growth (Zhang et al., 2002, 2003; Tan et al., 2004). The upscale error growth then depends on the underlying dynamics of the respective scale range (such as major instabilities) as opposed to solely the slope of the background spectrum. From an investigation of this second perspective on atmospheric error growth using idealized numerical simulations of a moist baroclinic wave, Zhang et al. (2007) suggest a three-stage conceptual model for atmospheric upscale error growth across a hierarchy of spatial and temporal scales that accounts for the direct forcing of the mesoscales by convection (see schematic illustration in Fig. 1.8). The approximately exponential error growths of the initial and final stages of this

model (stage 1 and 3) appear to be related to convective and baroclinic instabilities acting on small and large scales respectively (Zhang et al., 2007; Selz and Craig, 2015b). The dynamical mechanism dominating an intermediate stage (stage 2), where small-scale unbalanced convective errors transition to larger scale balanced errors, could so far not be identified. However, several indications for the geostrophic adjustment (GA, see paragraph 1.1.1 and schematic illustration in Fig. 1.3) process as dominant for stage 2 of the error growth model have been found in numerical error growth experiments (see Zhang et al., 2007; Selz and Craig, 2015b, Figs. 1.9 and 1.10 in the introduction).

GA is one of the well-known scale-interaction processes in atmospheric fluid dynamics that potentially contribute to the observed shape of the background mesoscale kinetic energy spectrum (for a review see Blumen, 1972; Schubert et al., 1980; Gill, 1982; Vadas and Fritts, 2001; Chagnon and Bannon, 2005a,b). From an error growth perspective, however, the GA process might play a dominant role as being the missing link in the conceptual error growth model between the end of stage 1 and the onset of stage 3, i.e. the complete displacement of individual convective cells and growth of a balanced component of the error within the large-scale baroclinic wave. The slight changes in the amplitude and position of the heating induced by condensation within the convective clouds excites an altered transient wave response as well as secondary circulation through the GA process. The errors that are initially confined on the convective scale thus propagate upscale and enter the balanced larger scale flow. So far, however, the GA mechanism was difficult to extract from numerical simulations of atmospheric flow since a suitable diagnostic has not yet been developed.

In this chapter an analytical formulation for the GA of an imbalance introduced into the atmosphere by the heating of a convective cloud is presented. The derived solution has two major advantages over results published in previous studies. First, it contains a time-dependent formulation of both transients and balanced flow components in one solution as opposed to solving for both parts separately using potential vorticity conservation (Gill, 1982; Schubert et al., 1980). Second, it provides the solution for the buoyancy response of a rotating atmosphere to a δ-function forcing in space and time. This most general solution is the Green's function for the mathematical problem which allows for the simple construction of a solution for arbitrary forcings. From the solution, the temporal and spatial adjustment scales will be identified, and diagnostics will be developed that allow an identification of the GA process in numerical simulations.

The chapter is structured as follows. First, the analytical solution for the GA of an impulsive heating in a rotating atmosphere and the related flow components are derived. Second, the solution and the properties of the different terms as well as the resulting flow are discussed. The spatial and temporal scales of the adjustment process and their dependence on the Coriolis parameter are examined. Third, three diagnostics that can be used to characterize the GA process in numerical simulations are presented. The chapter concludes with a summary.

3.2 The analytical model

A simple analytical model is employed to describe the response of a horizontally unbounded and rotating atmosphere to a buoyancy source in the framework of linear gravity wave theory. A two-dimensional approach will be applied first, where the atmospheric fields are not allowed to vary in the y-direction (slab-symmetry). An associated radially symmetric calculation will be needed later and given in paragraph 3.4.2. The model and analytical solution are based on the work of Bretherton and Smolarkiewicz (1989, hereafter BS89) on convective adjustment, with two main differences. The planetary rotation is included, and the buoyancy source term is formulated as a δ-function in time as opposed to a Heaviside-function.

The equations are linearized around a quiescent background state, and thus all advective terms are neglected. Furthermore the hydrostatic approximation and the Boussinesq approximations are employed. The set of equations, consisting of two horizontal momentum equations, the hydrostatic approximation, the continuity equation and the buoyancy equation, then reads

$$\partial_t u'(x,z,t) - f v'(x,z,t) = -\partial_x \pi'(x,z,t) \tag{3.1}$$
$$\partial_t v'(x,z,t) + f u'(x,z,t) = 0 \tag{3.2}$$
$$-\partial_z \pi'(x,z,t) + b'(x,z,t) = 0 \tag{3.3}$$
$$\partial_x u'(x,z,t) + \partial_z w'(x,z,t) = 0 \tag{3.4}$$
$$\partial_t b'(x,z,t) + N^2 w'(x,z,t) = Q(x,z,t), \tag{3.5}$$

with time t, horizontal distance x and height z. Primes denote the deviations from the quiescent reference atmosphere. The vector $\boldsymbol{v}' = (u', v', w')$ is the three-dimensional perturbation wind. The density is split up into a constant reference value, a background vertical profile, and fluctuations around it, i.e. $\rho = \rho_0 + \tilde{\rho}(z) + \rho'(x,z,t)$. With this the scaled pressure perturbation $\pi' = p'/\rho_0$ and the buoyancy perturbation $b' = -g\rho'/\rho_0$ are defined. The background density profile must decrease with height and is thus responsible for the restoring force in response to vertical displacements. The associated buoyancy frequency or Brunt-Väisälä frequency is given by $N^2 = -g/\rho_0 d_z\tilde{\rho}$. f is the Coriolis parameter which is assumed constant. In the remainder of this chapter primes are dropped for convenience. The buoyancy forcing rate is given by

$$Q(x,z,t) = Q_0 \delta(x)\delta(t) \sin\left(\frac{m\pi}{H_{\text{trop}}} z\right), \tag{3.6}$$

where $\delta(\cdot)$ denotes the Dirac-delta function, Q_0 is the amplitude of the forcing with units $\text{m}^2\,\text{s}^{-2}$ and H_{trop} the tropopause height. The forcing Q is thus located at $x = 0$, and turned on and off instantaneously at time $t = 0$. Its vertical structure follows a sine wave with integer wavenumber $m \in \mathbb{N}$, so that the forcing is assumed to vanish at the ground ($z = 0$) and at the tropopause ($z = H_{\text{trop}}$). The buoyancy forcing rate (3.6) can be converted into a diabatic heating rate, denoted by Q_h with units $\text{J}\,\text{kg}\,\text{s}^{-1}$, using

$$Q_h(x,z,t) = \frac{c_p T_0}{g} Q(x,z,t), \tag{3.7}$$

where c_p is the heat capacity of air at constant pressure and T is the air temperature (Nicholls et al., 1991). The total heating (in Joule) that is associated with the buoyancy forcing (3.6) can thus be calculated by integrating (3.7) over air mass and time. For the deepest vertical

mode ($m = 1$) and approximating temperature and density with their background values ($T = T_0$, $\rho = \rho_0$) the total heating can then be written as

$$Q_{h,tot} = dx \int dy \int dz \int dt \rho_0 Q_h = dy \frac{2H_{\text{trop}}\rho_0 Q_0 c_p T_0}{\pi g}\,. \tag{3.8}$$

Note that for all even vertical modes the column integrated total heating is zero.

3.2.1   The buoyancy solution

An analytical solution for the buoyancy is derived in the following. While the calculation presented in this chapter focuses on the main mathematical steps, a more detailed (and dimensional) version can be found in chapter A of the appendix. To highlight the key scales of the solution, (3.1)-(3.5) will be solved in non-dimensional terms. Each variable in the problem is written as the product of a dimensional and non-dimensional part, i.e.

$$\psi = \Psi\tilde{\psi}\,, \tag{3.9}$$

where $\psi = (t, x, z, u, v, w, b, \pi)$ are the original variables with characteristic magnitudes $\Psi = (\mathcal{T}, \mathcal{L}_h, \mathcal{L}_v, \mathcal{U}, \mathcal{V}, \mathcal{W}, \mathcal{B}, \mathcal{P})$ and $\tilde{\psi}$ are the respective non-dimensional variables. Inserting the scaling (3.9) into (3.1)-(3.5) gives

$$\frac{\mathcal{U}}{\mathcal{T}}\partial_{\tilde{t}}\tilde{u}(\tilde{x}, \tilde{z}, \tilde{t}) - f\mathcal{V}\tilde{v}(\tilde{x}, \tilde{z}, \tilde{t}) = -\frac{\mathcal{P}}{\mathcal{L}_h}\partial_{\tilde{x}}\tilde{\pi}(\tilde{x}, \tilde{z}, \tilde{t}) \tag{3.10}$$

$$\frac{\mathcal{V}}{\mathcal{T}}\partial_{\tilde{t}}\tilde{v}(\tilde{x}, \tilde{z}, \tilde{t}) + f\mathcal{U}\tilde{u}(\tilde{x}, \tilde{z}, \tilde{t}) = 0 \tag{3.11}$$

$$-\frac{\mathcal{P}}{\mathcal{L}_v}\partial_{\tilde{z}}\tilde{\pi}(\tilde{x}, \tilde{z}, \tilde{t}) + \mathcal{B}\tilde{b}(\tilde{x}, \tilde{z}, \tilde{t}) = 0 \tag{3.12}$$

$$\frac{\mathcal{U}}{\mathcal{L}_h}\partial_{\tilde{x}}\tilde{u}(\tilde{x}, \tilde{z}, \tilde{t}) + \frac{\mathcal{W}}{\mathcal{L}_h}\partial_{\tilde{z}}\tilde{w}(\tilde{x}, \tilde{z}, \tilde{t}) = 0 \tag{3.13}$$

$$\frac{\mathcal{B}}{\mathcal{T}}\partial_{\tilde{t}}\tilde{b}(\tilde{x}, \tilde{z}, \tilde{t}) + N^2\mathcal{W}\tilde{w}(\tilde{x}, \tilde{z}, \tilde{t}) = \mathcal{Q}\tilde{Q}(\tilde{x}, \tilde{z}, \tilde{t})\,, \tag{3.14}$$

where the forcing reads

$$\mathcal{Q}\tilde{Q}(\tilde{x}, \tilde{z}, \tilde{t}) = \frac{Q_0}{\mathcal{L}_h\mathcal{T}}\delta(\tilde{x})\delta(\tilde{t})\sin\left(\frac{m\pi\mathcal{L}_v}{H_{\text{trop}}}\tilde{z}\right)$$

Since the buoyancy forcing (3.6) spans the depth of the troposphere, the height scale is set as

$$\mathcal{L}_v \sim \frac{H_{\text{trop}}}{\pi} := H\,, \tag{3.15}$$

where H_{trop} is the tropopause height and the factor π^{-1} is included for convenience. The system of equations (3.10)-(3.14) has four externally imposed parameters, namely the Brunt-Väisälä frequency N, the height scale H, the forcing amplitude Q_0 and the rotation rate f. The remaining characteristic magnitudes in Ψ will be expressed in terms of these parameters.

The scales for the temporal and horizontal spatial coordinates, $\mathcal{T}$ and $\mathcal{L}_h$, will be considered first. Assuming that $\mathcal{U} \sim \mathcal{V}$, the second momentum equation (3.11) implies that time scales with the inverse of the inertial frequency, i.e.

$$\mathcal{T} \sim f^{-1}. \tag{3.16}$$

An appropriate horizontal length scale can be derived as follows. With the vertical scale given by (3.15), the gravity wave speed for vertical mode m is given by

$$c_m = \frac{NH}{m}. \tag{3.17}$$

The gravest ($m = 1$) gravity wave mode excited by the heating has the greatest propagation speed NH. The horizontal length scale considered here is the distance this fastest gravity wave mode travels in one inertial period $\mathcal{T}$ and reads

$$\mathcal{L}_h \sim \frac{NH}{f} = R_d. \tag{3.18}$$

This horizontal length scale can be identified as the (first baroclinic) Rossby radius of deformation R_d. The physical role of this length scale in the solution will be discussed in paragraph 3.3.2. The scaling of the remaining parameters, $\mathcal{U}, \mathcal{V}, \mathcal{W}, \mathcal{B}$ and $\mathcal{P}$, can easily be obtained from (3.10) and (3.12)-(3.14) and are given in table 3.1. Since all variables of (3.10)-(3.14) are expressed in terms of the external parameters N, f, Q_0 and H the scaling of the underlying equations is completed.

Table 3.1: Scaling of all Ψ in (3.10)-(3.14) in terms of N, f, Q_0 and H.

$\mathcal{T}$	$\mathcal{L}_v$	$\mathcal{L}_h$	$\mathcal{U} \sim \mathcal{V}$	$\mathcal{W}$	$\mathcal{B}$	$\mathcal{P}$
f^{-1}	H	$\frac{NH}{f}$	$\frac{Q_0 f}{N^2 H}$	$\frac{Q_0 f^2}{N^3 H}$	$\frac{Q_0 f}{NH}$	$\frac{Q_0 f}{N}$

The scaling given in table 3.1 is inserted in (3.10)-(3.14), which can be combined to yield a partial differential equation for the buoyancy:

$$(\partial_{\tilde{t}}^3 \partial_{\tilde{z}}^2 + \partial_{\tilde{t}} \partial_{\tilde{z}}^2 + \partial_{\tilde{t}} \partial_{\tilde{x}}^2) \, \tilde{b}_m(\tilde{x}, \tilde{z}, \tilde{t})$$
$$= (\partial_{\tilde{t}}^2 \partial_{\tilde{z}}^2 + \partial_{\tilde{z}}^2) \, \delta(\tilde{x}) \delta(\tilde{t}) \sin(m\tilde{z}), \tag{3.19}$$

where the subscript m denotes the buoyancy solution for the vertical mode with wavenumber m. Separating out the $\tilde{z}$-dependence gives an equation for the amplitude of the buoyancy $\tilde{B}_m(\tilde{x}, \tilde{t})$ with $\tilde{b}_m(\tilde{x}, \tilde{z}, \tilde{t}) = \tilde{B}_m(\tilde{x}, \tilde{t}) \sin(m\tilde{z})$

$$(\partial_{\tilde{t}}^3 + \partial_{\tilde{t}} - m^{-2} \partial_{\tilde{t}} \partial_{\tilde{x}}^2) \, \tilde{B}_m(\tilde{x}, \tilde{t}) = (\partial_{\tilde{t}}^2 + 1) \, \delta(\tilde{x}) \delta(\tilde{t}). \tag{3.20}$$

As in BS89 the solution proceeds by applying the Laplace transform

$$\mathcal{L}\{f(t)\} = F(s) = \int_{0^-}^{\infty} f(t) \exp(-st) \, dt, \quad s \in \mathbb{C} \tag{3.21}$$

to (3.20). The Laplace transform of $n-$th order temporal derivatives reads (Abramowitz and Stegun, 1964, formula 29.2.5)

$$\mathcal{L}\{\partial_t^{(n)} f(t)\} = s^n \mathcal{L}\{f(t)\} - \sum_{k=1}^{n} s^{k-1} \left. \partial_t^{n-k} f(t)\right|_{0^-} . \tag{3.22}$$

Using these relations, the equation for the Laplace transform of the buoyancy $\tilde{\beta}_m(\tilde{x}, \tilde{s}) = \mathcal{L}\{\tilde{B}_m(\tilde{x}, \tilde{t})\}$ becomes

$$\partial_{\tilde{x}}^2 \tilde{\beta}_m(\tilde{x}, \tilde{s}) - m^2(\tilde{s}^2 + 1)\tilde{\beta}_m(\tilde{x}, \tilde{s}) = -m^2(\tilde{s} + \tilde{s}^{-1})\delta(\tilde{x}) . \tag{3.23}$$

In order to evaluate $\tilde{B}_m(\tilde{s})$, (3.23) is formally treated as a homogeneous equation and the inhomogeneity as a boundary condition. The solution to the homogeneous equation that is symmetric in $\tilde{x}$ is

$$\tilde{\beta}_m(\tilde{x}, \tilde{s}) = \tilde{B}_m(\tilde{s}) \exp\left(-m\sqrt{\tilde{s}^2 + 1}\, |\tilde{x}|\right) \tag{3.24}$$

To find the boundary condition corresponding to the inhomogeneous term, (3.23) is integrated from $-\tilde{x}$ to $\tilde{x}$ and then the limit $\tilde{x} \to 0$ is taken. With $\tilde{\beta}_m(\tilde{x}, \tilde{s})$ bounded, it follows that

$$\lim_{\tilde{x} \to 0} [\partial_{\tilde{x}} \tilde{\beta}_m(\tilde{x}', \tilde{s})]_{\tilde{x}'=-\tilde{x}}^{\tilde{x}'=\tilde{x}} = -m^2(\tilde{s} + \tilde{s}^{-1}) . \tag{3.25}$$

The left hand side of (3.25) can be directly evaluated using the homogeneous solution (3.24). Noting that

$$\partial_{\tilde{x}} \tilde{\beta}_m(\tilde{x}, \tilde{s}) = -m\tilde{B}_m(\tilde{s})\sqrt{\tilde{s}^2 + 1} \exp(-m\sqrt{\tilde{s}^2 + 1}|\tilde{x}|) sgn(\tilde{x}) ,$$

where $sgn(\cdot)$ is the sign function, it follows that

$$\lim_{\tilde{x} \to 0} [\partial_{\tilde{x}} \tilde{\beta}_m(\tilde{x}', \tilde{s})]_{\tilde{x}'=-\tilde{x}}^{\tilde{x}'=\tilde{x}} = -2m\tilde{B}_m(\tilde{s})\sqrt{\tilde{s}^2 + 1}$$

and with (3.25) the amplitude reads

$$\tilde{B}_m(\tilde{s}) = \frac{m}{2} \frac{(\tilde{s} + \tilde{s}^{-1})}{\sqrt{\tilde{s}^2 + 1}} . \tag{3.26}$$

The full solution for the Laplace transform of the buoyancy results from (3.24) and (3.26) as

$$\tilde{\beta}_m(\tilde{x}, \tilde{s}) = \frac{m}{2} \left\{ \tilde{s}\tilde{\gamma}_m(\tilde{x}, \tilde{s}) + \tilde{s}^{-1}\tilde{\gamma}_m(\tilde{x}, \tilde{s}) \right\} \tag{3.27}$$

$$\text{with}\ \ \tilde{\gamma}_m(\tilde{x}, \tilde{s}) = \frac{1}{\sqrt{\tilde{s}^2 + 1}} \exp\left(-m\sqrt{\tilde{s}^2 + 1}\, |\tilde{x}|\right) . \tag{3.28}$$

Using the linearity property of the Laplace transform and the differentiation and integration rules involving Laplace transforms (Abramowitz and Stegun, 1964, formulas 29.2.3, 29.2.4, 29.2.6 and 29.3.92) it can be shown that the inverse transform $\tilde{B}_m(\tilde{x}, \tilde{t}) = \mathcal{L}^{-1}\left\{\tilde{\beta}_m(\tilde{x}, \tilde{s})\right\}$ is

$$\tilde{B}_m(\tilde{x}, \tilde{t}) = \frac{m}{2} \left\{ \partial_{\tilde{t}} \tilde{G}_m(\tilde{x}, \tilde{t}) + \int_0^{\tilde{t}} \tilde{G}_m(\tilde{x}, \tilde{t}') \, d\tilde{t}' \right\} ,$$

with

$$\tilde{G}_m(\tilde{x}, \tilde{t}) = \mathcal{L}^{-1}\{\tilde{\gamma}_m(\tilde{x}, \tilde{s})\}$$

$$= \mathcal{J}_0\left(\sqrt{\tilde{t}^2 - (m\tilde{x})^2}\right) \mathsf{H}(\tilde{t} - m|\tilde{x}|), \tag{3.29}$$

where $\mathcal{J}_i(\cdot)$ is the Bessel function of first kind and integer order i and $\mathsf{H}(\cdot)$ denotes the unit step function. Finally, the solution for the buoyancy field, $\tilde{b}_m(\tilde{x}, \tilde{z}, \tilde{t}) = \tilde{B}_m(\tilde{x}, \tilde{t})\sin(m\tilde{z})$, reads

$$\tilde{b}_m(\tilde{x}, \tilde{z}, \tilde{t}) = \frac{m}{2}\left\{ \mathcal{J}_0(\tilde{\tau}_r)\delta(\tilde{t}_r) - \frac{\tilde{t}}{\tilde{\tau}_r}\mathcal{J}_1(\tilde{\tau}_r)\mathsf{H}(\tilde{t}_r) \right.$$

$$\left. + \int_0^{\tilde{t}} \mathcal{J}_0(\tilde{\tau}_r')\mathsf{H}(\tilde{t}_r')\, d\tilde{t}' \right\}\sin(m\tilde{z}) \tag{3.30}$$

$$= \tilde{b}_m^{\mathrm{dt}}(\tilde{x}, \tilde{z}, \tilde{t}) + \tilde{b}_m^{\mathrm{igw}}(\tilde{x}, \tilde{z}, \tilde{t}) + \tilde{b}_m^{\mathrm{b}}(\tilde{x}, \tilde{z}, \tilde{t}),$$

where

$$\tilde{t}_r = \tilde{t} - m|\tilde{x}|$$

$$\tilde{\tau}_r = \sqrt{\tilde{t}^2 - (m\tilde{x})^2}$$

are non-dimensional retarded times. The subscript of the b-terms stands for the m-th vertical mode and the superscripts stand for the three summands of the buoyancy solution (dt= discontinuous transition, igw= inertia-gravity wave and b=balance). It can be shown that (3.30) reformulated in dimensional terms reduces to the solution presented by BS89 for $f = 0$ for their choice of the temporal forcing (i.e. Heaviside function), as expected. The analytical solution allows the unbalanced and balanced contributions to the buoyancy to be considered separately. From the initial set of equations (3.10)-(3.14) and (3.30) all other flow components can be derived from the buoyancy solution. In particular, expressions for the vertical velocity and the (transient) geostrophic wind can be derived from (3.14) and (3.30) as

$$\tilde{w}_m(\tilde{x}, \tilde{z}, \tilde{t}) = \left\{ \delta(\tilde{x})\delta(\tilde{t}) - \partial_{\tilde{t}}\tilde{b}_m(\tilde{x}, \tilde{t}) \right\}\sin(m\tilde{z}) \tag{3.31}$$

$$\tilde{v}_m^g(\tilde{x}, \tilde{z}, \tilde{t}) = \partial_{\tilde{x}}\tilde{b}_m(\tilde{x}, \tilde{t})\left\{ \frac{1 - \cos(m\tilde{z})}{m} \right\}, \tag{3.32}$$

where $\tilde{b}_m(\tilde{x}, \tilde{t})$ denotes the solution given in (3.30) without the sinusoidal vertical dependence, i.e. $\tilde{b}_m(\tilde{x}, \tilde{z}, \tilde{t}) = \tilde{b}_m(\tilde{x}, \tilde{t})\sin(m\tilde{z})$. The divergence and vorticity are derived analogously from the continuity and $\tilde{v}$-momentum equations (3.13) and (3.11) as

$$\partial_{\tilde{x}}\tilde{u}(\tilde{x}, \tilde{z}, \tilde{t}) = -\left\{ \delta(\tilde{x})\delta(\tilde{t}) - \partial_{\tilde{t}}\tilde{b}_m(\tilde{x}, \tilde{t}) \right\}m\cos(m\tilde{z}) \tag{3.33}$$

$$\partial_{\tilde{x}}\tilde{v}(\tilde{x}, \tilde{z}, \tilde{t}) = \left\{ \delta(\tilde{t}) - \left[\tilde{b}_m(\tilde{x}, \tilde{t}')\right]_{\tilde{t}'=0}^{\tilde{t}'=\tilde{t}} \right\}m\cos(m\tilde{z}). \tag{3.34}$$

The results from (3.31)-(3.34) will be employed later. Note that analytical expressions for the temporal and spatial derivatives in (3.31)-(3.34) can be obtained but are not written explicitly in the interest of clarity.

Two advantages of the presented solution (3.30) over results published in foregoing studies, as already mentioned in the introduction, become apparent. First, it contains all transients and balanced flow components in one solution and in particular the temporal evolution of the geostrophically balanced flow can be directly computed. This evolution is described only implicitly when using the mathematically more straightforward approach of solving for the final (infinite time) balanced flow separately using potential vorticity conservation (Gill, 1982; Schubert et al., 1980). Second, it provides the spatial and temporal Green's function solution of the buoyancy response of a rotating atmosphere to an imposed heating. For a general buoyancy source, varying in space and time,

$$\tilde{Q}(\tilde{x}, \tilde{z}, \tilde{t}) = \sum_m \tilde{Q}_m(\tilde{x}, \tilde{t}) \, \sin(m\tilde{z}) \,, \tag{3.35}$$

the corresponding buoyancy solution can be constructed by linear superposition

$$\tilde{b}(\tilde{x}, \tilde{z}, \tilde{t}) = \sum_m \int\limits_{-\infty}^{\infty} \int\limits_{0}^{\infty} \tilde{b}_m(\tilde{x}', \tilde{z}, \tilde{t}') \tilde{Q}_m(\tilde{x} - \tilde{x}', \tilde{t} - \tilde{t}') \, d\tilde{x}' \, d\tilde{t}' \,. \tag{3.36}$$

This property is useful when applying the solution to the real atmosphere, since the time and length scales of the forcing have a major impact on the nature of the flow response (Chagnon and Bannon, 2001, 2005a,b; Vadas and Fritts, 2001). This issue will be discussed further in paragraph 3.3.2.

3.3   Results

In this section basic properties of the solution are described. First, the structure and physical interpretation of the flow is given, noting the differences to the nonrotating solution of BS89. Second, the relevant spatial and temporal scales of the adjustment process and their dependence on f are identified. Finally, diagnostics are introduced that allow for a quantitative assessment of the GA process in numerical simulations.

3.3.1   Solution structure

In the following the buoyancy solution for a pulse forcing given in (3.30) will be examined in detail. As pointed out in section 3.2, the separability of the underlying equations allows the solution to be represented as a sum of vertical modes. The typical vertical profile of latent heating within a region with deep moist convection is positive throughout the column, peaks in the mid-troposphere and therefore projects most strongly onto a half-wave spanning the whole troposphere in the vertical (Nicholls et al., 1991). Higher vertical modes will also be excited but the gravest tropospheric mode has the greatest speed and amplitude and dominates the adjustment of the surrounding atmosphere to the imbalance (Mapes, 1993).

Thus, while solving the considered problem for a set of vertical modes does not add significant mathematical complexity, the following discussion will focus on the dominant $m = 1$ mode (half a sine wave between $z = 0$ and $z = H_{\text{trop}}$).

For a quantitative physical description of the resulting flow field, it will be useful to plot the solution in dimensional variables. The Brunt-Väisälä frequency is taken to be $N = 0.01\,\text{s}^{-1}$ and the height scale $H_{\text{trop}}\pi^{-1}$ with $H_{\text{trop}} = 10\,\text{km}$. The gravity wave speed of the gravest mode is then $c_1 = NH = 31.8\,\text{ms}^{-1}$. The other parameters are given by: total heating is set to $Q_0 = 7200\,\text{Jkg}^{-1}$ which equals a heating rate of $2\,\text{J(kg s)}^{-1}$ assumed by Nicholls et al. (1991) integrated over $1\,\text{h}$ approximate lifetime of a cloud. The Coriolis parameter is set to $f = f_0 = 1.03 \cdot 10^{-4}\,\text{s}^{-1}$.

Figure 3.1 displays the full buoyancy solution in two ways: in Fig. 3.1a a Hovmöller diagram is shown and in Fig. 3.1b the $x-$dependence of the solution is displayed for four different times. The solution has several characteristics associated with the three terms b_1^j in (3.30): the black line in Fig. 3.1a and the vertical line in Fig. 3.1b indicate a sharp front that is excited by the pulse forcing and spreads out symmetrically from the source at speed c_1 (b_1^{dt}). This fast mode propagates the disturbance with a constant amplitude to the unperturbed atmosphere, which is displayed as white areas in Fig. 3.1a (i.e. $|x| > c_1 t$) and is also apparent in the non-rotating solution of BS89.
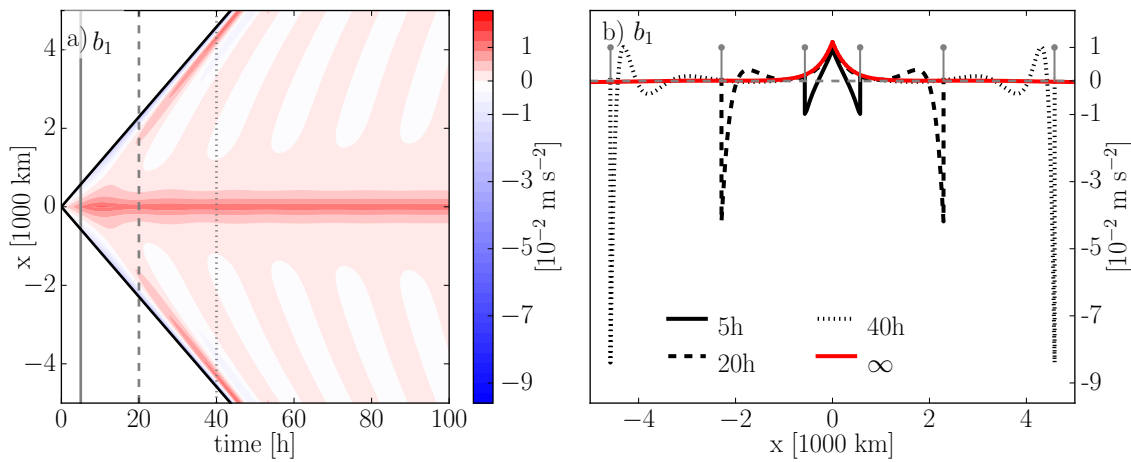
Figure 3.1: Full buoyancy solution b_1 at $z = H_{\text{trop}}/2$ a) as a function of distance from the source and time (Hovmöller diagram) and b) spatial dependence of solution for 5h, 20h, 40h and infinity. Gray solid, dashed and dotted lines in a) are times of cross-sections displayed in b) (see (3.30)). Vertical gray lines in b) demark the position of the discrete front at different times.

In Fig. 3.1 a wake of negative buoyancy that is narrowing and increasing in amplitude with time is trailed behind the wave front. The responsible term (b_1^{igw}) is shown in Fig. 3.2a and originates from a dispersive spectrum of inertia-gravity waves. The short-wavelength gravity wave modes propagate rapidly away from the source and separate from the longer modes with smaller phase speed, leading to a narrowing of the front. Close to the source, only the slowly propagating modes remain, and the frequency rapidly approaches the inertial frequency f.
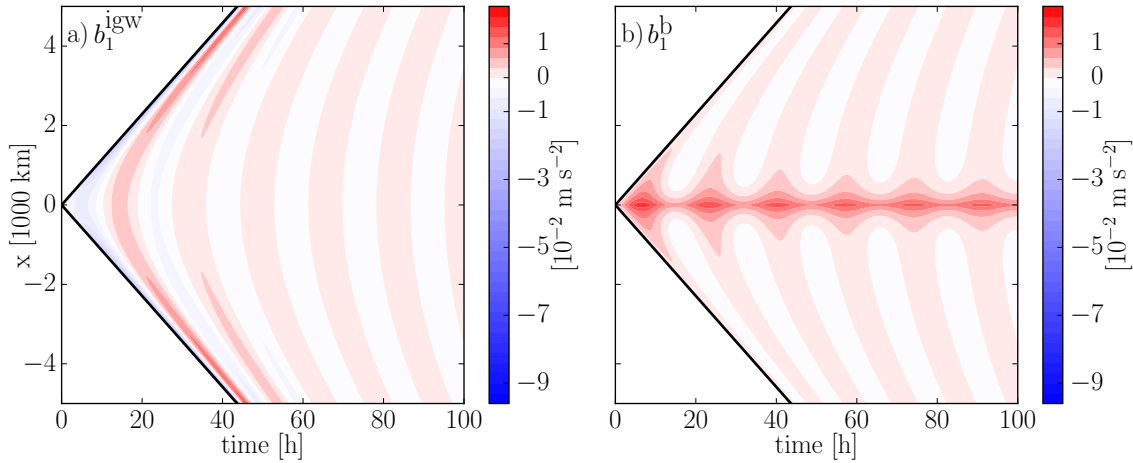
Figure 3.2: As Fig. 3.1a for a) b_1^{igw} and b) b_1^{b} at $z = H_{\text{trop}}/2$ (see (3.30)).

This dispersion process is discussed by Gill (1982) for an initial height perturbation in the shallow water equations, where it is shown that the amplitude of the inertial oscillation near the source location decays proportional to $t^{1/2}$. These oscillations are also apparent in Fig. 3.2b which shows the third term (b_1^{b}) in the buoyancy solution. This term is associated with the balanced flow that remains after the transient waves have left a particular part of the domain. The oscillations are superimposed on a persistent perturbation confined close to the source location. This part of the flow is of particular interest in this dissertation and will be examined in more detail in the following paragraph.
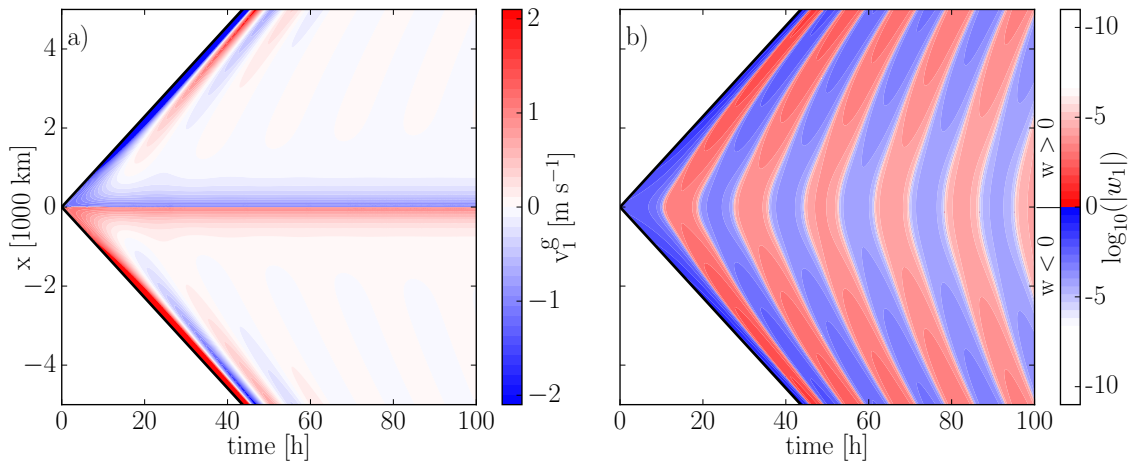
Figure 3.3: a) Geostrophic wind and b) $\log_{10}$ of the absolute value of the vertical velocity w_1 at $z = H_{\text{trop}}/2$. In b) blue and red colors indicate negative and positive values respectively. Note that the vertical velocity does not exceed a value of $1\,\text{ms}^{-1}$.

Physically, the following picture emerges (see also paragraph 1.1.1 and schematic in Fig. 1.3). The impulsive heat forcing at $t = 0$ generates a positive buoyancy anomaly that forces an updraft ($w_1 > 0$) in the center of the domain. The forcing excites gravity waves that propagate

horizontally away from the location of the heating to infinity. Furthermore the upward mass flux drives a divergent flow in the upper half of the domain and a convergent flow in the lower half of the domain. The Coriolis force acting on the divergent wind leads to the spin-up of a balanced (rotational) geostrophic wind (Fig. 3.3a) around the location of the initial imbalance. This rotational wind is anticyclonic in the upper half of the domain and cyclonic in the lower half. Note that due to the relatively strong pressure gradients at the front, the diagnosed geostrophic wind also has a high amplitude at the transient gravity wave front. As the vertical velocity in the center of the domain slowly decays to zero in the limit $t \to \infty$ (Fig. 3.3b) and the transient wave components have propagated out, the final state arising from the impulsive heating is a geostrophically balanced vortex centered around the location of the forcing.

3.3.2 Spatial and temporal scales of the geostrophic adjustment process

In the following, the characteristic spatial and temporal scales of the GA process and their dependence on the Coriolis parameter f are examined.

Spatial adjustment scale

In the long temporal limit the transient waves pass any location, i.e. the terms $\tilde{b}_m^{\mathrm{dt}}$ and $\tilde{b}_m^{\mathrm{igw}}$ pointwise converge to zero. This means that the buoyancy solution point-wise converges to $\tilde{b}_m^{\mathrm{b}}$ ($\tilde{t} \to \infty$). A change in variables with the known results of the zero-order Hankel transform shows that

$$\lim_{\tilde{t} \to \infty} \tilde{b}_m(\tilde{x}, \tilde{z}, \tilde{t}) = \frac{m}{2} \exp(-|\tilde{x}|) \sin(m\tilde{z}) \,. \tag{3.37}$$

This limit agrees with solutions found for the balanced final equilibrium separately (see Gill, 1982). The final, balanced response to the buoyancy perturbation decays exponentially away from the perturbation location with a length scale of unity in the nondimensional equation, corresponding to the Rossby radius of deformation R_d in dimensional terms (see (3.18)). Thus while the solution initially behaves similarly to the nonrotating limit, where an imposed heating generates a buoyancy perturbation that spreads outwards indefinitely (BS89), at later times rotation effects become evident and part of the response remains confined to a finite region with R_d being the characteristic length scale of GA

$$x_{GA} \approx R_d \,. \tag{3.38}$$

In the large panel of Fig. 3.4 the buoyancy solution $b_1(x, z, t)$ is displayed as a function of distance from the source for three exemplary rotation rates $f = f_0, 1.5f_0$ and $2f_0$ and at large times ($t \to \infty$). Dimensional units are employed to visualize quantitative differences arising from the choice of different f-values, where Q_0, N^2 and H are fixed at the values chosen in 3.3.1. Note that the sharp initial discontinuity associated with b_1^{dt} has propagated out of the domain by this time. It can be seen that much of the perturbation is confined to a limited region around the location of the initial forcing. The inset in Fig. 3.4 shows the nondimensional form of the $\tilde{t} \to \infty$ result given in (3.37), where the amplitude is scaled with

$\mathcal{B}$. For the chosen scaling of amplitude, time and horizontal distance with $\mathcal{B}$, f^{-1} and R_d respectively, the balanced flow takes this universal form.

The solution for a buoyancy forcing with arbitrary spatial structure can be obtained as the convolution of the Green's function solution presented here with the forcing function. For the final balanced flow component $(b_m^b(x, z, t \to \infty))$, the time integral commutes with the spatial averaging of the convolution (Chagnon and Bannon, 2001). As a result the spatial structure of the final balanced flow is given by the spatial structure of the time-integrated buoyancy source, smoothed over a scale equal to R_d by convolution with the infinite-time Green's function solution (3.37). Since the size of the buoyancy source associated with a convective cloud $(\mathcal{O}(1)\mathrm{km})$ is typically small compared to the adjustment scale (i.e. R_d, $\mathcal{O}(1000)\mathrm{km}$), the final balanced state it induces will only differ significantly from that shown in Fig. 3.4 near the sharp peak at $x = 0$, which will be smoothed over a distance given by the size of the cloud. The effects of the spatial scale of the forcing on the transient response are more complex (Chagnon and Bannon, 2005a,b), but will turn out to be less important those of the temporal variation, as discussed below.
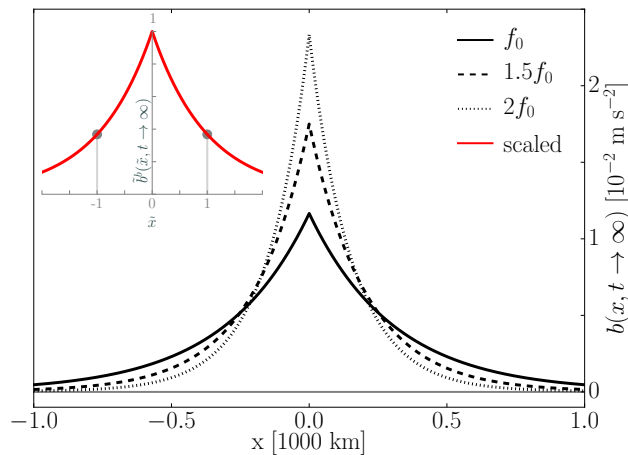

Figure 3.4: Long-time limit of the spatial dependence of buoyancy at $z = H_{\mathrm{trop}}/2$ for three different Coriolis parameters $f_0, 1.5f_0$ and $2f_0$. Small inset: Same as in large panel but for the non-dimensional quantities, see (3.37). The rescaling removes any dependence.

Temporal adjustment scale

While the spatial adjustment scale was found in the previous paragraph by considering the limit $\tilde{t} \to \infty$, the temporal adjustment scale can be isolated by evaluating the balanced term of the buoyancy solution b_m^{b} at $\tilde{x} = 0$. Here the time integral can be solved analytically to yield

$$
\lim_{\tilde{x} \to 0} \tilde{b}_m^b(\tilde{x}, \tilde{z}, \tilde{t}) =
$$

$$
\frac{m}{2} \left\{ \mathcal{J}_0(\tilde{t})\delta(\tilde{t}) - \mathcal{J}_1(\tilde{t})\mathsf{H}(\tilde{t}) \right.
$$

$$
\left. + \frac{\tilde{t}}{2} \left(\pi \mathcal{J}_1(\tilde{t})\mathcal{H}_0^S(\tilde{t}) + \mathcal{J}_0(\tilde{t}) \left[2 - \pi \mathcal{H}_1^S(\tilde{t}) \right] \right) \right\} \sin(m\tilde{z}), \tag{3.39}
$$

where $\mathcal{H}_j^S$ is the Struve-function of order j.
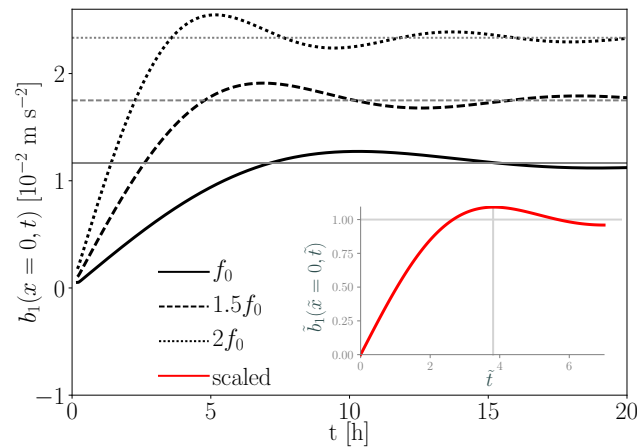
Figure 3.5: Temporal evolution of buoyancy at the position of the source $x = 0$ ($z = H_{\mathrm{trop}}/2$) for three different Coriolis parameters $f_0, 1.5f_0$ and $2f_0$. Horizontal gray lines are values of the buoyancy are associated values of the buoyancy for $t \to \infty$. Small inset: $\tilde{x} \to 0$ result according to (3.39) for amplitude and time scaled with $\mathcal{B}$ and f_0^{-1} respectively.

The three black lines in Fig. 3.5 show the temporal evolution of the buoyancy at the origin $x = 0$ for the three rotation rates. The $t \to \infty$ limit is indicated by the associated horizontal lines and reflects the dependence of the buoyancy amplitude on f already described. In addition it can be seen that the timescale for the buoyancy to reach the final level is longer for smaller f. As a quantitative estimate for the adjustment timescale the time of the first maximum of (3.39) can be used, which results in

$$
t_{GA} \approx 3.81 f^{-1}. \tag{3.40}
$$

The adjustment time scale t_{GA} thus amounts to around $10\,\mathrm{h}$ (for mid-latitudinal f-values) which is in good agreement with the simple dimensional argument in SC15. The universality of the temporal evolution of the solution is illustrated when time, space and amplitude are

nondimensionalized with f^{-1}, R_d and $\mathcal{B}$ respectively as in (3.39). The result is displayed in the inset in Fig. 3.5 for $\tilde{x} = 0$ where the horizontal gray line is the asymptote as before.

As discussed at the end of paragraph 3.3.2, the final balanced circulation depends only on the time-integral of the forcing (i.e. the total heating) and not on its temporal evolution. The transient response is composed of a spectrum of inertia-gravity waves, whose frequencies are confined between N^{-1} ($\mathcal{O}(10)$min) and f^{-1} ($\mathcal{O}(10)$h), and its amplitude will therefore be determined by the time scale of forcing in comparison to these intrinsic scales. Convoluting the Green's function solution with smoothly varying forcings of different durations but the same total buoyancy source (not shown) give the expected results: the transient amplitudes are large for any time scale smaller than N^{-1} and negligible for forcing scales long compared to GA timescale f^{-1}. The timescale of a heating introduced into the atmosphere by a convective cloud is typically $\mathcal{O}(1)$h and thus lies between the limits N^{-1} and f^{-1}. In this case, the initial sharp front in the transient response is smoothed to the time scale of the forcing function, but otherwise the response is similar to the Green's function shown above.

3.4   Diagnostics applicable to numerical simulations

Since the approximate equations considered here are linear they also apply to difference fields of two flows and thus may be employed to describe the evolution of errors from the cloud-scale up to the balanced part of the flow. The results of the analytical solution above describe how this evolution should occur and what parameters it depends on. These predictions can be tested in numerical simulations of flows and reveal the relevance of this picture in nature. In this section three diagnostics are suggested for this purpose.

3.4.1   Gravity wave propagation speed

The heat source in the present linear hydrostatic calculation is formulated as a sine-wave in the vertical with integer wavenumber m. The transient hydrostatic gravity waves excited by this heating have, as stated in (3.17), a horizontal phase speed $c_m = NH/m$. A heat source that is composed of various vertical modes m thus excites a spectrum of horizontally propagating gravity waves that spread out from the forcing region. However, since deep convection shows a maximum heating in the mid-troposphere, it will strongly excite the gravest tropospheric gravity wave mode, taking the form of a half-sine wave in the vertical between the ground and the tropopause ($m = 1$). This mode not only dominates in amplitude but also propagates faster (i.e. horizontal phase speed c_1) than all higher order modes and should be clearly visible in the resulting perturbation field. The identification of such a wave in non-linear numerical simulations of a convective cloud field can provide a first test for the GA process. If the perturbation heat source in a numerical simulation has a similar shape to that assumed in the analytical model and for typical midlatitudinal tropospheric values for N and H wave modes propagating with about $c_1 \sim 30 - 40\,\mathrm{ms}^{-1}$ should be apparent in the mid-troposphere. Furthermore the speed should be independent of the Coriolis parameter f. Due to the linearity assumption this should in particular also apply to the relative flow field between two numerical experiments, as for example has been already qualitatively demonstrated by SC15.

3.4.2 Circulation and vorticity

In the context of the model presented here, a heat source in the atmospheric flow (e.g. every convective cloud) spins up a geostrophically balanced buoyancy perturbation and an associated vortex on the length scale x_{GA} after the adjustment time t_{GA}, which remains approximately constant subsequently. A more realistic scenario will be obtained as a superposition of many such sources, each associated with a perturbed convective cloud. The resulting vortices superimpose, accumulate and modify the vorticity field of the flow on the length scale of the Rossby radius of deformation. This allows for the construction of a quantitative diagnostic that relates the vorticity to the heating (precipitation) on large scales. In the following the deepest vertical mode is considered ($m = 1$).

Consider an area A that is larger than the Rossby radius of deformation with convective activity inside of it. Let C be the circulation around the area or equally the integral of the vorticity over the area at a certain point in time. The change in circulation over a time interval $\Delta t = t_2 - t_1$ must equal the sum of the individual circulations generated by the clouds (heat sources) in the area and in the time interval, lagged by the adjustment time. If a cloud is well inside the area A (not close to the edges) then the circulation of the cloud with respect to A can be approximated by its circulation at infinite distance. Thus the circulation change with respect to A can be written as

$$\Delta C := C(t_2) - C(t_1) = \int dA\, \zeta(t_1) - \zeta(t_2) \approx \gamma_\infty \sum_{t_1 - t_{GA}}^{t_2 - t_{GA}} q_i \,, \tag{3.41}$$

where q_i is the total buoyancy source of cloud i in Joules (i.e. integrated in space and in time) and γ_∞ is the circulation at infinity of a single cloud normalized by its total heating.

The buoyancy source can then be related to the precipitation rate. Assuming that all precipitation is in the liquid phase when it reaches the ground and that contributions from cloud water and ice can be neglected, the circulation change can be approximated by

$$\Delta C \approx \gamma_\infty l_v \int_{t_1 - t_{GA}}^{t_2 - t_{GA}} dt \int dA\, P(x, y, t) \,, \tag{3.42}$$

with P being the rain rate at the ground (in $\mathrm{kg\,m^{-2}\,s^{-1}}$) and l_v the specific heat of vaporization. Both sides of (3.42) can easily be evaluated from a numerical simulation, since it only requires standard output variables. Note that in the absence of heating (precipitation) (3.42) reduces to Kelvin's circulation theorem.

For quiescent background flows a vorticity diagnostic can be derived from (3.42) without the need to specify an area A. Since the circulation divided by area equals the vorticity on the scale of the area, (3.42) states that changes in the coarse-grained vorticity field are related to the history of the coarse-grained precipitation field, the latter again lagged by the adjustment time. This can be written as

$$\Delta \bar{\zeta}(x, y) \approx \gamma_\infty l_v \int_{t_1 - t_{GA}}^{t_2 - t_{GA}} \bar{P}(x, y, t)\, dt, \tag{3.43}$$

where the overbars denote a spatial coarse-graining, e.g. a Fourier filter that removes all scales smaller than the Rossby radius of deformation.

The parameter γ_∞ can be derived from the analytical model presented above. However, to use it for a quantitative comparison with standard numerical simulations of the atmosphere the slab-symmetry applied so far is inappropriate. In a fully three-dimensional simulation of a convective cloud field, the balanced motions spun up by convective cells overlap and superimpose and the solution of the balanced state is expected to have a different dependence on horizontal distance from the source than for the slab-symmetric counterpart. To enable a quantitative comparison of the circulation arising from the analytical solution and the numerical simulations the radially symmetric analogue of (3.30) will be presented in the following. The reader might well skip ahead to (3.56), where the desired value of γ_∞ is given based on the radially symmetric mathematical model outlined in the following.

While the radially-symmetric calculation is generally analogous to the slab-symmetric calculation presented in section 3.2, there are, however, differences arising from the altered geometry that will be pointed out here for completeness. If not stated otherwise, definitions introduced in section 3.2 hold.

The non-dimensional radially symmetric partial differential equation (PDE) for the buoyancy (see (3.19)) with scale $\mathcal{B}_r$ reads

$$\left\{\partial_{\tilde{t}}^3 \partial_{\tilde{z}}^2 + \partial_{\tilde{t}}(\partial_{\tilde{r}}^2 + \tilde{r}^{-1}\partial_{\tilde{r}}) + \partial_{\tilde{t}}\partial_{\tilde{z}}^2\right\} \tilde{b}_m(\tilde{r}, \tilde{z}, \tilde{t}) \tag{3.44}$$

$$= \partial_{\tilde{z}}^2(\partial_{\tilde{t}}^2 + 1)\,\tilde{Q}(\tilde{r}, \tilde{z}, \tilde{t})\,, \tag{3.45}$$

where $\tilde{r}$ is the radial distance from the source with $\tilde{r} = \sqrt{\tilde{x}^2 + \tilde{y}^2}$ and the forcing is given by (see (3.6))

$$\mathcal{Q}\tilde{Q}(\tilde{r}, \tilde{z}, \tilde{t}) = \frac{Q_0}{\mathcal{L}_h \mathcal{T}} \frac{\delta(\tilde{r})}{2\pi\tilde{r}} \delta(\tilde{t}) \sin(m\tilde{z})\,. \tag{3.46}$$

Using (3.7) and integrating over air mass and time this buoyancy forcing approximates a total heating of

$$Q_{h,tot} = \frac{2H_{\text{trop}}Q_0 c_v T_0 \rho_0}{g\pi}\,, \tag{3.47}$$

again assuming background values for temperature and density. The scaling of $\mathcal{T}, \mathcal{L}_h$ and $\mathcal{L}_v$ is chosen as in table 3.1, with the only difference being the horizontal coordinate $r \sim \mathcal{L}_h \tilde{r}$. Note that, however, the scaling of the other variables in the equations has changed due to the altered geometry. The relevant scales of the radially symmetric problem are given in table 3.2.

The $\tilde{z}$-dependence can be separated out as before with $\tilde{b}_m(\tilde{r}, \tilde{z}, \tilde{t}) = \tilde{B}_m(\tilde{r}, \tilde{t})\sin(m\tilde{z})$. The Laplace-transformed PDE (3.44) for the buoyancy amplitude $\tilde{\beta}_m(\tilde{r}, \tilde{s}) = \mathcal{L}\left\{\tilde{B}_m(\tilde{r}, \tilde{t})\right\}$ takes the form of a modified Bessel's equation

$$\left\{\partial_{\tilde{r}}^2 + \frac{1}{\tilde{r}}\partial_{\tilde{r}} - m^2(\tilde{s}^2 + 1)\right\} \tilde{\beta}_m(\tilde{r}, \tilde{s}) = -m^2(\tilde{s} + \tilde{s}^{-1})\frac{\delta(\tilde{r})}{2\pi\tilde{r}}\,. \tag{3.48}$$

Table 3.2: Scaling of Ψ in radially symmetric geometry in terms of N, f, Q_0 and H.

$\mathcal{T}$	$\mathcal{L}_v$	$\mathcal{L}_h$	$\mathcal{B}_r$	$\mathcal{V}_r$	$\mathcal{Z}_r$	$\mathcal{C}_r$
f^{-1}	H	$\frac{NH}{f}$	$\frac{Q_0 f^2}{N^2 H^2}$	$\frac{Q_0 f^2}{N^3 H^2}$	$\frac{Q_0 f^3}{N^4 H^3}$	$\frac{Q_0 f}{N^2 H}$

The following steps are performed analogously to (3.24)-(3.27) of the slab-symmetric calculation and the inverse Laplace transform formally reads as before

$$\tilde{B}_m(\tilde{r}, \tilde{t}) = \frac{m^2}{2\pi} \left\{ \partial_{\tilde{t}} \tilde{G}(\tilde{r}, \tilde{t}) + \int_0^{\tilde{t}} \tilde{G}(\tilde{r}, \tilde{t}') \, d\tilde{t}' \right\} \tag{3.49}$$

where

$$\tilde{G}(\tilde{r}, \tilde{t}) = \mathcal{L}^{-1} \left\{ \mathcal{K}_0 \left(m\sqrt{\tilde{s}^2 + 1}\, \tilde{r} \right) \right\} . \tag{3.50}$$

Here, $\mathcal{K}_i(\cdot)$ is the modified Bessel function of second kind and order i. Note that finding the inverse Laplace transform given in (3.50) is one major difference compared to the slab-symmetric calculation where $G(\tilde{r}, \tilde{t})$ took a different form (see (3.29)).

The inverse Laplace transform (3.50) can now be found by inserting the integral representation of the modified Bessel function of second kind and order ν (Abramowitz and Stegun, 1964, formula 9.6.25)

$$\mathcal{K}_\nu(xz) = \frac{\Gamma(\nu + 1/2)(2z)^\nu}{\sqrt{\pi} x^\nu} \int_0^\infty \frac{\cos(x\eta)}{\sqrt{\eta^2 + z^2}} d\eta \, ,$$

where $\Gamma(\cdot)$ is the generalized Gamma-function, into the Bromwitch formula

$$\mathcal{L}^{-1} \{ f(s) \} = \frac{1}{2\pi i} \int_{c-\infty i}^{c+\infty i} \exp(st) f(s) \, ds \, .$$

After some basic algebraic operations (that totally didn't take the author of this thesis a week) it follows

$$\tilde{G}(\tilde{r}, \tilde{t}) = \frac{\cos(\tilde{\tau}_r^r)}{\tilde{\tau}_r^r} \mathsf{H}(\tilde{t}_r^r) \, , \tag{3.51}$$

where

$$\tilde{t}_r^r = \tilde{t} - m\tilde{r}$$

$$\tilde{\tau}_r^r = \sqrt{\tilde{t}^2 - (m\tilde{r})^2}$$

are non-dimensional retarded times in radially symmetric geometry. The buoyancy solution thus reads

$$
\tilde{b}_m(\tilde{r}, \tilde{t}, \tilde{z})
$$
$$
= \frac{m^2}{2\pi} \left\{ \frac{\cos(\tilde{\tau}_r^r)}{\tilde{\tau}_r^r} \delta(t_r^r) - \frac{\tilde{t}\cos(\tilde{\tau}_r^r)}{(\tilde{\tau}_r^r)^3} \mathsf{H}(t_r^r) \right.
$$
$$
\left. - \frac{\sin(\tilde{\tau}_r^r)}{(\tilde{\tau}_r^r)^2} \mathsf{H}(t_r^r) + \int_{\tilde{r}}^{\tilde{t}} \frac{\cos(\tilde{\tau}_r^r)}{\tilde{\tau}_r^r} \, d\tau \right\} \sin(m\tilde{z}) . \tag{3.52}
$$

Note that setting $f = 0$ in the fully dimensional form of this solution basically leads to the nonrotating radially symmetric solution presented by BS89. However, BS89 solve for a Heaviside-function forcing in time, and thus the present Green's function solution takes the form of the temporal derivative of the BS89 solution (for $f = 0$). The present solution, as in the slab-symmetric case, can in principle be employed to construct an analogous solution for forcing functions with arbitrary spatial and temporal shapes. Note that, however, the convolution operation in cylindrical coordinates is two-dimensional in nature and can only marginally be simplified for radial symmetry (Baddour, 2009) which renders its practical computation much more complicated than in the slab-symmetric case.

From (3.52) the balanced part of $\tilde{b}_m(\tilde{r}, \tilde{t}, \tilde{z})$ can be obtained in the limit $\tilde{t} \to \infty$ as

$$
\tilde{b}_m^{\mathrm{b}}(\tilde{r}, \tilde{z}) = \lim_{\tilde{t} \to \infty} \tilde{b}_m(\tilde{r}, \tilde{t}, \tilde{z}) = \frac{m^2}{2\pi} \mathcal{K}_0(m\tilde{r}) \sin(m\tilde{z}) . \tag{3.53}
$$

Note from (3.53) that transitioning from slab- to radially symmetric geometry leads to a balanced flow that has a shorter horizontal scale (i.e. more rapid decay of $\mathcal{K}_0(\tilde{r})$ than $\exp(-|\tilde{x}|)$ in (3.37) with spatial coordinate, see also Chagnon and Bannon (2001)).

Using hydrostatic and geostrophic balance the geostrophic wind associated with $\tilde{b}_m^{\mathrm{b}}(\tilde{r}, \tilde{z})$ can be derived and reads

$$
\tilde{v}_m^{\mathrm{g,b}}(\tilde{r}, \tilde{z}) = \frac{m^2}{2\pi} \mathcal{K}_1(m\tilde{r}) \cos(m\tilde{z})
$$

with the associated dimension $\mathcal{V}_r$ in table 3.2. The balanced geostrophic vorticity in the radially-symmetric geometry $\tilde{r}^{-1}\partial_{\tilde{r}}(\tilde{r}\tilde{v}_m^{\mathrm{g,b}}(\tilde{r}, \tilde{z}))$ and has the scale $\mathcal{Z}_r$ in table 3.2 and is given by

$$
\tilde{\zeta}_m^{\mathrm{g,b}}(\tilde{r}, \tilde{z}) = \frac{m^3}{2\pi} \left[\frac{\mathcal{K}_1(m\tilde{r})}{\tilde{r}} - \frac{1}{2}\{\mathcal{K}_0(m\tilde{r}) + \mathcal{K}_2(m\tilde{r})\} \right] \cos(m\tilde{z}) .
$$

In order to construct a diagnostic that relates the forcing (heating rate Q_0) with the amplitude of the generated balance flow, the circulation $\tilde{Z}_m^{\mathrm{g,b}}(\tilde{r}, \tilde{z})$ is calculated as the area-integral of the geostrophic vorticity $\tilde{\zeta}_m^{\mathrm{g,b}}(\tilde{r}, \tilde{z})$ and reads

$$
\tilde{Z}_m^{\mathrm{g,b}}(\tilde{r}, \tilde{z}) = \int_0^{2\pi} d\phi \int_0^{\tilde{r}} \tilde{r}' \, \mathcal{Z}\tilde{\zeta}_m^{\mathrm{g,b}}(\tilde{r}', \tilde{z}) \, d\tilde{r}'
$$
$$
= -m^2 \left\{ \tilde{r}\, \mathcal{K}_1(m\tilde{r}) - 1 \right\} \cos(m\tilde{z}) . \tag{3.54}
$$

The dimension associated with the circulation is denoted as $\mathcal{C}_r$ and given in table 3.2. The result (3.54), together with table 3.2, indicates that at a radius that is constant relative to R_d the amplitude of the circulation depends linearly on f. The circulation at large distances is finite and approaches

$$\lim_{\tilde{r}\to\infty} \tilde{Z}_m^{\mathrm{g,b}}(\tilde{r}, \tilde{z}) = m^2 \cos(m\tilde{z}) . \tag{3.55}$$

Thus, for radial symmetry it follows from (3.47) and (3.54) that

$$\gamma_\infty := \frac{Z_1^{\mathrm{g,b}}(\infty, z)}{Q_{h,tot}} = \frac{g f \pi^2}{2 c_p T_0 \rho_0 N^2 H_{\mathrm{trop}}^2} \cos\left(\frac{\pi z}{H_{\mathrm{trop}}}\right) . \tag{3.56}$$

Typical mid-tropospheric values for density and temperature ($T_0 = 250\,\mathrm{K}$, $\rho_0 = 0.7\,\mathrm{kg\,m^{-3}}$) thus lead to an (anticyclonic) circulation near the tropopause ($z = H_{\mathrm{trop}}$) of $-2.8 \cdot 10^{-12}\,\mathrm{m^2\,s^{-1}}$ per Joule of diabatic heating or $-6.8 \cdot 10^{-6}\,\mathrm{m^2\,s^{-1}}$ per kilogram of precipitation.

A vorticity diagnostic can be further derived from (3.42) without the need to specify an area A. Since the circulation divided by area equals the vorticity on the scale of the area, equation (3.42) states that temporal changes in the coarse-grained vorticity field are related to the coarse-grained precipitation rate, temporally shifted by the adjustment time. This can be written as

$$\frac{d}{dt}\bar{\zeta}(x, y, t) \approx \gamma_\infty l_v \bar{P}(x, y, t - t_{GA}), \tag{3.57}$$

where the overbars denote a spatial coarse-graining, e.g. a Fourier filter that removes all scales smaller than the Rossby radius of deformation and d/dt denotes the Lagrangian time derivative with respect to these large-scale particles. For a quiescent atmosphere it approximately equals the Eulerian time derivative. In this case (3.57) can easily be integrated over a certain time span and both sides of the equation can be compared. If the flow is not quiescent, e.g. a significant background flow is present, the circulation and vorticity diagnostics (3.42) and (3.57) are still valid but have to be applied in a Lagrangian reference frame. This means that the area A should be bounded by a material contour and d/dt describes the Lagrangian rate of change. The large-scale flow must however be sufficiently regular to ensure that the area A is not distorted to the point that its spatial extend is reduced to less than the Rossby radius of deformation in any direction and accordingly the definition of a large-scale particle is reasonable.

Because of the linearity all diagnostics above can be applied to error growth experiments by using difference fields between two runs as long as the runs are quiescent or large-scale advective differences remain small. Consider for example an experiment like SC15 where two simulations are identical until one is being perturbed with noise at time t_1. The evolution of vorticity and circulation in the difference field at the scale of the Rossby radius is then given by the differences in the precipitation field that originate from convective-scale error growth.

3.4.3   Rossby number

If the gravity wave transients are neglected, the flow that is associated with a buoyancy source changes during the GA process from significantly divergent to purely rotational. More generally, the ratio of divergence over rotation of the flow and its temporal evolution may

serve as a diagnostic for GA and has been applied to numerical simulations before (e.g. Zhang et al. (2007) and SC15). In SC15 this ratio was called a Rossby number and was defined as the root mean square (RMS) of the divergence over the RMS of the vorticity. It was applied to different ranges of spatial scales and to the relative flow between two experiments.

In this section the analytical model is used to predict how this diagnostic will evolve in time. To this end the flow generated by one pulse of forcing at the space-time origin as in (3.6) is considered. The transient parts of the solution will be neglected and thus only the circulation associated with the term b_m^{b} in (3.30) will be taken into account. For convenience the maximums norm $\|\cdot\|_{\max}$ is used here instead of the RMS. With this and (3.30) the Rossby number can be approximated as

$$\mathrm{Ro}(\tilde{t}) := \frac{\|\mathrm{div}\|_{\max}}{\|\mathrm{rot}\|_{\max}} \approx \frac{\left|\partial_{\tilde{t}} b(x=0,\tilde{t})\right|}{\left|b(x=0,\tilde{t})\right|} = \frac{\left|J_0(\tilde{t})\right|}{\left|\int_0^{\tilde{t}} J_0(t')dt'\right|} . \tag{3.58}$$

For $\tilde{t} \to 0$ the integral in the denominator approaches zero while the numerator is finite, resulting in a large Rossby number that indicates a mainly divergent flow. At later time the numerator oscillates towards zero while the denominator converges to a constant so that the Rossby number converges towards zero indicating a mainly rotational flow. The speed of this transition is according to (3.58) proportional to f since the Rossby number is a function of the non-dimensional time only. Therefore Ro is a suitable diagnostic to assess the adjustment timescale discussed in paragraph 3.3.2.

With regard to its application to more complex numerical simulations it has to be noted however that the diagnostic (3.58) is non-linear and a simple superposition principle as in (3.41) does not apply. Therefore the exact value of Ro at a certain time will depend on many other aspects of the considered flow and cannot be predicted from this simple consideration. One the other hand (3.58) is independent of the strength of the forcing and since spatial superposition of clouds affects the numerator and the denominator in the same way, the f-scaling should be robust and could be tested in numerical experiments with varying rotation rates.

3.5   Summary

In this chapter, an analytical model for the geostrophic adjustment (GA) of an initially localized heating imposed in a quiescent atmosphere was examined. The model is based on the linearized, hydrostatic slab- and radially symmetric Boussinesq equations. A solution is found for the buoyancy perturbation arising from an impulsive, localized heating and all other atmospheric flow components can be derived from this. The present solution is in good agreement with previous analytical studies that examined the GA mechanism (Schubert et al., 1980; Chagnon and Bannon, 2005a,b). The localized delta-forcing of the presented model allows for a specification of the Green's function of the employed set of equations and thus a straightforward deduction of the solution for an arbitrary spatio-temporal forcing by superposition. Furthermore, the solution includes all (transient and balanced) flow components and thus in particular the temporal evolution of the balanced flow can be estimated (in contrast to Gill,

1982, who considers only the large-time limit).

With these generalizations, scaling characteristics and diagnostics that may help to identify the GA mechanism in more complex numerical simulations can be derived. In particular the following three diagnostics are suggested:

1. The analytical model predicts gravity waves with phase speeds that are independent of f and inversely proportional to the vertical mode m of the forcing. In agreement with previous studies it is assumed that the convection projects mainly onto the gravest vertical mode ($m = 1$), which results in a phase speed of the waves of $c_1 = NH$.

2. The analytical model suggests a relationship between changes in the balanced, large-scale vorticity and the time-lagged latent heating. For an evaluation of this relationship the precipitation can be used as a proxy for the latent heating.

3. When neglecting the transients the response to the heat source evolves over time from purely divergent to purely rotational. The timescale of this transition is proportional to f^{-1}. The ratio of divergence over vorticity (Rossby number) can be extracted from numerical simulations and the f-dependence of its evolution can be tested.

The limitations of the results presented in this chapter as well as possible future studies are generally discussed in chapter 5. However, one limitation of the presented calculation is relevant to the following chapter and will thus be discussed here.

Linearity is one major assumption which underlies the presented calculation and implies that the amplitude of the flow that is generated by the heat sources remains small. The linear and also the hydrostatic assumptions are clearly violated within the convective clouds themselves. However, heating by convective clouds typically generates small amplitude flow responses implying that linearity is expected to hold for the wave response and secondary circulation excited by the heating (Nicholls et al., 1991; Schubert et al., 1980). If the linearity assumption holds the predictions of the analytical model can be applied to single convective clouds as well as to a field of convective clouds by linear superposition. In addition they can be applied to difference fields between two simulations in the context of an error growth study.

While the strong assumptions underlying the analytical calculation presented here render the comparison between the analytical solution and simulations of observed weather situations complicated, it is possible that the GA process could be unambiguously identified in an idealized numerical setup. Consider a simulation of a field of convective clouds, without a large-scale background flow. If the flow is perturbed on small scales (as in Selz and Craig, 2015b), the upscale growth of the perturbations is predicted to follow the GA evolution shown by the analytical solution, with temporal and spatial scales of f and R_d respectively. This scaling could be tested by varying the Coriolis parameter carefully (i.e. such that the scale separation between the convective forcing scale and R_d is guaranteed, Shutts and Gray, 1994). In this way the three diagnostics presented in this chapter could be applied to demonstrate whether GA is responsible for the upscale error growth. In the following chapter, the results of such experiments will be presented.

Chapter 4

Upscale error growth from convection through geostrophic adjustment: idealized numerical simulations

4.1 Introduction

In paragraph 1.3.2 the three-stage conceptual error growth model following Zhang et al. (2007) (see also schematic illustration in Fig. 1.8) was introduced. In there, errors imposed on the small-scales initially grow from the convective instability (stage 1) and ultimately perturb the large-scale balanced flow (stage 3). Indications for the geostrophic adjustment (GA) following an imbalance imposed on the atmosphere by deep moist atmospheric convection as a possible mechanism underlying the intermediate stage 2 of this model were found in numerical error growth studies (Zhang et al., 2007; Selz and Craig, 2015b). In the previous chapter 3, an analytical solution describing the GA of a localized, impulsive heating generated by the latent heat release within a convective cloud was found. The calculation was based on the linearized, hydrostatic slab- and radially-symmetric Boussinesq-equations. In there, three diagnostics that allow for an identification of the GA mechanism in numerical error growth experiments were suggested (see section 3.5):

1. The hydrostatic deepest tropospheric gravity wave mode propagating with the associated horizontal phase speed should be clearly identifiable. This phase speed should be independent of the Coriolis parameter f.

2. The large-scale vorticity is linearly related with the accumulated divergence (convertible to the precipitation rate) through a proportionality factor αf (with α constant).

3. A scaling in space and time with the Rossby radius of deformation and the Coriolis parameter respectively renders the solution and derived quantities (such as the Rossby number) universal.

The study presented in this chapter aims at closing the gap in the hierarchy of complexity between the analytical investigation of the GA process presented in chapter 3 and the complex numerical studies shown by Zhang et al. (2007) and Selz and Craig (SC15 2015b, in the

following). To that end, idealized numerical perturbation experiments are performed within a convective cloud field in a rotating environment.

Several idealized numerical studies addressed the impact of convective clouds on the environment in non-rotating and rotating frameworks. Studies that examine non-rotating environments focus on the wave response excited by the convective heating (depending on whether the model is (in-) compressible: acoustic-, Lamb- and gravity waves; Chagnon and Bannon, 2005a). Bretherton and Smolarkiewicz (1989) and Mapes (1993) found that an isolated heating as introduced into the atmosphere by a single convective cloud in an idealized hydrostatic two-dimensional numerical model excites a spectrum of horizontally propagating gravity waves that communicates the imposed perturbation to the surrounding atmosphere. Nicholls and Pielke (2000) additionally found in a three-dimensional and compressible cloud model that the deepest tropospheric gravity mode (vertical wavenumber 1) propagates fastest, thus dominates the response and produces deep subsidence warming that compensates for the upward transport of mass by convection (see also Lane and Reeder, 2001). In numerical studies that examine the response of a rotating atmosphere to a heating imposed by a convective cloud, basic characteristics of the non-rotating systems wave response still hold. The waves are, however, constrained by the rotation. They do not propagate out from the source region infinitely and a balanced state evolves after the geostrophic adjustment process (Liu and Moncrieff, 2004). It was found that the propagation properties of the deepest tropospheric gravity wave modes nevertheless do not depend on the rotation rate (Liu and Moncrieff, 2004), where the relative contributions of transient and balanced energies to the total budget do (Shutts and Gray, 1994; Gray, 1996).

The main goal of this chapter is to test whether the dynamical process that underlies upscale error growth through the atmospheric mesoscales is GA. To that end, idealized simulations of a convective cloud field on a f-plane (i.e. constant Coriolis parameter imposed) are performed with a non-hydrostatic, fully three-dimensional atmospheric numerical weather prediction model on a large domain. In order to test the suggested scaling with f, three control-simulations with different close-to planetary rotation rates are performed. For each of the simulations a slightly perturbed twin experiment is conducted and the error growth is examined in the difference field (between a control and perturbed simulation). Apart from the comparison of traditional error growth measures employed by foregoing studies (such as Rossby number and domain-integrated difference total energy, see Figs. 1.9 and 1.10), the theoretical concept of GA is reconciled with the study of upscale error growth through the atmospheric mesoscales by testing the three predictions made in chapter 3 for the GA process in the numerical simulations.

The current chapter is structured as follows: in a first part, the employed numerical model and the set up of the simulations are introduced. Then, the kinetic energy spectrum and the domain-integrated difference total energy as standard error growth measures are briefly discussed. In the next section, the perturbed simulations are examined by testing the three predictions for GA by the analytical model. The chapter concludes with a summary.

4.2   Experimental setup

In this chapter, numerical simulations are performed with the atmospheric numerical weather prediction model provided by the Consortium of Small-Scale modeling (COSMO; Baldauf et al., 2011). Note that as opposed to the global MPAS model employed in chapter 2, the COSMO-model is a high-resolution limited-area model. The fully non-hydrostatic and compressible COSMO model is based on the primitive thermo-hydrodynamical equations. Various subgrid-scale processes (e.g. turbulent diffusion, radiation, shallow convection, soil-processes and soil-atmosphere interactions) are parametrized in the model which is utilized operationally with a horizontal resolution of 2.8 km at the German National Meteorological Service (DWD). This horizontal resolution is understood to be high enough to (at least partly) explicitly simulate deep moist convection (convection-permitting) and only shallow convection is parametrized. The effective resolution (i.e. the wavelength at which the model spectrum decays relative to a simulation with finer grid spacing) amounts to $4-5$ times the horizontal grid-spacing (Bierdel et al., 2012) and scales smaller than this are not represented accurately.

Version 5.0 of COSMO is used in idealized mode on a f-plane with periodic lateral boundaries and a homogeneous flat landscape at an elevation of 500 m as lower boundary. The horizontal coordinates cover 1601 grid points spaced at a distance of 2.8 km. The resulting large horizontal domain of approximately 4500×4500 km is chosen to cover several times the Rossby radius of deformation, which leads to an accurate representation of the larger scales of the flow. In the vertical the model has 57 grid points with resolution decreasing from ~ 100 m at the lower boundary to 800 m at the model top at 30 km. The model is initialized homogeneously with an sounding that was taken in Payerne, Switzerland (CH, Radiosonde 06610) at 12 UTC 30 July 2007. The sounding is very unstable with a Convective Available Potential Energy (CAPE) of 2000 J kg and preceded the formation of strong convective storms and mesoscale convective systems (Bischof, 2011). Note that for better comparability with the theoretical results from chapter 3 and unlike in Lange and Craig (2014), the horizontal wind of the sounding is set to zero and no convective organization occurs. Here, convection is initialized by holding the soil temperature constant at a value 3 K higher than the lowest data point of the initial sounding and by a long-wave radiative cooling that further destabilized the atmosphere. The initial symmetry of the atmosphere is slightly perturbed with a Gaussian-distributed uncorrelated grid-scale noise with zero mean and a standard-deviation of 0.05 K on the temperature field in all model levels. The described experiments (control runs, CTRL) are performed from 0 to 110 h for three different rotation rates $f_0 = 1.03 \cdot 10^{-4} \text{s}^{-1}$, $1.5 f_0$ and $2 f_0$. The rotation rates are chosen such that the time- and length scales of the adjustment process change significantly enough to be detected in the employed diagnostics, but in a manner that the scale separation between the forcing (i.e. convective) and adjustment scales (Rossby radius of deformation R_d) is guaranteed (Shutts and Gray, 1994).

In order to give a visual impression of the simulated flow field an exemplary horizontal wind field is shown in Fig. 4.1. In there, the absolute value of the upper-tropospheric horizontal wind field $|\boldsymbol{v}_h|$ is shown for the CTRL-run and f_0. The total simulation lead time $t = 72$h has been chosen rather arbitrarily, but lies within the period where the perturbation experiments are performed (i.e. perturbation lead time 22h, see below).
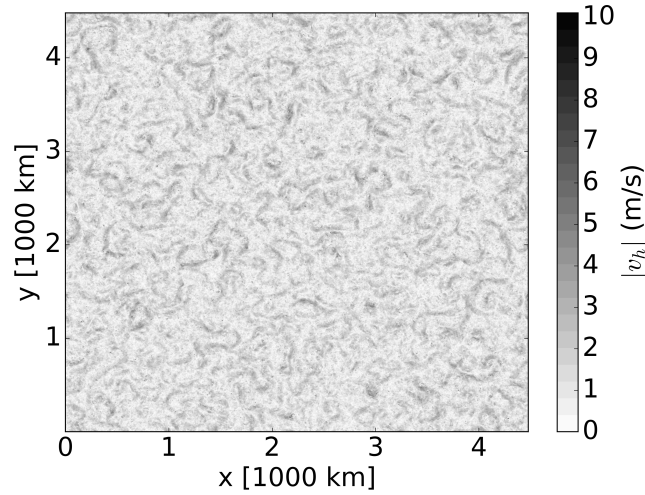
Figure 4.1: Absolute value of the horizontal wind field $|\boldsymbol{v}_h|$ in m/s for the CTRL run with Coriolis parameter f_0 at total hour 72 (perturbation lead time 22h) and upper-tropospheric heights ($z \sim 10\,\mathrm{km}$)

In Fig. 4.2 the area-mean precipitation rate is shown for the three CTRL-runs as a function of model lead time. The initial rapid increase of the precipitation rate is associated with the onset of strong, short-lived and small-scale convection after a couple of hours. The onset of convective activity is associated with a rapid decrease in CAPE (not shown), which has a negative feedback on the convective activity and results in the drop of the precipitation rate until around 25 h. After the initial transients and convective clouds have decayed, convective activity arises with smaller mean precipitation rates that level out on $0.12\,\mathrm{mm\,h^{-1}}$.

Figure 4.2: Temporal evolution of the area-mean precipitation rate of the CTRL runs for the three rotation rates f_0, $1.5f_0$ and $2f_0$ (solid, dashed and dotted respectively). The vertical gray line depicts the time at which the perturbation is added.

For each of the three CTRL simulations a slightly perturbed twin experiment (PERT) is conducted, where (following SC15), Gaussian-distributed, uncorrelated grid-scale noise with zero mean and a stand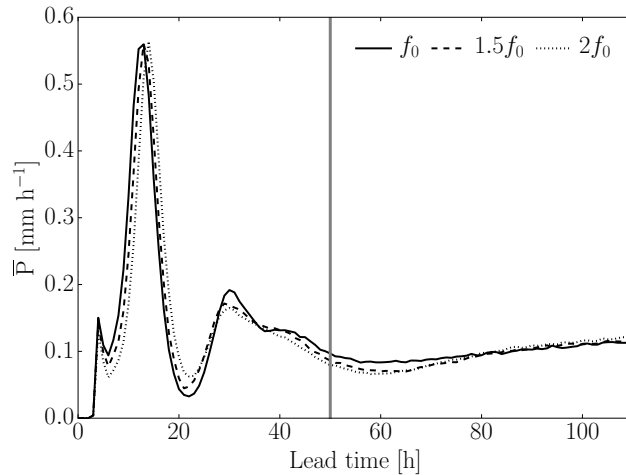ard deviation of $0.01\,\mathrm{K}$ is added to the temperature field on all levels after $50\,\mathrm{h}$ model run time and the model runs freely for $60\,\mathrm{h}$. The instant where the perturbations are imposed on the background flow and the time span of the PERT experiments were chosen such that the GA process can be identified from upscale error growth characteristics: first, no other dynamical process or balance dominates the GA mechanism on respective scales. Second, the small-scale forcing (i.e. convective activity) is independent of f. Due to the imposed rotation the atmosphere approaches a state with fast rotating, small-scale low-pressure systems that are separated on a distance of the order of the Rossby radius of deformation (Nolan et al., 2007; Khairoutdinov and Emanuel, 2013). However, in the time span of 50-110 h of the present simulation, the background flow is still characterized by a convective cloud field that did not enter a regime where larger-scale storms have developed and other dynamical processes (such as cyclostrophic balance) dominate the GA process (see Fig. 4.1). The Rossby-number of the background flow is constant (not shown), indicating that there is no significant drift in the (rotational) background flow. Additionally, the convective-scale forcing is after the decay of initial transients to a good approximation independent of f (see Fig. 4.2). The chosen time-span of $50 - 110\,\mathrm{h}$ thus fulfills both requirements.

4.3 Error growth measures

Before the three predictions made by the analytical model will be employed to extract the GA mechanism from the numerical simulations, the kinetic energy spectrum and the domain integrated difference total energy (diDTE) will be introduced as two standard diagnostics in studies of upscale error growth.

Spatial kinetic energy (E_K) spectra give substantial insight into the distribution of energy amongst different scales of motion in a flow field and are calculated in the traditional way (see Skamarock, 2004; Bierdel et al., 2012). E_K spectra of the horizontal difference wind ($\delta \boldsymbol{v}_h(x,t) = \boldsymbol{v}_{h,\mathrm{PERT}}(x,t) - \boldsymbol{v}_{h,\mathrm{CTRL}}(x,t)$) have been employed in error growth studies (Durran et al., 2013; Selz and Craig, 2015b) to identify the speed of error growth and associated saturated scales (i.e. the scale at which the error spectrum has the same amplitude as the background spectrum). The slope of the background E_K spectrum furthermore sets the predictability time in models that interpret upscale error growth as a turbulent cascade (see also sections 1.3 and 4.5, Lorenz, 1969; Rotunno and Snyder, 2008).

In Fig. 4.3 the E_K spectrum, averaged temporally between $50\,\mathrm{h}$ and $110\,\mathrm{h}$ and vertically over the free troposphere of the CTRL runs is shown in the traditional double-logarithmic axis. The kinetic energy spectra are very similar for the three rotation rates with respect to amplitude per wavenumber and spectral slope. For all three rotation rates, E_K has little energy on the largest scales, peaks at a wavelength at around $200 - 500\,\mathrm{km}$ and drops off more shallow than the measured $k^{-5/3}$ spectral dependence on the atmospheric mesoscales, with an approximate $k^{-1.4}$ slope (see dashed gray line in Fig. 4.3). The build-up of an E_K spectrum with significant mesoscale energy in a flow field that only features small-scale convection confirms findings by recent studies (Waite and Snyder, 2013; Sun et al., 2017). This aspect particularly concerns
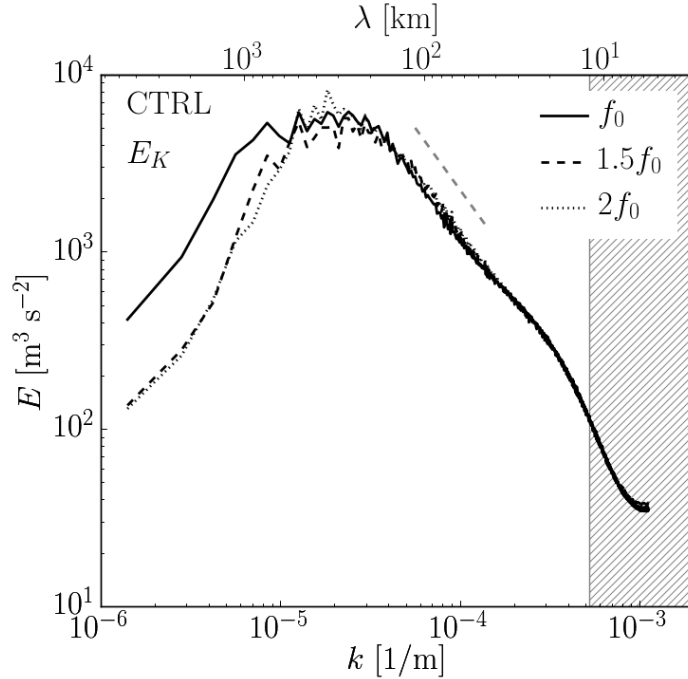
Figure 4.3: Kinetic energy spectrum of the CTRL runs averaged over times $50 - 110\,\mathrm{h}$ in double logarithmic space. Spectra are calculated on horizontal levels in the free atmosphere and then averaged. Rotation rates of f_0, $1.5f_0$ and $2f_0$ are indicated as solid, dashed and dotted lines respectively. The gray dashed line indicates a spectral slope $k^{-1.4}$ and the hatched area marks wavelengths below the effective resolution.

the vital debate about the dynamic origin of the mesoscale E_K spectrum (Bierdel et al., 2016, and references therein). However, the examination of the dynamic origin of the mesoscale energy spectrum is beyond the scope of this chapter.

The domain integrated difference total energy (diDTE) is a simple norm for error growth that has been employed by foregoing studies (Zhang et al., 2003; Selz and Craig, 2015b). Initially introduced by Ehrendorfer and Errico (1995), the diDTE involves the horizontal wind components u and v and the temperature T and reads

$$\mathrm{diDTE}(t) = \frac{1}{V} \int_V \frac{1}{2} \left[(\delta u)^2 + (\delta v)^2 + \frac{c_p}{T_r} (\delta T)^2 \right] dV \tag{4.1}$$

where $\delta\psi$ refers to the difference of field ψ between a perturbation and control run ($\delta\psi = \psi_{\mathrm{PERT}} - \psi_{\mathrm{CTRL}}$), V is the integration volume, c_p is the heat capacity of dry air at constant pressure and $T_r = 287\,\mathrm{K}$ is a reference temperature.

The diDTE is separated with a Fourier filter into the small convective scales S and the larger scales L where the balanced flow is expected to emerge. The scale ranges for the f_0-run are chosen as $S = 0 - 200\,\mathrm{km}$ and $L > 200\,\mathrm{km}$ (see SC15) and the scale ranges for $1.5f_0$ and $2f_0$ are scaled according to R_d (i.e. $1.5f_0 : [0 - 133]\,\mathrm{km}$, $[> 133]\,\mathrm{km}$ and $2f_0 : [0 - 100]\,\mathrm{km}$, $[> 100]\,\mathrm{km}$).
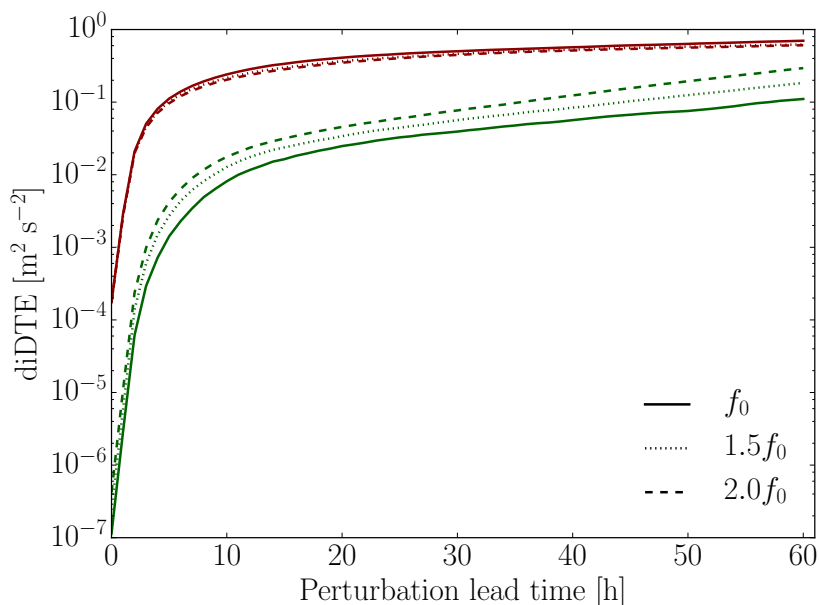
Figure 4.4: diDTE as a function of perturbation lead time on a semi-y-log scale for the three different rotation rates f_0 (solid), $1.5f_0$ (dashed) and $2f_0$ (dotted). The scaled S and L scales are displayed in red and green respectively.

The diDTE for the scaled S and L ranges is displayed for the three rotation rates as a function of perturbation lead time in Fig. 4.4. The small-scale error growth properties (red curves) are not significantly different for the three rotation rates. SC15 show that the speed of the error growth and the final amplitude of the errors in stage 1 of the conceptual model are related to the CAPE and precipitation rate respectively. Thus, given the independence of the mean precipitation rate (see Fig. 4.2) and CAPE (not shown) of f the independence of the diDTE on the S-scales is an expected result. On the larger scales (green curves), the initial (i.e. first $2 - 3$ h) fast growth does not differ significantly between the three runs. On this scale range, however, the timescale of the saturation of the initial rapid error growth as well as final diDTE-level show a significant dependence on the rotation rate f. In particular, the diDTE takes the highest (lowest) value for the highest (lowest) rotation rate. This behavior qualitatively agrees with the expected scaling featured by the isolated GA mechanism, where the amplitude of the horizontal wind and the buoyancy scale linearly with f (see table 3.1) meaning that a heating of the same amplitude generates a large-scale balanced response with a higher amplitude for higher rotation rates. The large-scale diDTE is associated with the balanced part of the flow that evolves from the small-scale perturbation. According to the third diagnostic suggested based on the analytical model (see section 3.4), these diDTE-curves should take a unique shape (i.e. be independent of f) when time is scaled with the geostrophic adjustment time scale f^{-1}.

Primarily owing to the quadratic nature of the energy spectrum and the diDTE, comparing these two diagnostics for the analytical model (a single convective cloud and spin up of one associated balanced vortex, see chapter 3) and the numerical simulations (an ensemble of

convective clouds) is not straightforward. In the relative flow between a PERT and CTRL simulation, the shift of individual convective clouds appears as a field of massflux-dipoles. By taking the square the sign of the up- and downdrafts is lost. If a Fourier transform is applied to this squared field, the scale information will be only contained in the dipole separation distance as opposed to the actual spreading of errors amongst different scales of the flow. The same difficulty arises for the superposition of the E_K spectrum, where in particular the cloud spacing and clustering scales play a decisive role. As opposed to the balanced vortex scale, these cloud-separation distances do not scale with f and thus render the comparison between a single-cloud analytical solution and a cloud-ensemble numerical simulation complex.

For given reasons, for time, space and amplitude scaled with f, the E_K spectra and larger-scale diDTE curves of the different f-runs do not collapse onto each other. As indicated in chapter 3 there are diagnostics derived from the analytical model that are better suited to extract the GA mechanism from the idealized numerical simulations. These diagnostics will be discussed in the following section.

4.4 Test of GA in numerical simulations

In this part the three diagnostics developed in the analytical framework in chapter 3 are employed to identify the GA process in numerical error growth experiments with a full atmospheric model. To that end, the difference fields (perturbed minus control run) of the present numerical simulations will be examined.

4.4.1 Lag-correlation and gravity wave speed

In the analytical calculation a deep tropospheric (vertical wavenumber $m = 1$) hydrostatic, linear gravity wave front was predicted with f-independent horizontal propagation speed $c = NH(\pi)^{-1} = 36.6\,\mathrm{ms}^{-1}$ (with Brunt-Väisälä frequency $N = 0.01\,\mathrm{s}^{-1}$ (averaged over free troposphere) and scale height is $H = 11.5\,\mathrm{km}$, see chapter 3). This first baroclinic wave mode manifests itself in vertical displacements which are the most significant in the mid-troposphere (Nicholls et al., 1991). SC15 examine the temporal evolution of the $500\,\mathrm{hPa}$ DTE around a convective cell (see Fig. 1.10) and visually deduce the speed at which the perturbation spreads out as $c \approx 36.0\,\mathrm{ms}^{-1}$. The resemblance of the theoretical value and the value derived from the complex numerical simulation of a realistic weather situation suggests that deep tropospheric gravity waves might be the dynamical process that spreads the perturbations out from convective areas. To extract the gravest gravity wave mode from the present numerical simulations, the lag-correlation of the difference vertical velocity $\delta\omega(x,t) = \omega_{\mathrm{PERT}}(x,t) - \omega_{\mathrm{CTRL}}(x,t)$ at $500\,\mathrm{hPa}$ (i.e. the cross-correlation between $\delta\omega(x,t)$ and $\Delta\omega(x,t+\Delta t)$ for a time-lag Δt) is calculated. The horizontal distance of the maximum of the lag-correlation function then defines together with the time-lag Δt the gravity-wave speed c. Note that the presence of the deepest gravity wave mode is a characteristic of every (CTRL and PERT) simulation at any time. The signal is, however, more clear at early perturbation lead times and in the difference field where noise is filtered out and the signal-to-noise ratio is amplified.

Figure 4.5 shows the lag-correlation coefficient as a function of horizontal distance for three different time-lags $\Delta t = 10, 15, 20\,\mathrm{min}$ and Coriolis parameters f_0, $1.5f_0$ and $2f_0$. The lag-correlation has been averaged over seven different times t between 2 and 3 hours perturbation lead time. The correlation is as expected the greatest for very short distances and the overall values are small. There are, however, for the time-lags $\Delta t = 10, 15, 20\,\mathrm{min}$ distinct correlation maxima at $23.0, 33.6$ and 44.8 km that result in dominant gravity wave speeds 38.3, 37.7 and $37.3\,\mathrm{ms}^{-1}$, with an average of $37.6\,\mathrm{ms}^{-1}$. This result holds for all rotation rates (see comparison solid, dashed and dotted curves in Fig. 4.5) and has two major implications: first, the high level of agreement of the found gravity wave speed with the theoretical value suggests that in the complex, nonlinear numerical simulation the forcing through latent heat release within convection projects strongly on the deepest tropospheric mode and that the gravity wave response is linear (even if the convective forcing itself is highly nonlinear, see chapter 3). Second, the independence of the obtained result on f confirms the study by Liu and Moncrieff (2004) that the horizontal phase speed of the gravest tropospheric gravity wave mode is widely unaffected by the change in rotation rate. The universality of the propagation characteristics of the transient gravity waves excited by the convective forcing suggest that the experiments are well designed in a way that the change of the rotation rate does not affect other parameters that are relevant to the convective forcing (e.g. N, H). The clear sign of the gravest hydrostatic wave mode furthermore indicates that the perturbation heat source has a similar shape to that assumed in the linear model, which provides a first test for the GA mechanism in the fully nonlinear model simulation.
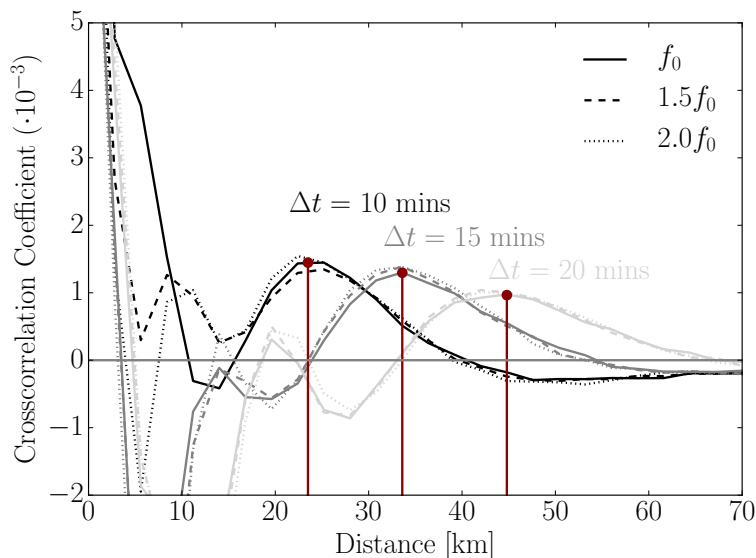
Figure 4.5: Lag-correlation coefficient $C_{\mathrm{lag}}(\Delta t)$ for $\delta\omega(x, t)$ at $500\,\mathrm{hPa}$ and $\Delta t = 10, 15, 20\,\mathrm{min}$ (black, gray and light gray respectively) as a function of horizontal distance. Solid, dashed and dotted lines are rotation rates f_0, $1.5f_0$ and $2f_0$ respectively. Red dots and lines depict correlation maxima of the f_0 curves.

4.4.2 Vorticity diagnostic

The second diagnostic derived from the analytical model for the identification of the GA process from numerical simulations suggested in chapter 3 is a direct relationship between the coarse-grained vorticity $\bar{\zeta}(x,y)$ (in s^{-1}) and precipitation rate anomaly $\bar{P}(x,y,t)$ (in $\mathrm{kg\,m^{-2}\,s^{-1}}$) which reads (see paragraph 3.4.2)

$$\delta\bar{\zeta}(x,y) \approx \alpha\,f\,\int_{t_1-t_{GA}}^{t_2-t_{GA}} \bar{P}(x,y,t)\,dt \tag{4.2}$$

$$\text{with}\quad \alpha = \frac{g\pi^2 l_v}{2c_p T_0 \rho_0 N^2 H^2}\,\cos\left(\frac{\pi z}{H}\right)\,.$$

In there, α is positive and depends on various constants and properties of the background sounding (i.e. specific heat of vaporization l_v, reference values for temperature and density T_0 and ρ_0, Brunt-Väisälä frequency N, tropopause height H, specific heat capacity of air at constant pressure c_p and acceleration through gravity g), but explicitly not on the Coriolis parameter. According to the physical picture established in chapter 3 associated with (4.2), every convective cloud spins up a geostrophically balanced buoyancy perturbation and an associated vortex on the length scale $x_{GA} \sim R_d$ (with $R_d = NHf^{-1}$ being the first baroclinic Rossby radius of deformation) after the adjustment time $t_{GA} \sim f^{-1}$. These vortices superimpose linearly, accumulate and modify the vorticity field of the flow on the length scale of R_d. Due to the linearity assumption, this picture also holds for the relative flow between a control- and a perturbed simulation and can thus be employed to study error growth. The vorticity field needs to be examined on scales larger than the Rossby radius. Only on these large scales of the flow, the full $\boldsymbol{v}_h$ field that underlies the vorticity diagnostic is associated with the balanced part of the flow.

Relationship (4.2) is now tested in the framework of the three numerical simulations with Coriolis parameters f_0, $1.5f_0$ and $2f_0$. The difference upper tropospheric vorticity (averaged over four levels between $9.5\,\mathrm{km}$ and $10.9\,\mathrm{km}$) and the difference accumulated precipitation are Fourier filtered, such that scales smaller than the associated R_d (i.e. $1000\,\mathrm{km}$, $670\,\mathrm{km}$ and $500\,\mathrm{km}$ for f_0, $1.5f_0$ and $2f_0$ respectively) are neglected. The height levels are chosen based on the sinusoidal vertical shape of (4.2) that predicts a maximal amplitude of the balanced vortex of positive sign at the tropopause and thus renders the signal most clear at this height. Note that according to (4.2), a linear scaling between the coarse-grained upper tropospheric vorticity and the associated accumulated precipitation field is expected to hold for the vorticity at time t and the accumulated precipitation until time $t - t_{GA}$. According to paragraph 3.3.2 in chapter 3, the adjustment timescale is given by $t_{GA} \sim 3.81f^{-1} \approx 10\,\mathrm{h}$. For simplicity and owing to the hourly numerical output, we consider $t_{GA} = 12\,\mathrm{h}, 8\,\mathrm{h}$ and $6\,\mathrm{h}$ for the f_0, $1.5f_0$ and $2f_0$ runs respectively.

In Fig. 4.6 the filtered vorticity at perturbation lead time $t = 58\,\mathrm{h}$ and the accumulated precipitation field at respective lagged times $t - t_{GA}$ are shown in the upper and lower row respectively for the three rotation rates f_0 (left), $1.5 f_0$ (center) and $2 f_0$ (right). A qualitative visual comparison of the vorticity- and associated precipitation fields reveals a high correlation between positive accumulated precipitation features and anticyclonic upper level vorticity anomalies. For higher rotation rates, a precipitation anomaly of certain amplitude generates a stronger vorticity feature, a relationship that is reflected in the proportionality factor $\alpha \cdot f$ in (4.2).
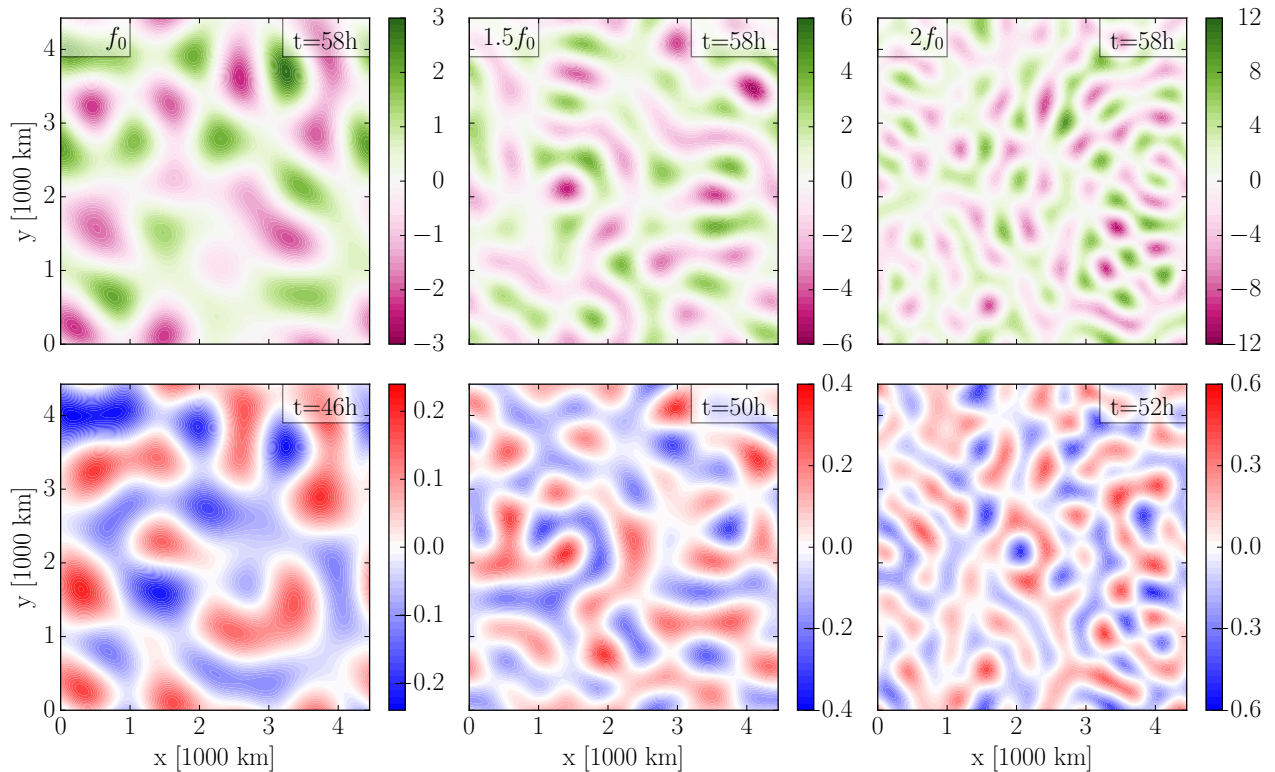
Figure 4.6: Spatially filtered (scales larger than respective R_d) upper-tropospheric vorticity (averaged between $9.5\,\mathrm{km}$ and $10.9\,\mathrm{km}$ height, upper row) and accumulated precipitation rate at ground (lower row) for the three rotation rates f_0 (left), $1.5 f_0$ (center) and $2 f_0$ (right). The vorticity is displayed for perturbation lead time $t = 58\,\mathrm{h}$ and the precipitation field for $t - \tau_{GA}$, where $\tau_{GA} = 12\,\mathrm{h}, 8\,\mathrm{h}$ and $6\,\mathrm{h}$ for f_0, $1.5 f_0$ and $2 f_0$ respectively. The vorticity has been multiplied by a factor of 10^6 for visualization.

Uniqueness of estimated slope

In order to extract α in (4.2) from the three present simulations, the vorticity fields shown in the upper row of Fig. 4.6 are scattered point-wise with the associated precipitation fields in the lower row and a linear functional fit is applied to the data. The slope of the fit then equals $\alpha \cdot f$, where the GA-hypothesis in hydrostatic linear theory predicts that α is independent of f. Since (apart from the constants g, π, l_v, c_p, T_0 and ρ_0) the tropopause height and stability of the atmosphere are found to be identical for the three f-runs (see paragraph 4.4.1), α is expected to be constant in all three numerical experiments.

Since the displayed vorticity and accumulated precipitation fields are large-scale Fourier-filtered, they are highly auto-correlated. While the quality of the slope estimate does not suffer from the redundant information contained in the underlying fields (i.e. the auto-correlation), the uncertainty of the fit is significantly underestimated and should be estimated based on the number of independent grid-points of the fields (i.e. number of effective degrees of freedom N_{eff}). While there are different approaches to determine N_{eff} in real data (Wang and Shen, 1999), however, the examined highly idealized fields are Fourier filtered which implies that the decorrelation length and the effective sample size are to a high degree imposed by the filter. With the cutoff wavelength R_d depending on f, the effective sample size is given by the number of Fourier coefficients that are considered for the inverse transformation from Fourier- to real space and amounts to $N_{\text{eff}} = 61, 137$ and 241 for f_0, $1.5f_0$ and $2f_0$ respectively (with symmetries in Fourier space as well as real and imaginary parts of complex numbers independently accounted for).

The standard deviation σ of the linear fit is estimated based on regularly resampled (regular grid with $\sqrt{N_{\text{eff}}}$ grid points in x- and y-direction respectively) vorticity and precipitation fields, while the slope of the fit is obtained from the full data set ($N_x \times N_y$). The dependence of the obtained α and σ on the resampling method has been addressed with a bootstrapping method, where N_{eff} points are drawn from a uniform random distribution N-times and the linear fit is applied to the independent samples (not shown). For $N = 1000$ the slope and standard deviation do not show a significant dependence on the location of the underlying sampled points.

In the upper panel of Fig. 4.7 the upper tropospheric vorticity is scattered point-wise with the associated precipitation fields in the right column and a linear functional fit is applied to the data. From the high anti-correlation r smaller than -0.7 for all runs, the spatial coincidence of the fields anticipated from Fig. 4.6 holds in a point-wise sense and for the decorrelated fields. The α-values are given in the upper row of table 4.1. The α-values are not significantly different (i.e. all lie within one-standard-deviation) for f_0, $1.5f_0$ and $2f_0$ and thus do not depend significantly on f, which agrees well with the prediction (4.2) by the analytical model. Note that the reduced uncertainty associated with the estimate of α for higher f values is owed to the respective larger N_{eff}.
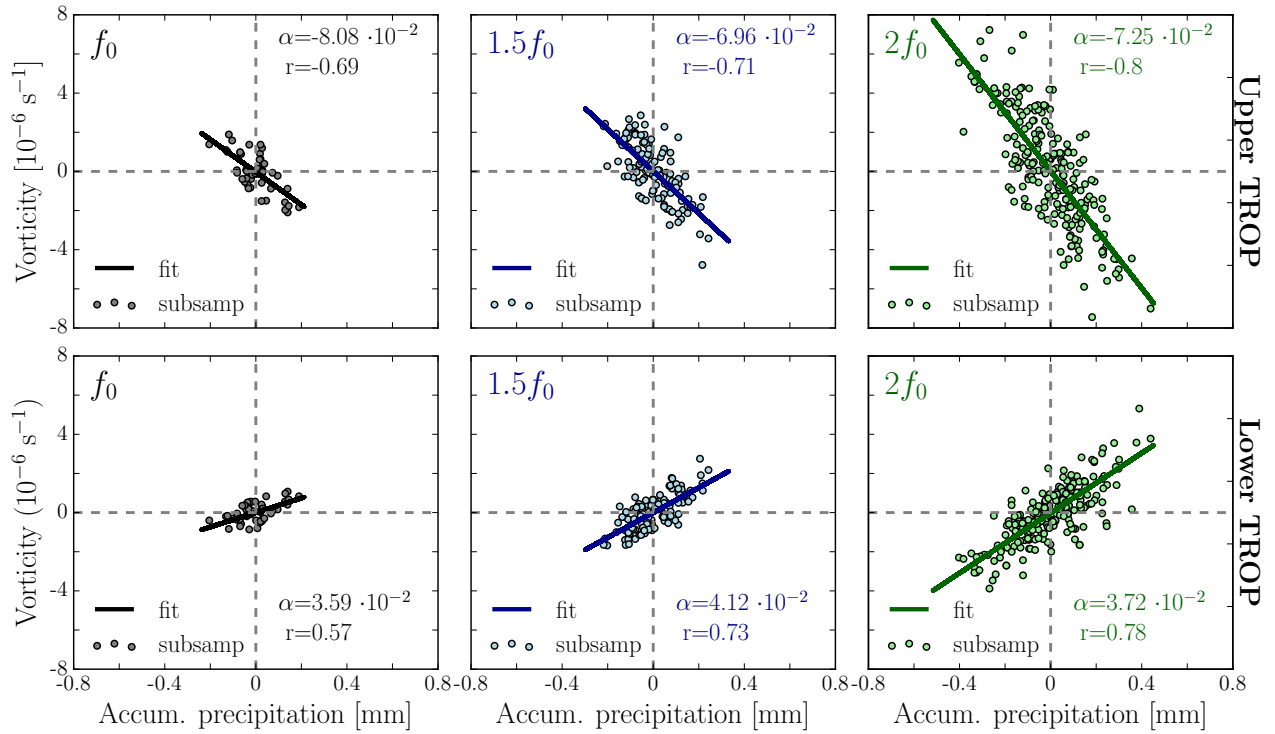
Figure 4.7: Spatially filtered ($\lambda > R_d$) upper tropospheric (i.e. average over four vertical levels between 9.5 and 10.9 km, upper panel) and lower tropospheric (i.e. average over four vertical levels between 2.1 and 0.9 km, lower panel) vorticity and accumulated precipitation rate scattered for f_0, $1.5f_0$ and $2f_0$ (columns from left to right). r denotes the correlation coefficient of the uniformly sampled N_{eff} data points. Solid lines are least-squares fits with slope $\alpha \cdot f$. Standard deviations are given in table 4.1.

Table 4.1: α values (in $\text{m}^2\,\text{kg}^{-1}$) associated with scattered fields in Fig. 4.7 for the upper (Upper TROP) and lower (Lower TROP) troposphere and f_0, $1.5f_0$ and $2f_0$.

	f_0	$1.5f_0$	$2f_0$	
α	$(-8.08 \pm 1.26) \cdot 10^{-2}$	$(-6.96 \pm 0.64) \cdot 10^{-2}$	$(-7.25 \pm 0.38) \cdot 10^{-2}$	Upper Trop
	$(3.59 \pm 0.69) \cdot 10^{-2}$	$(4.12 \pm 0.36) \cdot 10^{-2}$	$(3.72 \pm 0.19) \cdot 10^{-2}$	Lower Trop

Since thus far only one instant has been discussed, the α values estimated from the point-wise scatter of the upper-level vorticity at perturbation lead time t with the accumulated precipitation at $t - t_{GA}$ are shown for ten perturbation lead times in Fig. 4.8 to validate the persistence of the presented results. The solid lines depict α estimated from the three f-runs and the associated hatched areas of the same color indicate the 1σ interval. The α values and the associated uncertainty do not vary significantly (i.e. all lie within one standard-deviation) and are thus not significantly distinct for different f values during the evaluated period.

Equation (4.2) has so far been discussed for upper tropospheric layers where the vorticity anomaly takes its maximum. Owed to the cosine-shape in the vertical, a second maximum of negative sign is expected to occur on lower tropospheric levels. In order to test this prediction, the vorticity field is averaged over four lower tropospheric height levels (between $0.9\,\mathrm{km}$ and $2.1\,\mathrm{km}$) and α and σ are calculated as before (see paragraph 4.4.2). The result is shown in the lower panel of Fig. 4.7. In good agreement with the expectation, the linear relationship obtained for the upper troposphere is reversed, meaning that positive precipitation anomalies lead to positive (i.e. cyclonic) lower-level vorticity anomalies. As before, the correlation between the two fields is high with r-values larger than 0.6 for all runs. The α-values are given in the lower row of table 4.1. As for the upper tropospheric heights, the α-values for f_0, $1.5f_0$ and $2f_0$ are not significantly different (i.e. lie within one standard deviation). This finding also holds for the times shown in Fig. 4.8 (not shown). The hypothesis based on the analytical model, i.e. α is independent of f, is thus also verified for lower tropospheric layers.

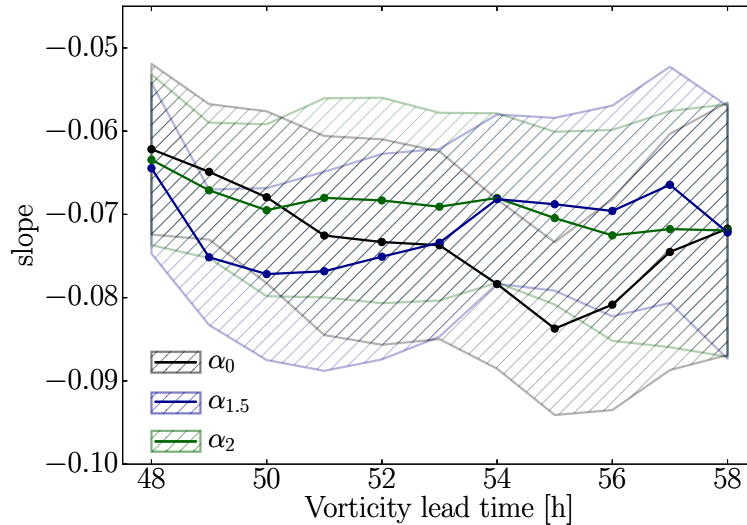**Figure 4.8:** Slope of tropopause height vorticity (average of 4 levels between $9.5\,\mathrm{km}$ and $10.9\,\mathrm{km}$ taken from perturbation lead time t=51-58h and scattered with the accumulated precipitation field at $t - \tau_{GA}$ (see Fig. 4.7).

Quantitative comparison with theoretical value

Second, the order of magnitude estimate of α in (4.2) is quantitatively compared with the values obtained from the linear regression given in table 4.1. With tropospheric values chosen as $T_0 = 250\,\mathrm{K}$, $\rho_0 = 0.7$, $N = 0.01\,\mathrm{s}^{-1}$, $H = 11.5\,\mathrm{km}$ and constants $c_p = 1004\,\mathrm{J\,(kg\,K)}^{-1}$ and $l_v = 2.5 \cdot 10^6\,\mathrm{J\,(kg)}^{-1}$ the order-of magnitude estimate for the upper troposphere and f_0 amounts to $\alpha = 5.21 \cdot 10^{-2}\mathrm{m}^2\,\mathrm{kg}^{-1}$ (with opposite sign in the lower troposphere). While the order of magnitude compares well with the values obtained from the slopes of the regression lines, this value is marginally larger than the obtained upper tropospheric values (with an average of the three upper TROP α-values $\sim -7.43 \cdot 10^{-2}\mathrm{m}^2\,\mathrm{kg}^{-1}$). This is understood to be owed to the fact that (4.2) is based on the Boussinesq-approximation, which implies that the density is assumed constant through the whole considered layer (here the troposphere). If the density was allowed to decrease with height (as in higher order —such as the anelastic— approximations), the upper-level outflow and associated vorticity would be stronger for a given precipitation anomaly than in the in the Boussinesq-approximated counterpart. This results in a larger α value for upper levels. In the lower troposphere this relationship is reversed, meaning that accounting for a decrease of density with height results in a weaker lower level inflow and associated vorticity anomaly for a given precipitation anomaly than in the Boussinesq-approximated counterpart. The averaged lower tropospheric α-values are $\sim 1.42 \cdot 10^{-2}\mathrm{m}^2\,\mathrm{kg}^{-1}$ and thus smaller than the order of magnitude estimate and thus agree well with this understanding. The obtained overestimation of α for upper tropospheric heights compared to the theoretical value (and vice versa) is thus in good agreement with the expected behavior owed to limitations of the Boussinesq-approximation.

4.4.3 f-scaling

The Rossby number (R_O) is defined in SC15 as the ratio between a squared divergence and vorticity norm and reads

$$R_O = \sqrt{\frac{||\delta D||}{||\delta \zeta||}} \quad \text{with} \quad ||\delta D||, ||\delta \zeta|| = \frac{1}{V} \int\limits_V \delta D^2, \delta \zeta^2 \, dV \,, \tag{4.3}$$

where the horizontal divergence δD and the vertical vorticity $\delta \zeta$ are calculated from the horizontal difference wind field ($\delta \boldsymbol{v}_h(x,t) = \boldsymbol{v}_{h,\mathrm{PERT}}(x,t) - \boldsymbol{v}_{h,\mathrm{CTRL}}(x,t)$) and integrated over a volume V that covers 1595 grid-points in each horizontal direction (i.e. 1601 total grid-points minus 6 repeated grid-points of the cyclic horizontal domain) and 18 vertical levels between 3 and 10 km altitude. The vertical range covers the free troposphere and excludes boundary layer effects and is chosen as in SC15 for better comparability. For the Rossby-number the relative contributions of rotational and divergent flow components on different scales are of interest, as opposed to the vorticity diagnostic where solely the large balanced scales were evaluated. The Rossby number is thus calculated for two different scale ranges (i.e. small convective scales S and larger scales L), where a Fourier filter is applied to the difference divergence and vorticity fields and the $S-$ and $L-$scale ranges for the three f-runs are chosen as in section 4.3.

As divergence and vorticity can be interpreted as proxies for unbalanced and balanced motions respectively (see Bühler et al., 2014, and chapter 2), a Rossby number larger than unity (i.e. divergence dominates vorticity) indicates that the underlying wind field is unbalanced. Accordingly, a Rossby number dropping from initially higher values is a sign of an increasing degree of geostrophic balance in the underlying wind field.

The analytical solution for the linear GA problem examined in chapter 3 predicts for space and time scaled with R_d and f respectively a unique shape (i.e. functional form that does not depend on f) for the Rossby number. Note that it was also shown that the amplitude of the balanced vortex as well as the associated divergent circulation depend linearly on f, but this scaling cancels out in the Rossby number which is the ratio between these two quantities.
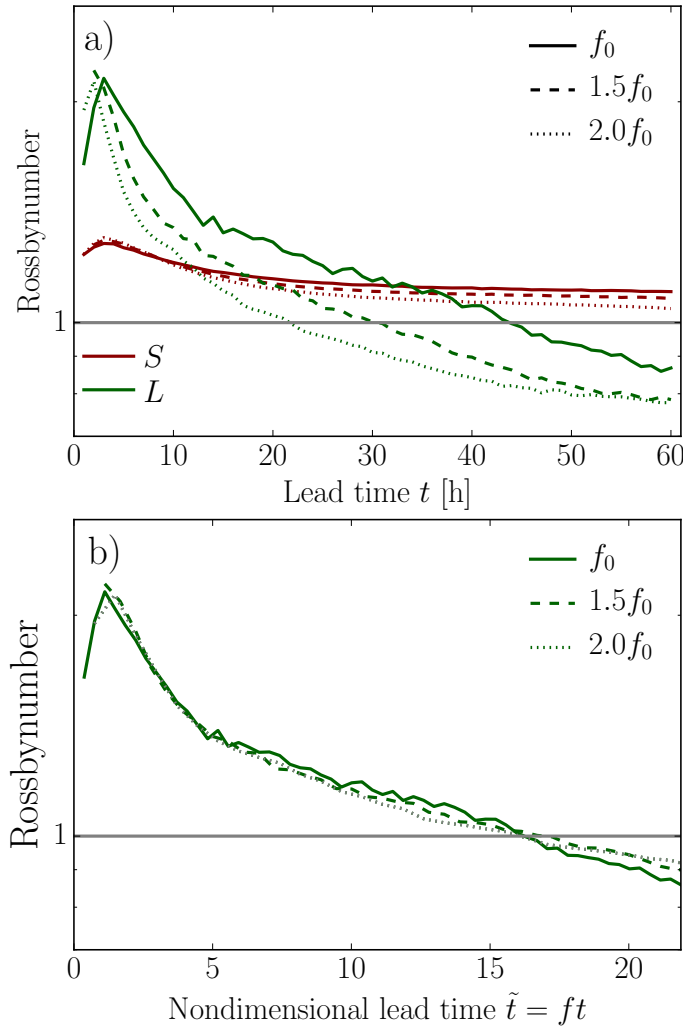
Figure 4.9: Rossby number R_O calculated from $\delta \boldsymbol{v}_h(x,t) = \boldsymbol{v}_{h,\mathrm{PERT}}(x,t) - \boldsymbol{v}_{h,\mathrm{CTRL}}(x,t)$ for the three different f-values. a) R_O as a function of perturbation lead time t, S and L scales. b) R_O as a function of non-dimensional perturbation lead time $\tilde{t} = ft$, solely L scales.

Figure 4.9a displays the Rossby number of the difference wind field for the three different f-values and the scaled S- and L-scales. The small-scale relative flow between two realizations is dominated by convective activity that is not in geostrophic balance. This characteristic is reflected in a Rossby number on the small scales that is initially slightly larger than unity and levels out on a marginally smaller value (i.e. saturation of small scale errors that remain unbalanced throughout the simulation). The small-scale Rossby number shows a negligible dependence on the Coriolis parameter f. This is in good agreement with the finding from paragraph 4.4.1 that in the present numerical setup convective activity acting on scales significantly smaller than R_d is not influenced by the systems rotation rate.

On larger scales, however, there is a significant difference between the temporal evolution of the Rossby number when different rotation rates are imposed: while the curves are initially similar and take a value around 2 (meaning that larger scale dynamics are not balanced at early perturbation lead times), they diverge with increasing perturbation lead time. Note that since the errors are introduced on small-scales, the initial high values of the Rossby-number on the larger scales are most likely attributable to projections from the small-scales due to Fourier filtering (SC15). The decay of the Rossby number with time is, however, associated with an increasing degree of geostrophic balance in the underlying flow field (i.e. the errors) and is shorter for higher rotation rates and vice versa.

Additionally to space scaled with the Rossby Radius of deformation (see Fig. 4.9a), the green curves in Fig. 4.9b depict the larger scale Rossby number for time scaled with f. Evidently, for the employed choice of scaling, the Rossby number for the difference field of the full numerical simulations takes a unique shape (i.e. functional form that does not depend on f). Particularly note that the Rossby number scaling (3.58) in chapter 3 holds for all times in the numerical simulations. The Rossby number in the complex, fully three-dimensional, nonlinear simulation of a convective cloud field scales thus as predicted by the linear analytical model of the GA following convective heating.

4.5   Summary

This chapter aims at closing the gap in complexity in a hierarchy of models (from the analytical calculations in chapter 3 to numerical simulations of realistic weather situations) that aimed at assessing the dynamical process that underlies upscale error growth through the atmospheric mesoscales. Geostrophic adjustment (GA) following convective heating was suggested as a possible dynamical process underlying the transition from small-scale unbalanced to larger-scale balanced errors (Zhang et al., 2007; Selz and Craig, 2015b) but appears difficult to extract from numerical simulations. In chapter 3, the GA of a point-like heat source was examined analytically and three concrete predictions that allow for an identification of the GA mechanism in numerical simulations were proposed where the Coriolis parameter f plays a major role. In the present chapter idealized numerical error growth experiments within a convective cloud field and three different imposed Coriolis parameters are employed to test these predictions. The results are summarized in the following.

First, the analytical model treats the GA mechanism in the highly simplified framework of the linearized, hydrostatic slab- (and radially-) symmetric Boussinesq-equations, where latent heating within a convective cloud is assumed to excite a transient divergent circulation that contains most energy in the hydrostatic deepest tropospheric gravity wave mode. In a numerical simulation that reproduces this dynamical process accurately, features propagating with the associated horizontal phase speed should be clearly identifiable. The horizontal phase speed extracted from the numerical simulations shows a high level of agreement with the analytical value and is furthermore independent of the rotation rate. From these results it is concluded that the transient divergent circulation that is initiated by a convective cloud (i.e. heating) in the fully nonlinear model simulation agrees well with the respective assumption made in the simplified analytical model and indicates that the numerical simulations were successfully designed in a way that the forcing of the mesoscale circulation by convection is independent of f (while the mesoscale circulation itself depends on f).

Second, the analytical study of GA in chapter 3 suggests that the balanced, large-scale vorticity is linearly related to the accumulated divergence (convertible to the precipitation rate) through a proportionality factor. In the numerical simulations, this relationship holds in a point-wise sense and a positive precipitation anomaly generates an anticyclonic (cyclonic) balanced vorticity feature in upper (lower) tropospheric heights. The proportionality factors qualitatively and quantitatively agree well with associated predictions made by linear hydrostatic theory. This results suggest that the GA mechanism might play a role in transitioning errors from small unbalanced to larger balanced scales. Note that, however, in a more realistic numerical simulation with significant surface friction and/or topography, the correlation between the precipitation anomaly and the associated vorticity at lower levels is expected to be worse than the upper tropospheric counterpart due to the more complicated boundary layer effects.

Third, the temporal and spatial coordinates of the analytical solution are shown to naturally scale with the Coriolis parameter f and the Rossby radius of deformation respectively. This choice of scaling renders the shape of the solution and particularly the functional form of the Rossby number universal (i.e. independent of f) in the theoretical GA study. The Rossby number is calculated from the numerical model output with the three rotation rates. Scaling the result according to the prediction by the analytical model shows that the curves collapse onto each other, which indicates that the Rossby number of the difference fields of the presented numerical simulations shows the same behavior as the prediction of the isolated GA process.

The three major results suggest that the diagnostics proposed by the analytical model were successfully applied to identify the GA mechanism in numerical simulations. A discussion of the implications and limitations of the presented results can be found in chapter 5.

Chapter 5

Summary and Discussion

Atmospheric dynamical phenomena associated with diabatic processes experienced as mid-latitudinal weather are attributed to the mesoscales, i.e. typically feature horizontal length scales between a few and a couple of hundred kilometers and time scales of several minutes to one day. Undoubtedly, the skillful prediction on this scale range and the sources of associated uncertainties are a topic of major interest to meteorological research. In spite of their importance to present-day numerical weather prediction, fundamental aspects regarding dominant mesoscale dynamics and scale-interaction processes that govern upscale error growth in the atmosphere remain uncertain. While this thesis can by no means fully solve these open issues, it contributes to an improved understanding of current research questions in two ways: first, a method to decouple mesoscale rotational and divergent modes of motion from aircraft measurements of horizontal wind velocities has been successfully and positively tested in the framework of global numerical model simulations. This method can in the future be applied to atmospheric measurement data and thus potentially provide insights into the dominant dynamics underlying the mesoscale kinetic energy spectrum. Furthermore, indications for the non-universality of mesoscale dynamics and the associated horizontal kinetic energy spectrum were found. Second, geostrophic adjustment following convective heating was identified as a principal dynamical mechanism that effectively propagates errors from small- (significantly divergent) to large (mainly rotational) scales, which intrinsically limits the predictability of atmospheric motion. The relative importance of rotational and divergent modes of motion as well as the nature of their interaction play a major role in identifying the dynamical agent that governs mesoscale dynamics as well as upscale error growth. In the following, the results of these two parts will be summarized and discussed, and possible subsequent studies will be suggested.

Rotational and divergent energy spectra derived from flight-track winds

Bühler et al. (2014) proposed a one-dimensional Helmholtz-decomposition method that allows for the decoupling of rotational and divergent modes from one-dimensional aircraft measurements. Two different implementations of this decomposition method have been applied by Callies et al. (2014) and Lindborg (2015) to aircraft measurement data with different results regarding the relative importance of rotational and divergent modes of motion on the mesoscales. In chapter 2 of this thesis the accuracy of both implementations of the suggested

one-dimensional Helmholtz-decomposition method was tested in the framework of global numerical atmospheric simulations. One-dimensional transects of horizontal velocity fields simulated by the Model for Prediction Across Scales (MPAS) taken along circles of constant latitudes and longitudes served as input to the proposed approaches. The resulting spectra of divergent and rotational kinetic energy were then compared to the respective spectra calculated from two-dimensional fields from MPAS, where the decomposition may be done unambiguously. Furthermore, the variability of the spectra with the examined latitude- and height-ranges was assessed. The results of this chapter have partly been published in Bierdel et al. (2016) and the two major findings are outlined in the following.

First, both suggested implementations of the one-dimensional Helmholtz-decomposition method are very accurate and yield results almost indistinguishable from the correct solution. Particularly on the mesoscales the errors of the proposed methods are small enough that the ratio of divergent to rotational kinetic energy can be estimated accurately. It is thus concluded that, at least when data are aggregated over large areas, the assumptions on the underlying flow of isotropy and homogeneity must be well satisfied. This thesis thus demonstrates that the suggested techniques provide a strong observational check of model- and theoretical results with existing large commercial aircraft data sets.

Second, applications of the proposed methods in foregoing studies have led to contradictory results regarding the dominance of either rotational or divergent modes of motion on the mesoscale range (Callies et al., 2014; Lindborg, 2015). As summarized in the previous paragraph, the two implementations of the one-dimensional Helmholtz-decomposition method were demonstrated to yield practically identical results. It was, however, shown in this thesis that the apparent differences arise from an examination of different latitudinal and height regions of the same data set. The mesoscale divergent kinetic energy was found to generally increase with altitude (see also Koshyk and Hamilton, 2001; Waite and Snyder, 2013; Skamarock et al., 2014; Weyn and Durran, 2017) and an inclusion of lower stratospheric data leads to a significantly stronger divergent kinetic energy component than if only tropospheric data were considered. Regarding the latitudinal region, the mesoscale divergent energy was found to dominate the rotational contribution particularly on the Northern hemisphere as opposed to the Southern hemisphere where the rotational energy is dominant. This finding is in agreement with results found by Nastrom et al. (1984) and Cho et al. (1999), i.e. that atmospheric kinetic energy spectra depend on latitude and if they are taken over ocean or over land. Cho et al. (1999) speculate that orographically-generated gravity waves increase mesoscale spectral variability over land. Since land covers a higher percentage of the area in the Northern hemisphere than in the Southern hemisphere, the results presented are not in disagreement with this hypothesis. In the equatorial region, where the major dynamics are significantly different from the mid-latitudes, the rotational component dominates the whole spectral range. However, the dominance over the divergent component is less pronounced than in the mid-latitudes and the amplitude of the large-scale kinetic energy is comparatively reduced. A corollary is that explanations of the dynamics underlying the mesoscale kinetic energy spectrum may vary between different regions of the atmosphere. Future studies that analyze these dynamics will need to account for such variations.

A detailed examination of the dynamical origin of the mesoscale horizontal kinetic energy spectrum is beyond the scope of this thesis. One major limitation of the examined real-case study is that it merely encompasses 15 days in Northern hemispheric winter and a horizontal grid spacing of 15 km of the employed numerical model. With this data set, the full variability of the kinetic energy spectrum and the rotational and divergent parts can not be assessed. Particularly the impact of deep moist convection on the mesoscale horizontal kinetic energy spectrum can not be determined conclusively for two reasons: first, the energetic contribution of deep moist convection over land in the Northern hemisphere is underrepresented in the selected winter season. Second, deep moist convection is generally not simulated explicitly in the employed numerical model owing to the too coarse horizontal resolution. It is parameterized as a subgrid-scale process and might thus not be accurately represented.

The successful test of the suggested one-dimensional Helmholtz-decomposition method published in Bierdel et al. (2016) has already proven relevant to subsequent research (i.e. cited by Callies et al., 2016; Achatz et al., 2017; Bühler et al., 2017; Sun et al., 2017) and the method was applied to (oceanic) measurement data by Balwada et al. (2016) and Rocha et al. (2016). Furthermore, an explicit wave-vortex decomposition based on the examined Helmholtz-decomposition method has been developed by Bühler et al. (2014, 2017). While the direct evaluation of this second step is not part of the present thesis, the successful application of the Helmholtz-decomposition method to complex atmospheric flow also gives confidence in the applicability of the wave-vortex decomposition, as both methods are partly based on the same mathematical assumptions (Callies et al., 2016). As introduced in paragraph 1.2.2, prevailing theories assessing the meososcale energy spectrum fundamentally differ with regard to a dominance of either rotational or divergent modes of motion. The positively tested one-dimensional Helmholtz-decomposition method should in the future further be applied to atmospheric measurement data such as the well-noted GASP data set (see paragraph 1.2.1). The resulting insights into rotational and divergent contributions to the horizontal kinetic energy spectrum might transform the understanding of mesoscale dynamics.

The *universality* of the mesoscale horizontal kinetic energy spectrum and the associated $k^{-5/3}$ power-law shape is a major paradigm of mesoscale dynamical meteorology (see paragraph 1.2.1). All established theories for the mesoscale horizontal kinetic energy spectrum build on this assumption. In this dissertation, however, the horizontal kinetic energy spectrum and its rotational and divergent constituents were found to depend on the examined geographical region. This result points to non-universal dynamics underlying the mesoscale kinetic energy spectrum and confirms foregoing idealized modeling studies. In there, in particular atmospheric deep moist convection was found to be of crucial importance: the measured atmospheric $k^{-5/3}$-mesoscale kinetic energy spectrum is shown to develop in a flow that lacks large-scale dynamics and is solely energized by small-scale deep moist convection (Sun et al., 2017; Weyn and Durran, 2017). The associated kinetic energy spectrum features a significant divergent contribution and depends sensitively on the atmosphere's moisture content (Waite and Snyder, 2013). Deep moist convection is a process that intimately depends on the state of the surrounding atmosphere determined by the prevailing weather regime and season. The apparent dependence of the mesoscale kinetic energy spectrum on small-scale intermittent processes such as convection suggests that it is sensitive to these details of the examined data set.

While the variability of the mesoscale kinetic energy spectrum and the impact of atmospheric convection clearly warrants further research it has not yet been systematically analyzed.

In a possible follow-up study the variability of the horizontal kinetic energy spectrum and its rotational and divergent constituents could be systematically and quantitatively analyzed. To this end, a more conclusive, high-resolution data set is needed. Simulations such as operational forecasts by the numerical weather prediction model COSMO-DE (Consortium of Small-Scale modeling, Baldauf et al., 2011) that feature a convection-permitting horizontal resolution $\mathcal{O}(1\,\mathrm{km})$ can be analyzed. In order to assess the spectral dependence on the season and prevailing weather regime, the simulations should encompass several years, and summer and winter months. The spectral energy could then quantitatively be associated with parameters such as precipitation, the convective time scale (Keil et al., 2014), the surface pressure or the convective available potential energy (CAPE) in order to systematically assess the regime-dependence.

Together with her colleague Tobias Selz, the author of this thesis has already initiated such a study. First results are shown in Fig. 5.1. The results are preliminary and the evaluated data contains merely three months in summer 2011 and operational COSMO-DE forecasts valid at 15 UTC (for details see caption of Fig. 5.1). The operational COSMO-DE forecasts are routinely provided by the German National Meteorological Service (DWD) and cover a region that contains Germany and also parts of the neighboring countries. The horizontal kinetic energy spectrum (Fig. 5.1a), its spectral slope (Fig. 5.1c) and small-scale amplitude (Fig. 5.1d) are highly variable over the considered time period. Owing to the size of the model domain, the displayed spectra cover scales up to 1000 km. In there, June 22 2011 15 UTC is an extreme event (see red dots in Figs. 5.1c and d). For the shown 15 UTC forecast, the slope of the horizontal kinetic energy spectrum is particularly shallow and the small-scale kinetic energy is exceptionally high. The associated precipitation field displayed in Fig. 5.1b indicates that this day was characterized by intense (partly organized) convective activity. These first results indicate that particularly small-scale kinetic energy correlates well with the precipitation rate. If these results prove to be robust they will show that the mesoscale kinetic energy spectrum is regime-dependent, i.e. sensitive to the current state of the atmosphere (as characterized e.g. by temperature, pressure and precipitation) associated with the examined geographical region and season. This directly opposes the notion of the *universal* atmospheric kinetic energy spectrum introduced in paragraph 1.2.1. In particular, the dependence of the small-scale horizontal kinetic energy spectrum on the precipitation rate hints at the potential of atmospheric deep moist convection to directly energize the mesoscale range. If this hypothesis proves correct, the fundamental inertial-subrange assumption of theoretical studies assessing the mesoscale kinetic energy spectrum is violated (see paragraph 1.2.2). For theories to advance in this field, the dynamics governing the kinetic energy spectrum and its associated variability should be understood first. It will then be possible to assess the resulting kinetic energy spectrum.

Finally, the full variability of the measured kinetic energy spectrum and the rotational and divergent contributions can not be assessed by analyzing data taken by commercial aircraft. In particular regions of active deep moist convection are generally avoided or overflown and thus not contained in the data set. Flight routes are furthermore located on heights between
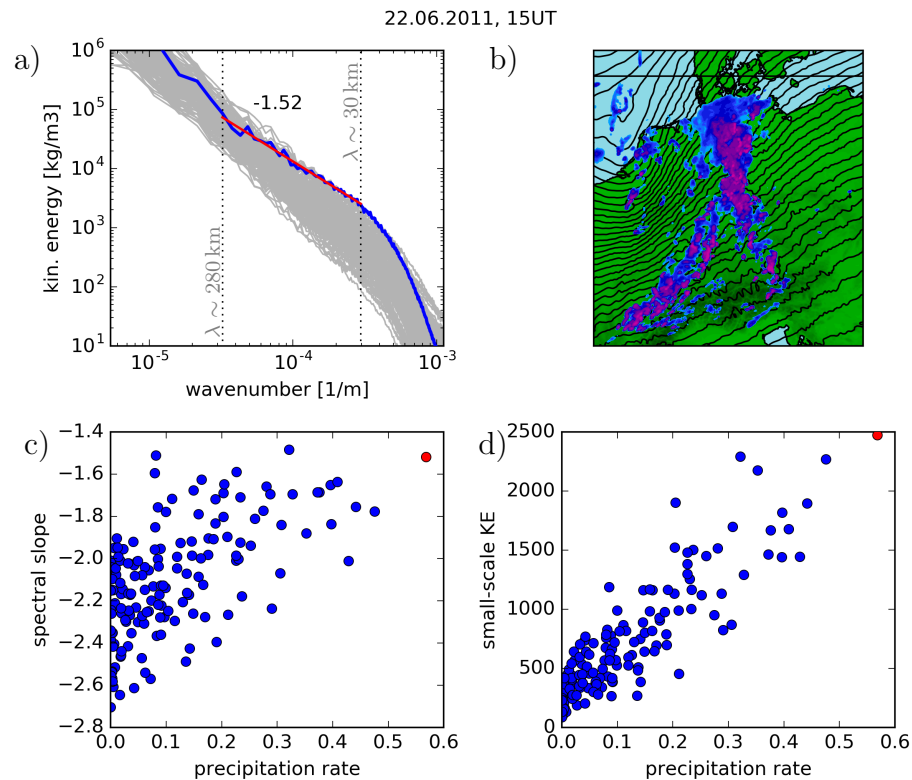
Figure 5.1: a) Upper-tropospheric horizontal kinetic energy spectra of the operational COSMO-DE forecast for 15 UTC initialized at 00 UTC of the same day from May 01 2011 to September 30 2011 as a function of wavenumber in traditional double-logarithmic axes (gray). The spectrum for June 22 2011 15 UTC is highlighted (blue). Least-squares fit to power-law spectrum with coefficient −1.52 between two vertical gray dotted lines is marked in red. b) Precipitation rate on June 22 2011 15 UTC (dark blue and purple colors). Land is displayed in green, ocean in light blue and isolines of the 500 hPa geopotential in steps of $100 \, \mathrm{m^2/s^2}$ (black). c) Spectral slopes estimated as in a) scattered against the precipitation rate. d) Small-scale kinetic energy (i.e. $\lambda \sim 30 \, \mathrm{km}$) scattered against the precipitation rate. In c) and d) values for May 01 2011 to September 30 2011 are displayed in blue and June 22 2011 15 UTC is highlighted in red (courtesy of Tobias Selz).

9 and 12 km and usually clustered in the jet stream region for minimization of fuel consumption. It is thus desirable to apply the suggested one-dimensional Helmholtz-decomposition method to measurements taken by research aircraft (see Callies et al., 2016). One example is aircraft data taken in the course of the NAWDEX (North Atlantic Waveguide and Downstream Impact Experiment) field campaign in autumn 2016 over the North Atlantic Ocean. There, measurement aircraft explicitly targeted regions of particularly strong diabatic modification of the dynamics. For example, one research flight on which the author of this thesis was mission scientist measured the waveguide near the warm conveyor-belt outflow associated with cyclone Vladiana shown in Fig. 1.1. However, attributing mesoscale errors and their variation with scale to the violation of certain underlying assumptions of the one-dimensional Helmholtz-decomposition method is not straightforward and beyond the scope of this thesis. Transects measured in the course of research flights might be shorter, on lower altitudes and

significantly affected by deep moist convection or rising air masses in a warm-conveyor belt. An application of the one-dimensional Helmholtz-decomposition method to this measurement data should thus be preceded by a more extensive evaluation of possible error sources related with the violation of underlying assumptions such as homogeneity.

A general corollary is that a focus of future studies employing numerical models or measurement data as outlined above should focus first on understanding dominant mesoscale dynamics and scale-interactions as well as the associated regime-dependence. These insights can subsequently be used to analyze the mesoscale kinetic energy spectrum and its variability.

Upscale error growth from convection through geostrophic adjustment

The second part of this dissertation addressed the question whether geostrophic adjustment (GA) following atmospheric deep moist convection governs the second stage of the conceptual error growth model by Zhang et al. (2007, see also paragraph 1.3.2). The GA mechanism was exploited in the current thesis with a twofold, analytical and numerical, approach.

First, an analytical model for the GA of an initially localized heating imposed on a quiescent atmosphere was presented in chapter 3. The model is based on the linearized, hydrostatic slab- and radially-symmetric Boussinesq-equations. A solution was found for the buoyancy perturbation arising from a localized pulse heating. The solution has two major advantages over results published in previous studies. First, it contains all transients and balanced flow components in one solution as opposed to solving for both components separately by using potential vorticity conservation (Gill, 1982; Schubert et al., 1980). Second, it provides the solution for the buoyancy response of a rotating atmosphere to a Delta-function forcing in space and time. The solution to this forcing is the Green's function for the mathematical problem. It allows for the simple construction of a solution for arbitrary forcings by linear superposition. From the buoyancy solution, spatial and temporal scaling characteristics are derived. Furthermore, three diagnostics that may help to identify the GA mechanism in numerical simulations were suggested. In there, the Coriolis parameter plays a major role. The diagnostics are:

1. The analytical model predicts gravity waves with phase speeds that are independent of f and inversely proportional to the vertical mode m of the forcing. In agreement with previous studies it is assumed that the convection projects mainly onto the gravest vertical mode ($m = 1$), which results in a phase speed of the waves of $c_1 = NH$.

2. A linear relationship is predicted by the analytical model between the rate of change of the balanced, large-scale vorticity and the (time-lagged) latent heating. For an evaluation of this relationship the precipitation can be used as a proxy for the latent heating.

3. When neglecting the transients the response to the heat source evolves over time from purely divergent to purely rotational. The timescale of this transition is proportional to f^{-1}. The ratio of divergence over vorticity (Rossby number) can be extracted from numerical simulations and the f-dependence of its evolution can be tested.

Linearity is one major assumption which underlies the calculation presented in chapter 3 and implies that the amplitude of the flow that is generated by the heat sources remains small. The linear and also the hydrostatic assumptions are clearly violated within the convective clouds themselves. However, heating by convective clouds typically generates small amplitude flow responses implying that linearity is expected to hold for the wave response and for the secondary circulation excited by the heating (Nicholls et al., 1991; Schubert et al., 1980). Nonlinear effects (Raymond, 1987) can nevertheless become relevant for very large heating rates, leading to a large amplitude of the transient response (Chagnon and Bannon, 2005a). This effect is a known problem in convective-scale data assimilation where spurious convective cells are generated non-linearly by waves excited by a local perturbation of the model state (Lange et al., 2017). If the linearity assumption holds, however, the predictions of the analytical model can be applied to single convective clouds as well as to a field of convective clouds by linear superposition. In addition they can be applied to difference fields between two simulations in the context of an error growth study.

In chapter 4 the predictions based on the analytical model were compared with complex, fully nonlinear COSMO model simulations of a convective cloud field in a rotating environment. In order to test the suggested scaling with the Coriolis parameter and the established diagnostics, three control-simulations with different close-to planetary rotation rates were performed. For each of the simulations a slightly perturbed twin experiment was conducted and the error growth was examined in the difference field (between a control and perturbed simulation). The numerical experiments were carefully designed such that possible issues concerning the comparability between the highly idealized analytical calculation (i.e. linear, hydrostatic theory in the framework of Boussinesq-equations) and complex, fully nonlinear model simulations were avoided. This has been achieved by neglecting large scale flow and topography, and choosing the imposed Coriolis parameters such that differences in the upscale error growth were apparent while the small-scale convective activity remained unchanged. In this idealized numerical setting, three major results suggest that the diagnostics following from the analytical model were successfully applied to identify the GA mechanism in numerical simulations. First, the gravest gravity wave mode with a f-independent horizontal phase speed could be detected. Second, the proportionality factors between the balanced, large-scale vorticity and the accumulated precipitation agreed qualitatively and quantitatively well with associated predictions. Third, scaling the Rossby number according to the prediction based on the analytical model showed the expected f-dependence. Note that particularly in the second diagnostic any advection with the background flow was neglected. While in the idealized study the initial wind field could simply be set to zero, this limitation can be mitigated in more realistic numerical simulations by considering a Lagrangian reference frame. These results show that the diagnostics derived from the analytical model were successfully applied to identify the GA mechanism in numerical simulations.

Based on the results presented in chapters 3 and 4 the arising image for upscale error growth from precipitating regions is the following: small-scale error growth is understood to be saturated (i.e. end of stage 1) when all individual convective cells are displaced. The difference field is then an ensemble of massflux-dipoles with varying amplitude. Every cloud in the difference field initiates a gravity wave response, which propagates dominantly with the speed of the

gravest hydrostatic gravity wave mode in mid-tropospheric levels. The divergent upper-level outflow and convergent lower-level inflow then set up a balanced rotational flow while undergoing GA. The characteristic time- and length-scales of the arising vortices is proportional to the inverse Coriolis parameter f^{-1} and the Rossby radius of deformation R_d (see schematic in Fig. 1.3). The GA process might thus link the convective (stage 1) to the baroclinic (stage 3) error growth of the conceptual model suggested by Zhang et al. (2007).

In paragraph 1.3.2 the two prevailing viewpoints on atmospheric predictability, i.e. the turbulent cascade (Lorenz, 1969) and the three-stage approach (Zhang et al., 2007) were introduced. While the three-stage error growth model has been investigated in this thesis, one aspect that allows for the distinction between the suggested GA-hypothesis and the turbulent cascade theory is the scaling of the characteristic time-scale of upscale error growth with the Coriolis parameter f. According to the GA-framework, the time of the appearance of large-scale balanced errors is linearly inversely proportional to f, i.e. $t_{GA} \sim f^{-1}$ (see (3.40)). In the standard local cascade hypothesis introduced in paragraph 1.3.2 the predictability time T_p is the integral of the eddy turnover time τ_k over the given scale range (Lilly, 1972). For a background kinetic energy spectrum with a powerlaw-dependence $E_K(k) \sim k^{-\beta}$ it follows from (1.5) that $T_p \sim (k_L - k_S)^{(\beta-3)/2}$. For the large-scale being the Rossby radius of deformation R_d (see (3.38)) the large-scale wavenumber is given by $k_L = 2\pi f/(NH)$. If k_S is either equally scaled with R_d or constant (implying that the scale of the forcing by convective heating does not depend on f), the predictability time reads

$$T_p \sim f^{(\beta-3)/2} \,. \tag{5.1}$$

In this cascade picture, the predictability time is—for β not equal to unity—different from the geostrophic adjustment timescale $t_{GA} \sim f^{-1}$. In the present idealized numerical simulations the horizontal background kinetic energy spectrum features a f-independent slope that takes the approximate value $\beta \sim 1.4$ (see Fig. 4.3). It is thus fairly steeper than the mesoscale $\beta \sim 1.67\,(= 5/3)$ slope that follows from measurement data (Nastrom et al., 1984). The arising $f^{-0.8}$-scaling of the predictability time contradicts the f^{-1}-scaling of the GA hypothesis. Note that this simple calculation of upscale growth neglects up-amplitude growth that might have to be considered for completeness. For a more accurate comparison of the cascade- and geostrophic adjustment hypotheses as possibly determining the predictability time the spectral slope should furthermore be estimated with an accurate mathematical approach (Clauset et al., 2009; Stumpf et al., 2012). However, while the difference between the two scalings ($f^{-0.8}$ and f^{-1}) appears small, it is large enough for the $f^{-0.8}$ scaling to depart significantly from the linear f-scaling of the Rossby number shown in Fig. 4.9. This indicates that the dynamical process that governs error growth in the numerical simulations described in chapter 4 may not be associated with a turbulent cascade.

In this dissertation the growth of small-scale, small-amplitude initial errors through the GA process and thus the intrinsic predictability problem was assessed (Melhauser and Zhang, 2012; Sun and Zhang, 2016). Thus, the results presented in chapters 3 and 4 particularly do not account for a potential downscale impact of large-scale errors that might pose a practical limit to the predictability of atmospheric flow in certain weather regimes (Durran et al., 2013; Durran and Gingrich, 2014). The results presented in this thesis are, however, not limited to

the intrinsic predictability case where errors grow in the first stage from infinitesimally small initial amplitude and scale. The suggested mechanism underlying upscale error growth in the second stage is rather generally applicable and practically relevant to numerical simulations where the latent heat release within convective clouds is a small-scale source of uncertainty (Zhang et al., 2007; Selz and Craig, 2015b).

In a real-case study of an European forecast bust, Rodwell et al. (2013) identified the accurate representation of mesoscale convective systems (over North America) and associated subgrid-scale structures as crucial to the skillful numerical weather prediction over Europe. In Rodwell et al. (2013), the impact of latent heating within convective clouds that are not or only partly resolved is found to grow upscale due to a significant diabatic modification of the upper level Rossby wave train. In atmospheric numerical models subgrid-scale processes are parameterized. This signifies that they are not explicitly resolved by the model's grid-resolution and are represented in the model by a simplified process. Convective-scale variability in numerical models that feature a too coarse spatial resolution to explicitly resolve convection can be accounted for by employing stochastic subgrid-scale parameterizations. In there, a random component is introduced into the modeling system on unresolved scales. Selz and Craig (2015a) find that the correct representation of the variability associated with convective clouds and the subsequent upscale propagation are crucially important to a correct estimate of the large-scale variability (e.g. reflected by an increased reliability of an ensemble prediction system (EPS)). This dissertation provides dynamically motivated insights into the upscale impact of convective heating on explicitly resolved or unresolved scales. It thus may particularly contribute to improving current subgrid-scale parameterizations and their impact on the resolved parts of the flow. An example will be given in the following.

Widely used stochastic physical parameterizations such as kinetic energy backscatter schemes (SKEBs, Shutts, 2005) and perturbed parameterization tendencies (Buizza et al., 1999) are designed in an ad-hoc manner to improve the spread of operational EPS. Recently, Shutts (2015) suggested a dynamically motivated modified SKEBs (i.e. Stochastic Convective Backscatter, SCB), where the only source of random model error accounted for is deep convection. In there, every convective grid point instantaneously forces a near-grid scale concentric divergence and vorticity response which is solely driven by the mass-flux profiles provided by the convective parameterization. The SCB scheme is shown to produce a similar spread as the operationally used, less dynamically motivated combination of SKEBs and perturbed parameterization tendencies. Details of the physical response in the SCB scheme, particularly the outer spectral smoothing- or adjustment scale and the time scale of the response, are currently not based on a theoretical model. The current thesis may help to improve such stochastic parameterizations by contributing to a more profound dynamical understanding of the upscale growth of convective-scale uncertainty. It particularly provides a dynamical reasoning for the time- and length scales involved in the SCB scheme.

Finally, the three stage-error growth model suggested by Zhang et al. (2007) is highly conceptual in nature and the analytical description presented in chapter 3 assesses merely the transitional stage of this model in a simplified mathematical framework. As a follow-up study, a quantitative and more comprehensive mathematical framework for the three-stage error growth model might be formulated on the basis of *multiscale asymptotics* (Klein, 2009;

Achatz et al., 2017). In this framework, subsets of the full equations that govern atmospheric flow are derived for the small-, meso- and large-scales by an identification of dominant dynamics through a scale analysis. Atmospheric error growth from small- to large scales can then be assessed in a mathematically more rigorous manner by solving a hierarchy of sets of equations. The solution to a set of equations serves as a forcing to the larger-scale dynamics and scale-interaction coefficients will be accounted for explicitly. The author of this thesis plans to conduct an according study in the course of a PostDoc project in the framework of the *Waves to Weather* (W2W) Transregional Collaborative Research Center.

Appendix A

Detailed dimensional calculation: Geostrophic adjustment of a point-like buoyancy forcing in slab-symmetric geometry

In this chapter of the appendix an extended and dimensional version of the analytical model presented in chapter 3 is given. This chapter might thus be particularly insightful for students or a reader who intends to perform an analogous calculation. Note that while this chapter is part of the appendix, the notation might differ slightly from the notation employed in the rest of the thesis. However, all symbols used in this chapter are introduced.

In the following simple analytical model the response of a horizontally unbounded, rotating atmosphere to a slab-symmetric buoyancy source ('cloud') of zero width is examined. From the obtained buoyancy solution the pressure and geostrophic wind will be derived. The starting point are the linearized, hydrostatic, inviscid, rotating Boussinesq-equations (see for example Vallis (2006, p. 99) or Gill (1982, p. 256)) [with a reference density $\rho_0 = 1\,\mathrm{kg\,m^{-3}}$]. The slab-symmetric, rotating equations read

$$\partial_t u'(x,z,t) - f_0 v'(x,z,t) = -\partial_x \pi'(x,z,t) \tag{A.1}$$

$$\partial_t v'(x,z,t) + f_0 u'(x,z,t) = 0 \tag{A.2}$$

$$-\partial_z \pi'(x,z,t) + b'(x,z,t) = 0 \tag{A.3}$$

$$\partial_x u'(x,z,t) + \partial_z w'(x,z,t) = 0 \tag{A.4}$$

$$\partial_t b'(x,z,t) + N^2 w'(x,z,t) = Q(x,z,t), \tag{A.5}$$

where $\boldsymbol{v}'(x,z,t) = (u',v',w')$ is the three-dimensional perturbation wind vector with components u', v' and w', $\pi' = p'/\rho_0$ is the scaled pressure perturbation, $b' = -g\rho'/\rho_0$ is the perturbation buoyancy and f_0 denotes the Coriolis parameter. The " ' " denotes a perturbation from a reference field at $t=0$ (according to the decomposition $\psi(t) = \bar{\psi} + \psi'(t)$). Since the considered initial state is a quiescent atmosphere the prime is dropped for convenience. $N^2 = -g/\rho_0 d_z \rho_0$ is the Brunt-Väisälä frequency and

$$Q = Q_0 \delta(x)\delta(t)\sin(mz) \tag{A.6}$$

is the buoyancy source. $\delta(\xi)$ denotes the Dirac-delta function with

$$\int_a^b \delta(\xi)\, d\xi = \begin{cases} 1, & \text{if } 0 \in [a,b], \\ 0, & \text{otherwise.} \end{cases}$$

The forcing Q is thus turned on and off 'instantaneously' at time $t = 0$, located at $x = 0$ and its vertical structure follows a sine wave with wavenumber $m = n\pi/H$ (with the tropopause height H) (see Nicholls et al. (1991) and Fig. A.1).
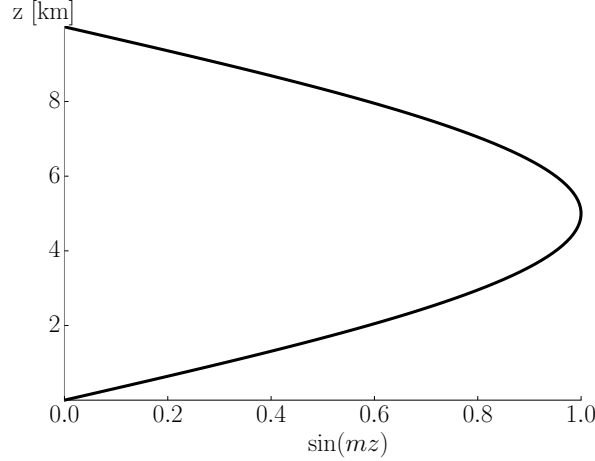

Figure A.1: The vertical structure of the heating $Q = Q_0\delta(x)\delta(t)\sin(mz)$ with $m = \pi/H$.

The partial differential equation (PDE) for the buoyancy perturbation $b = b(x, z, t)$ is obtained by the following calculation, where two equations relating w and b are derived and then w is eliminated:

$$\partial_x\partial_z(\text{A.1}):\ \partial_t\partial_z\partial_x u - f_0\partial_x\partial_z v = -\partial_x^2\partial_z\pi \overset{(\text{A.3})}{=} -\partial_x^2 b'$$
$$\text{with (A.4)}:\ -\partial_t\partial_z^2 w - f_0\partial_x\partial_z v = -\partial_x^2 b$$
$$\partial_t\ :\ -\partial_t^2\partial_z^2 w - f_0\partial_x\partial_z\partial_t v = -\partial_t\partial_x^2 b \tag{A.7}$$

In order to eliminate v the associated momentum equation is used:

$$\partial_x\partial_z(\text{A.2}):\ \partial_t\partial_z\partial_x v = -f_0\partial_x\partial_z u\,.$$

It thus follows for (A.7)

$$-\partial_t^2\partial_z^2 w + f_0^2\partial_z\underbrace{\partial_x u}_{-\partial_z w} = -\partial_t\partial_x^2 b$$
$$-\partial_t^2\partial_z^2 w - f_0^2\partial_z^2 w = -\partial_t\partial_x^2 b\,. \tag{A.8}$$

The second equation relating b and w is derived as follows:

$$\partial_t^2\partial_z^2(\text{A.5}):\ \partial_t^3\partial_z^2 b + N^2\partial_t^2\partial_z^2 w = \partial_t^2\partial_z^2 Q$$
$$\Rightarrow\ \partial_t^2\partial_z^2 w = N^{-2}[\partial_t^2\partial_z^2 Q - \partial_t^3\partial_z^2 b] \tag{A.9}$$
$$\text{and}\quad \partial_z^2 w = N^{-2}[\partial_z^2 Q - \partial_t\partial_z^2 b]\,. \tag{A.10}$$

With (A.9) and (A.10) it follows for (A.8):

$$-N^{-2}[\partial_t^2\partial_z^2 Q - \partial_t^3\partial_z^2 b] - f_0^2 N^{-2}[\partial_z^2 Q - \partial_t\partial_z^2 b] = -\partial_t\partial_x^2 b$$
$$\Rightarrow \partial_t^3\partial_z^2 b - \partial_t^2\partial_z^2 Q - f_0^2\partial_z^2 Q + f_0^2\partial_t\partial_z^2 b = -N^2\partial_t\partial_x^2 b$$
$$\partial_t^3\partial_z^2 b + f_0^2\partial_t\partial_z^2 b + N^2\partial_t\partial_x^2 b = \partial_t^2\partial_z^2 Q + f_0^2\partial_z^2 Q \,. \tag{A.11}$$

The z-dependence can be separated out by expansion in eigenfunctions of ∂_z^2:

$$\partial_z^2 \boldsymbol{e}_i(z) = -\lambda^2 \boldsymbol{e}_i(z) \text{ with } \boldsymbol{e}_i(z) = \sin\left(i\frac{\pi}{H}z\right) = \sin(m_i z)$$

The expansion reads

$$b(x,z,t) = \sum_i B_i(x,t)\boldsymbol{e}_i(z) = \sum_i B_i(x,t)\sin(m_i z)$$

and in the following only a forcing which corresponds to an integer-wavenumber $i = 1$, i.e. $m = m_1 = \pi/H$, $B(x,t) = B_1(x,t)$ is going to be considered.
The PDE for the amplitude $B(x,t)$ with $b'(x,z,t) = B(x,t)\sin(mz)$ then reads

$$\partial_t^3 B(x,t) + f_0^2\partial_t B(x,t) - c^2\partial_t\partial_x^2 B(x,t) = Q_0\delta(x)\partial_t^2\delta(t) + f_0^2 Q_0\delta(x)\delta(t)\,, \tag{A.12}$$

where $c = N/m$ denotes the spreading ('gravity wave') velocity of the disturbance.
The Laplace transform

$$\mathcal{L}\{f(t)\} = F(s) = \int_{0^-}^{\infty} f(t)\exp(-st)\,dt, \quad s \in \mathbb{C} \tag{A.13}$$

is applied to (A.12) and it follows

$$\underbrace{\int_{0^-}^{\infty}\partial_t^3 B(x,t)\exp(-st)\,dt}_{\text{I}} + f_0^2\underbrace{\int_{0^-}^{\infty}\partial_t B(x,t)\exp(-st)\,dt}_{\text{II}} - c^2\partial_x^2\underbrace{\int_{0^-}^{\infty}\partial_t\ B(x,t)\exp(-st)\,dt}_{\text{III}} \tag{A.14}$$

$$= Q_0\delta(x)\underbrace{\int_{0^-}^{\infty}\partial_t^2\delta(t)\exp(-st)\,dt}_{\text{IV}} + f_0^2 Q_0\delta(x)\underbrace{\int_{0^-}^{\infty}\delta(t)\exp(-st)\,dt}_{\text{V}}$$

$$\tag{A.15}$$

For the evaluation of terms $I - V$ the following two identities are employed: The Laplace transform of the $n-$th order temporal derivatives of a function $f(t)$ (I. N. Bronstein and Mühlig, 2001, p. 735)

$$\mathcal{L}\{\partial_t^{(n)} f(t)\} = s^n\mathcal{L}\{f(t)\} - s^{n-1}f(0^-) - s^{n-2}\partial_t f(t)|_{0^-} - \ldots - s\partial_t^{(n-2)} f(t)|_{0^-} - \partial_t^{(n-1)} f(t)|_{0^-}$$

$$= s^n\mathcal{L}\{f(t)\} - \sum_{k=1}^{n} s^{k-1}\,\partial_t^{n-k} f(t)\big|_{0^-} \tag{A.16}$$

and the Laplace transform of the Dirac-delta function

$$\int_{0^-}^{\infty} \delta(t) \exp(-st)\, dt = 1\,. \tag{A.17}$$

With (A.16) and (A.17) it follows for the terms given in (A.14)

$$
\begin{aligned}
\text{I}: \quad & s^3 \beta(x,s) \underbrace{-\partial_t^2 B(x,t)|_{t\to 0^-} - s\partial_t B(x,t)|_{t\to 0^-} - s^2 B(x,t)|_{t\to 0^-}}_{=0} \\
\text{II and III}: \quad & s\beta(x,s) \underbrace{-B(x,t)|_{t\to 0^-}}_{=0} \\
\text{IV}: \quad & s^2 \underbrace{-\partial_t \delta(t)|_{t\to 0^-} - s\delta(t)|_{t\to 0^-}}_{=0} \\
\text{V}: \quad & 1\,.
\end{aligned}
$$

It thus follows for the Laplace-transformed PDE with $\beta(x,s) = \mathcal{L}\{B(x,t)\}$:

$$
\begin{aligned}
s^3 \beta(x,s) + f_0^2 s \beta(r,s) - c^2 s \partial_x^2 \beta(x,s) &= Q_0 \delta(x)(s^2 + f_0^2) \\
\partial_x^2 \beta(x,s) - \frac{1}{c^2}(s^2 + f_0^2)\beta(x,s) &= -\frac{Q_0 \delta(x)}{c^2}(s + f_0^2 s^{-1})\,.
\end{aligned} \tag{A.18}
$$

The desired solution vanishes for $x \to \infty$ owing to

$$
\begin{aligned}
\lim_{x\to\infty} \beta(x,s) = \lim_{x\to\infty} & \left| \int_{0\to\infty} B(x,t)\exp(-st)\, dt \right| \\
= \lim_{x\to\infty} & \left[\underbrace{\int_0^{x/c} B(x,t)\exp(-st)\, dt}_{=0} + \int_{x/c}^{\infty} B(x,t)\exp(-st)\, dt \right]\,,
\end{aligned}
$$

where the triangle inequality gives

$$
\begin{aligned}
\lim_{x\to\infty} \beta(x,s) &\le \lim_{x\to\infty} \int_{x/c}^{\infty} |B(x,t)|\,|\exp(-st)|\, dt \\
&\le \lim_{x\to\infty} \max(B(x,t)) \int_{x/c}^{\infty} |\exp(-st)|\, dt
\end{aligned}
$$

and thus

$$
\lim_{x\to\infty} \max(B(x,t)) \int_{x/c}^{\infty} |\exp(-st)|\, dt \le \lim_{x\to\infty} \max(B(x,t)) \int_{x/c}^{\infty} \exp(-st) \underbrace{|\cos(bt) - i\sin(bt)|}_{=2}\, dt
$$

$$
= \lim_{x\to\infty} 2\max(B(x,t)) \int_{x/c}^{\infty} \exp(-st)\, dt
$$

$$
= \lim_{x\to\infty} 2\max(B(x,t))[-s^{-1}\exp(-st)]_{t=x/c}^{t\to\infty}
$$

$$
= \lim_{x\to\infty} 2\max(B(x,t))s^{-1}\exp(-sx/c) = 0\,,
$$

where a and b denote the real and imaginary parts of s respectively.

Since the desired solution vanishes for $x \to \infty$ and interest lies on the response outside of the source region ($x \neq 0$), the in x-symmetric solution

$$
\beta(x,s) = B(s)\exp\left(-\frac{1}{c}\sqrt{s^2 + f_0^2}\,|x|\right) \tag{A.19}
$$

is guessed for the homogeneous equation.

Since the second derivative of $\beta(x,s)$ is proportional to $\delta(x)$, the solution has a kink at $x = 0$ (first derivative is $\mathsf{H}(x)$). For $\beta(x,s)$ it holds

$$
\beta(x,s) = B(s) \cdot \begin{cases} \exp(-\vartheta(s)x), & x > 0 \\ \exp(\ \vartheta(s)x), & x < 0\,, \end{cases} \tag{A.20}
$$

where $\vartheta(s) = c^{-1}\sqrt{s^2 + f_0^2}$ has been used for simplification.
Formally, (A.18) is treated as a homogeneous equation and the inhomogeneity as a boundary condition defining the strength of the kink $B(s)$. In order to find an expression for $B(s)$, the PDE (A.18) is integrated from $-x$ to x and then the limit $x \to 0$ is taken:

$$
\lim_{x\to0} \int_{-x}^{x} \partial_x^2 \beta(x',s)\, dx' - \vartheta(s)^2 \lim_{x\to0} \int_{-x}^{x} \beta(x',s)\, dx' = \xi(s) \lim_{x\to0} \underbrace{\int_{-x}^{x} \delta(x')\, dx'}_{=1}
$$

$$
\text{for } \beta(x,s) \text{ bounded: } \lim_{x\to0} \int_{-x}^{x} \beta(x',s)\, dx' = 0
$$

$$
\Rightarrow \lim_{x\to0}[\partial_x\beta(x',s)]_{x'=-x}^{x'=x} = \xi(s)\,, \tag{A.21}
$$

where $\xi(s) = -Q_0 c^{-2}(s + f_0^2 s^{-1})$ has been introduced for simplification. The left hand side of (A.21) can be directly evaluated using (A.20) and with

$$
\partial_x\beta(x,s) = B(s)\vartheta(s) \cdot \begin{cases} -\exp(-\vartheta(s)x), & x > 0 \\ \exp(\ \vartheta(s)x), & x < 0 \end{cases} = B(s)\vartheta(s)\exp(-\vartheta(s)|x|) \cdot \begin{cases} -1, & x > 0 \\ 1, & x < 0\,, \end{cases}
$$

it follows

$$\lim_{x\to 0}[\partial_x\beta(x',s)]_{x'=-x}^{x'=x} = \lim_{x\to 0}\left\{-B(s)\vartheta(s)\exp(-\vartheta(s)x) - B(s)\vartheta(s)\exp(\vartheta(s)x)\right\} \tag{A.22}$$
$$= -2B(s)\vartheta(s)\,. \tag{A.23}$$

With (A.21) it thus follows

$$B(s) = -\frac{1}{2}\frac{\xi(s)}{\vartheta(s)}$$

and the solution for $\beta(x,s)$ takes the form

$$\beta(x,s) = -\frac{1}{2}\frac{\xi(s)}{\vartheta(s)}\exp\left(-\vartheta(s)\,|x|\right) \tag{A.24}$$
$$\text{with}\qquad \xi(s) = -Q_0 c^{-2}(s + f_0^2 s^{-1})$$
$$\text{and}\qquad \vartheta(s) = c^{-1}\sqrt{s^2 + f_0^2}\,.$$

This formula can also be written as

$$\beta(x,s) = \frac{Q_0}{2c}\left[sf(x,s) + f_0^2 s^{-1} f(x,s)\right]$$
$$\text{with}\quad f(x,s) = \frac{1}{\sqrt{s^2 + f_0^2}}\exp\left(-(|x|c^{-1})\sqrt{s^2 + f_0^2}\right)\,.$$

From the linearity property of the Laplace transform, $f(s) = Af_1(s) + Bf_2(s)$ and $F(t) = AF_1(t) + BF_2(t)$ (Abramowitz and Stegun, 1964, formula 29.2.3), it follows

$$B(x,t) = \mathcal{L}^{-1}\left\{\beta(x,s)\right\} = \frac{Q_0}{2c}\left[\mathcal{L}^{-1}\left\{sf(x,s)\right\} + f_0^2\mathcal{L}^{-1}\left\{s^{-1}f(x,s)\right\}\right)\right]\,. \tag{A.25}$$

With the differentiation and integration rules involving Laplace transforms (Abramowitz and Stegun, 1964, formulas 29.2.4 and 29.2.6) it holds

$$g(s) = sf(s) - F(t)|_0 \qquad\qquad\qquad G(t) = \partial_t F(t) \tag{A.26}$$

$$g(s) = \frac{1}{s}f(s) \qquad\qquad\qquad G(t) = \int_0^t \mathcal{L}^{-1}\{f(s)\}\,d\tau\,. \tag{A.27}$$

While inverse Laplace transforms can generally be obtained by a contour-integration around branch cuts in the complex plane, they might also be found in lookup-tables. The latter applies to the current function $f(x,s)$, where the inverse Laplace-transform is according to Abramowitz and Stegun (1964, formula 29.3.92) given by

$$F(x,t) = \mathcal{L}^{-1}\{f(x,s)\} = \mathcal{J}_0(f_0\sqrt{t^2 - (|x|/c)^2})\mathsf{H}(t - (|x|/c)\,, \tag{A.28}$$

where $\mathcal{J}_0(\cdots)$ denotes the Bessel function of first kind and order zero.
With $F(x,t)|_0 = 0$ it follows

$$\mathcal{L}^{-1}\left\{sf(x,s)\right\} = \mathcal{L}^{-1}\left\{sf(x,s) - F(x,t)|_0\right\} = \partial_t F(x,t)\,. \tag{A.29}$$

With the integration rule it follows

$$\mathcal{L}^{-1}\left\{s^{-1}f(x,t)\right\} = \int_0^t F(x,\tau)\,d\tau \tag{A.30}$$

and with (A.29) and (A.30) equation (A.25) becomes

$$B(x,t) = \frac{Q_0}{2c}\left[\partial_t F(x,t) + f_0^2 \int_0^t F(x,\tau)\,d\tau\right].$$

With $F(x,t)$ from (A.28) it follows for the full buoyancy solution $b(x,z,t) = B(x,t)\sin(mz)$

$$b(x,z,t) = \frac{Q_0}{2c}\left[\partial_t F(x,t) + f_0^2 \int_0^t F(x,\tau)\,d\tau\right]\sin(mz)$$

$$= \frac{Q_0}{2c}\left[-\frac{f_0\,t}{g(x,t)}\mathcal{J}_1(\cdots)\mathsf{H}(\cdots) + \mathcal{J}_0(\cdots)\delta(\cdots)\right.$$

$$\left. + f_0^2 \int_0^t \mathcal{J}_0(f_0 g(x,\tau))\mathsf{H}(\tau - |x|/c)\,d\tau\right]\sin(mz), \tag{A.31}$$

where the abbreviations

$$g(x,t) = \sqrt{t^2 - (|x|/c)^2}$$
$$\mathcal{J}_\psi(\cdots) = \mathcal{J}_\psi(f_0 g(x,t))$$
$$\mathsf{H}(\cdots) = \mathsf{H}(t - |x|/c)$$
$$\delta(\cdots) = \delta(t - |x|/c)$$

have been used.
With the hydrostatic equation (A.3) the perturbation pressure reads

$$\pi(x,z,t) = \int_0^z b(x,z',t)\,dz'$$

$$= \frac{Q_0}{2c}\left[\partial_t F(x,t) + f_0^2 \int_0^t F(x,\tau)\,d\tau\right]\int_0^z \sin(mz')dz'$$

$$= \frac{Q_0}{2c}\left[-\frac{f_0\,t}{g(x,t)}\mathcal{J}_1(\cdots)\mathsf{H}(\cdots) + \mathcal{J}_0(\cdots)\delta(\cdots)\right.$$

$$\left. + f_0^2 \int_0^t \mathcal{J}_0(fg(x,\tau))\mathsf{H}(\tau - |x|/c)\,d\tau\right]\left(-\frac{1}{m}\cos(mz) + \frac{1}{m}\right). \tag{A.32}$$

For very large $t \gg |x|/c$ the geostrophic balance is expected to hold (i.e. the temporal derivative of the u-velocity vanishes in (A.1)) and the geostrophic wind reads

$$v_g(x,z,t) = f_0^{-1} \partial_x \pi(x,z,t) = \frac{Q_0}{2cf_0} \left[\partial_x \partial_t F(x,t) + f_0^2 \int_0^t \partial_x F(x,\tau)\, d\tau \right] \left(-\frac{1}{m}\cos(mz) + \frac{1}{m} \right)$$

$$= \frac{Q_0}{2cf_0} \left[-\underbrace{\partial_x \left(\frac{f_0\, t}{g(x,t)} \mathcal{J}_1(\cdots) \mathsf{H}(\cdots) \right)}_{\text{I}} + \underbrace{\partial_x \left(\mathcal{J}_0(\cdots)\delta(\cdots) \right)}_{\text{II}} \right.$$

$$\left. + f_0^2 \int_0^t \underbrace{\partial_x \mathcal{J}_0(f_0 g(x,\tau)) \mathsf{H}(\tau - |x|/c)\, d\tau}_{\text{III}} \right] \left(-\frac{1}{m}\cos(mz) + \frac{1}{m} \right), \qquad \text{(A.33)}$$

where the derivatives of the Bessel functions are calculated from the associated series expansion as shown in the following. The series expansion of the Bessel function of first kind and order ν reads From (Lide, 2005, p. A-93, formula 2)

$$\mathcal{J}_\nu(x) = \sum_{k=0}^{\infty} \frac{(-1)^k}{k!(k+\nu)!} \left(\frac{x}{2} \right)^{2k+\nu}$$

Thus, for $F(x,t) = \mathcal{J}_0(f\sqrt{t^2 - a^2})$ with $a = x/c$ reads

$$\partial_t \mathcal{J}_0(f\sqrt{t^2 - a^2}) = \sum_{k=0}^{\infty} \frac{(-1)^k k}{(k!)^2} \left(\frac{f\sqrt{t^2 - a^2}}{2} \right)^{2k-1} \frac{f\, t}{\sqrt{t^2 - a^2}}.$$

Since the first summand $(k = 0)$ vanishes the summation can be carried out from $k = 1$ and an index shift $j = k - 1$ can be performed

$$\partial_t \mathcal{J}_0(f\sqrt{t^2 - a^2}) = \frac{f\, t}{\sqrt{t^2 - a^2}} \sum_{j=0}^{\infty} \frac{(-1)^{j+1}(j+1)}{(j+1)!(j+1)!} \left(\frac{f\sqrt{t^2 - a^2}}{2} \right)^{2j+1}$$

$$= -\frac{f\, t}{\sqrt{t^2 - a^2}} \sum_{j=0}^{\infty} \frac{(-1)^j}{(j+1)!j!} \left(\frac{f\sqrt{t^2 - a^2}}{2} \right)^{2j+1}$$

$$= -\frac{f\, t}{\sqrt{t^2 - a^2}} \mathcal{J}_1(f\sqrt{t^2 - a^2}). \qquad \text{(A.34)}$$

It analogously holds

$$\partial_x \mathcal{J}_0(f\sqrt{t^2 - a^2}) = \frac{f\, x}{c^2\sqrt{t^2 - a^2}} \mathcal{J}_1(f\sqrt{t^2 - a^2}). \qquad \text{(A.35)}$$

The different terms of the geostrophic wind given in (A.33) thus calculate as

$$\text{I} = \frac{f_0\, t\, x}{c^2 g(x,t)^3} \mathcal{J}_1(\cdots) \mathsf{H}(\cdots) - \frac{f_0^2\, t\, x}{2c^2 g(x,t)^2} [\mathcal{J}_0(\cdots) - \mathcal{J}_2(\cdots)] \mathsf{H}(\cdots)$$

$$-\frac{f_0\,t}{cg(x,t)}\mathcal{J}_1(\cdots)\,\delta(\cdots)\,\mathrm{sgn}(x)$$

$$\mathrm{II}=\frac{f_0\,x}{c^2 g(x,t)}\,\mathcal{J}_1(\cdots)\,\delta(\cdots)+\mathcal{J}_0(\cdots)\,\partial_x\delta(\cdots)$$

$$\mathrm{III}=\frac{f_0\,x}{c^2 g(x,t)}\mathcal{J}_1(\cdots)\,\mathsf{H}(\cdots)-c^{-1}\mathcal{J}_0(\cdots)\delta(\cdots)\,\mathrm{sgn}(x)\,.$$

Again, for $t\gg|x|/c$ (i.e. $\mathsf{H}(\cdots)=1$; $\delta(\cdots)=0$) the geostrophic wind reads

$$v_g(x,z,t)=\frac{Q_0}{2cf_0}\left[-\frac{f_0\,t\,x}{c^2 g(x,t)^3}\,\mathcal{J}_1(\cdots)+\frac{f_0^2\,t\,x}{2c^2 g(x,t)^2}[\mathcal{J}_0(\cdots)-\mathcal{J}_2(\cdots)]\right.$$

$$\left.+f_0^2\left(\int_0^t\frac{f_0\,x}{c^2 g(x,t)}\mathcal{J}_1(\cdots)\,\mathsf{H}(\cdots)-c^{-1}\mathcal{J}_0(\cdots)\delta(\cdots)\,\mathrm{sgn}(x)\,d\tau\right)\right]$$

$$\left(-\frac{1}{m}\cos(mz)+\frac{1}{m}\right)\tag{A.36}$$

and with

$$-\frac{f_0^2}{c}\int_0^t\mathcal{J}_0(\cdots)\delta(\cdots)\,\mathrm{sgn}(x)\,d\tau=-\frac{f_0^2}{c}\mathsf{H}(\cdots)\,\mathrm{sgn}(x)\tag{A.37}$$

the solution for $v_g(x,z,t)$ reads

$$v_g(x,z,t)=\frac{Q_0}{2c}\left[-\frac{t\,x}{c^2 g(x,t)^3}\,\mathcal{J}_1(\cdots)+\frac{f_0\,t\,x}{2c^2 g(x,t)^2}[\mathcal{J}_0(\cdots)-\mathcal{J}_2(\cdots)]\right.$$

$$\left.+f_0^2\int_0^t\frac{x}{c^2 g(x,t)}\mathcal{J}_1(\cdots)\mathsf{H}(\cdots)\,d\tau-\frac{f_0}{c}\mathsf{H}(\cdots)\,\mathrm{sgn}(x)\right]$$

$$\left(-\frac{1}{m}\cos(mz)+\frac{1}{m}\right)\,.\tag{A.38}$$

The full expression under the integral cannot be evaluated analytically and has to be approximated.

Appendix B

List of Abbreviations

ALADIN	Aire Limitée Adaptation Dynamique Développement International
CAPE	Convective Available Potential Energy
COAMPS	Coupled Ocean-Atmosphere Mesoscale Prediction System
COSMO	Consortium of Small-Scale modelling
CTRL	Control simulations
DTE	Difference Total Energy
diDTE	Domain integrated Difference Total Energy
DWD	German National Meteorological Service
GA	Geostrophic Adjustment
GASP	Global Atmospheric Sampling Program
GCM	General Circulation Model
IGW	Inertia-Gravity Wave
MOZAIC	Measurement of Ozone and Water Vapor by Airbus In-Service Aircraft
MPAS	Model for Prediction Across Scales
MSG	Meteosat Second Generation
NWP	Numerical Weather Prediction
ODE	Ordinary Differential Equation
PDE	Partial Differential Equation
PERT	Perturbed simulations
ppbv	Parts per billion by volume
TROP	Tropospheric height range ($8.5 - 10.5$ km)
RMS	Root-Mean-Square
Ro	Rossby number
SCB	Stochastic Convective Backscatter
SEVIRI	Spinning Enhanced Visible and InfraRed Imager

| SKEB | Stochastic Kinetic Energy Backscatter |
| STRAT | Stratospheric height range ($16 - 18$ km) |

Appendix C

List of Symbols

A	Area
α	Proportionality factor between coarse-grained vorticity and precipitation
b'	Buoyancy perturbation
$\mathcal{B}$	Characteristic buoyancy scale
$\mathcal{B}_r$	Characteristic buoyancy scale in radially-symmetric geometry
$\tilde{B}_m$	Amplitude of buoyancy perturbation with vertical wavenumber m
$\tilde{\beta}_m$	Laplace transform of $\tilde{B}_m$
$\tilde{b}_m^{\mathrm{b}}$	Summand of the buoyancy solution associated with balanced flow
$\tilde{b}_m^{\mathrm{dt}}$	Summand of the buoyancy solution associated with discontinuous transition
$\tilde{b}_m^{\mathrm{igw}}$	Summand of the buoyancy solution associated with inertia-gravity wave component
C	Circulation
$\mathcal{C}_r$	Characteristic scale of balanced geostrophic circulation in radially-symmetric geometry
c_m	Gravity wave speed of mode with vertical wavenumber m
c_p	Heat capacity of dry air at constant pressure
c_v	Heat capacity of dry air at constant volume
$\delta\chi$	Difference of field χ between perturbed and control simulation
$\partial_\chi^n A$	n-th order partial derivative of field A with respect to χ
$\delta(\cdot)$	Dirac-delta function
d_t	Total derivative $d_t = \partial_t + \mathbf{v} \cdot \nabla$

D	Horizontal divergence
D^ψ	y-derivative of spectrum of stream function
D^ϕ	y-derivative of spectrum of velocity potential
$\mathcal{E}$	Fraction of divergent of kintic energy
E_D	One-dimensional power-spectrum of divergent energy
E_K	One-dimensional power-spectrum of kinetic energy
E_L	One-dimensional power-spectrum of along-track energy
E_R	One-dimensional power-spectrum of rotational energy
E_T	One-dimensional power-spectrum of across-track energy
$E_{D,R}^B$	One-dimensional power-spectrum of divergent and rotational energy calculated from the *Bühler*-method
$E_{D,R}^B$	One-dimensional power-spectrum of divergent and rotational energy calculated from the *Lindborg*-method
$(\mathbf{e}_x, \mathbf{e}_y, \mathbf{e}_z)$	Unit vectors of the three-dim. cartesian coordinate system
$\exp(\cdot)$	Exponential function
f	Coriolis parameter
f_0	Coriolis parameter with midlatitudinal value $f_0 = 1.03 \cdot 10^{-4}\mathrm{s}^{-1}$
$F(s)$	Inverse Laplace-transform of function $f(t)$
g	Gravitational acceleration
γ_∞	Circulation at infinity of a single cloud normalized by its total heating
H	Characteristic vertical scale
$\mathsf{H}(\cdot)$	Heaviside-function
$\mathcal{H}_j^S$	Struve-function of order j
H_{Trop}	Height of the troposphere
$\mathcal{J}_j(\cdot)$	Bessel function of first kind and order j
k	Wavenumber
$\mathcal{K}_j(\cdot)$	Modified Bessel function of second kind and order j
L	Large scales
l	Wavenumber
l_v	Specific heat of vaporization
$\mathcal{L}^{-1}\{\cdot\}$	Inverse Laplace transform
$\mathcal{L}_h$	Characteristic horizontal length scale
$\mathcal{L}_v$	Characteristic vertical length scale
m	Vertical integer wavenumber of forcing

M	Medium scales
N	Brunt-Väisälä-frequency
N_{eff}	Effective degrees of freedom
N_x, N_y	Number of gridpoints in x- and y-direction
∇	Horizontal gradient operator
ω	Frequency of inertia-gravity waves
p	Along-track wavenumber
q	Across-track wavenumber
R_d	First baroclinic Rossby radius of deformation
R_{dd}	Two-point correlation function of divergent velocity
R_{ll}	Two-point correlation function of longitudinal velocity
R_{rr}	Two-point correlation function of rotational velocity
R_{tt}	Two-point correlation function of transversal velocity
t	Time
$\mathcal{T}$	Characteristic time scale
t_{GA}	Characteristic temporal scale of the geostrophic adjustment process
T_p	Predictability time
T_0	Constant reference temperature
$\tilde{t}_r, \tilde{\tau}_r$	Non-dimensional retarded times
$\mathcal{U}$	Characteristic horizontal velocity scale
$\mathcal{V}$	Characteristic horizontal velocity scale
$\mathcal{V}_r$	Characteristic horizontal velocity scale in radially-symmetric geometry
$\boldsymbol{v}_h$	Horizontal wind field
$\boldsymbol{v}'$	Three-dimensional perturbation wind vector with components (u', v', w')
$\boldsymbol{v}_{h,D}$	Divergent component of horizontal wind
$\boldsymbol{v}_{h,R}$	Rotational component of rotational wind
π'	Scaled pressure perturbation
P	Rain rate at ground
$\overline{P}$	Coarse-grained rain rate at ground
$\mathcal{P}$	Characteristic pressure scale
ψ	Stream function
ϕ	Velocity potential
q_i	Total buoyancy source of cloud i
Q	Buoyancy source

Q_0	Amplitude of buoyancy forcing
Q_h	Diabatic heating
$Q_{h,tot}$	Total diabatic heating
ρ	Density
ρ_0	Constant reference value for density
$\hat{\rho}$	Background vertical profile of density
ρ'	Density fluctuations around constant value and background profile
S	Small scales
V	Volume
$\mathcal{W}$	Characteristic vertical velocity scale
x_{GA}	Characteristic spatial scale of the geostrophic adjustment process
z	Height
ζ	Vertical vorticity
$\overline{\zeta}$	Coarse-grained vertical vorticity
$\tilde{\zeta}_m^{g,b}$	Balanced geostrophic vorticity
$\mathcal{Z}_r$	Characteristic scale of balanced geostrophic vorticity in radially-symmetric geometry
$\tilde{Z}_m^{g,b}$	Balanced geostrophic circulation

Bibliography

Abramowitz, M. and Stegun, I. A. (1964). *Handbook of mathematical functions*. U.S. Department of Commerce, National Bureau of Standards.

Achatz, U., Ribstein, B., Senf, F., and Klein, R. (2017). The interaction between synoptic-scale balanced flow and a finite-amplitude mesoscale wave field throughout all atmospheric layers: Weak and moderately strong stratification. *Quart. J. Roy. Meteor. Soc.*, 143:342–361.

Anthes, R. A. (1986). The general question of predictability. In Ray, P. S., editor, *Mesoscale Meteorology and Forecasting*, pages 636–656. Amer. Meteor. Soc.

Anthes, R. A., Kuo, Y. H., Baumhefner, D. P., and Errico, R. P. (1985). Predictability of mesoscale atmospheric motions. *Advances in Geophysics*, 28B:159–202.

Augier, P. and Lindborg, E. (2013). A new formulation of the spectral energy budget of the atmosphere, with application to two high-resolution general circulation models. *J. Atmos. Sci.*, 70:2293–2308.

Bacmeister, J. T., Eckermann, S. D., Newman, P. A., Lait, L., Chan, K. R., Loewenstein, M., Proffitt, M. H., and Gary, B. L. (1996). Stratospheric horizontal wavenumber spectra of winds, potential temperature, and atmospheric tracers observed by high-altitude aircraft. *J. Geophys. Res.*, 101:9441–9470.

Baddour, N. (2009). Operational and convolution properties of two-dimensional Fourier transforms in polar coordinates. *J. Opt. Soc. Am. A*, 26:1767–1777.

Baldauf, M., Seifert, A., Förstner, J., Majewski, D., Raschendorfer, M., and Reinhardt, T. (2011). Operational convective-scale numerical weather prediction with the COSMO model: Description and sensitivities. *Mon. Wea. Rev.*, 139:3887–3905.

Balwada, D., LaCasce, J. H., and Speer, K. G. (2016). Scale-dependent distribution of kinetic energy from surface drifters in the gulf of Mexico. *Geophys. Res. Lett.*, 43:10856–10863.

Bauer, P., Thorpe, A., and Brunet, G. (2015). The quiet revolution of numerical weather prediction. *Nature*, 525:47–55.

Bierdel, L., Friederichs, P., and Bentzien, S. (2012). Spatial kinetic energy spectra in in the convection-permitting limited-area NWP model COSMO-DE. *Meteor. Z.*, 21:245–258.

Bierdel, L., Snyder, C., Park, S.-H., and Skamarock, W. C. (2016). Accuracy of rotational and divergent kinetic energy spectra diagnosed from flight track winds. *J. Atmos. Sci.*, 73:3273–3286.

Billant, P. and Chomaz, J. (2000). Experimental evidence for a new instability of a vertical columnar vortex pair in a strongly stratified fluid. *J. Fluid. Mech.*, 418:167–188.

Bischof, M. (2011). Ensemble simulations of convective storms. M.S. thesis, Institute for Atmospheric and Climatic Sciences at Swiss Federal Institute of Technology, Zürich, Switzerland.

Bjerknes, V. (1904). Das Problem der Wettervorhersage, betrachtet vom Standpunkte der Mechanik und der Physik. *Meteor. Z.*, 21:1–7.

Blažica, V., Žagar, N., Strajnar, B., and Cedilnik, J. (2013). Rotational and divergent kinetic energy in the mesoscale model ALADIN. *TELLUS A*, 65:18918.

Blumen, W. (1972). Geostrophic adjustment. *Rev. Geophys. Space Phys.*, 10:485–528.

Boer, G. and Shepherd, T. (1983). Large-scale two-dimensional turbulence in the atmosphere. *J. Atmos. Sci.*, 40:164–184.

Bott, A. and Zdunkowski, W. (2003). *Dynamics of the atmosphere*. Cambridge University Press.

Bretherton, C. S. and Smolarkiewicz, P. K. (1989). Gravity waves, compensating subsidence and detrainment around cumulus clouds. *J. Atmos. Sci.*, 46:740–759.

Brune, S. and Becker, E. (2013). Indications of stratified turbulence in a mechanistic GCM. *J. Atmos. Sci.*, 70:231–247.

Bühler, O., Callies, J., and Ferrari, R. (2014). Wave-vortex decomposition of one-dimensional ship-track data. *J. Fluid Mech.*, 756:1007–1026.

Bühler, O., Kuang, M., and Tabak, E. G. (2017). Anisotropic Helmholtz- and wave-vortex decomposition of one-dimensional spectra. *J. Fluid Mech.*, 815:361–387.

Buizza, R., Miller, M., and Palmer, T. N. (1999). Stochastic representation of model uncertainty in the ECMWF ensemble prediction systems. *Quart. J. Roy. Meteor. Soc.*, 125:2887–2908.

Burgess, B. H., Erler, A. R., and Shepherd, T. G. (2013). The troposphere-to-stratosphere transition in kinetic energy spectra and nonlinear spectral fluxes as seen in ECMWF analyses. *J. Atmos. Sci.*, 70:669–687.

Callies, J., Bühler, O., and Ferrari, R. (2016). The dynamics of mesoscale winds in the upper troposphere and lower stratosphere. *J. Atmos. Sci.*, 73:4853–4872.

Callies, J., Ferrari, R., and Bühler, O. (2014). Transition from geostrophic turbulence to inertia-gravity waves in the atmospheric energy spectrum. *Proc. Natl. Acad. Sci. (USA)*, 111:17033–17038.

Chagnon, J. M. and Bannon, P. R. (2001). Hydrostatic and geostrophic adjustment in a compressible atmosphere: Initial response and final equilibrium to an instantaneous localized heating. *J. Atmos. Sci.*, 58:3776–3792.

Chagnon, J. M. and Bannon, P. R. (2005a). Wave response during hydrostatic and geostrophic adjustment. Part I: Transient dynamics. *J. Atmos. Sci.*, 62:1311–1329.

Chagnon, J. M. and Bannon, P. R. (2005b). Wave response during hydrostatic and geostrophic adjustment. Part II: Potential vorticity conservation and energy partitioning. *J. Atmos. Sci.*, 62:1330–1345.

Charney, J. G. (1948). On the scale of atmospheric motions. *Geof. Pub.*, 17:1–71.

Charney, J. G. (1971). Geostrophic turbulence. *J. Atmos. Sci.*, 28:1087–1095.

Cho, J. Y. N. and Lindborg, E. (2001). Horizontal velocity structure functions in the upper troposphere and lower stratosphere. 1. Observations. *J. Geophys. Res.*, 106:10,223 – 10,232.

Cho, J. Y. N., Newell, R. E., and Barrick, J. D. (1999). Horizontal wavenumber spectra of winds, temperature, and trace gases during the Pacific Exploratory Missions: 2. Gravity waves, quasi-two-dimensional turbulence, and vortical modes. *J. Geophys. Res.*, 104:16,297 – 16,308.

Clauset, A., Shalizi, C. R., and Newman, M. E. J. (2009). Power-law distributions in empirical data. *SIAM Review*, 51:4:661–703.

Craig, G., Richard, E., Richardson, D., Burridge, D., Jones, S., Atger, F., Ehrendorfer, M., Heikinheimo, M., Hoskins, B., Lorenc, A., Methven, J., Paccagnella, T., Pailleux, J., Rabier, F., Roulson, M., Saunders, R., Swinbank, R., Tibaldi, S., and Wernli, H. (2010). Weather Research in Europe. A THORPEX European Plan. *WMO/TD-No. 1513, WWRP/THORPEX No. 14.*

Dewan, E. (1994). The saturated-cascade model for atmospheric gravity wave spectra, and the wavelength-period (W-P) relations. *Geophys. Res. Lett.*, 21:817–820.

Dewan, E. (1997). Saturated-cascade similitude theory of gravity wave spectra. *J. Geophys. Res.*, 102:29,799 –29,817.

Dewan, E. M. (1979). Stratospheric wave spectra resembling turbulence. *Science*, 204:832–835.

Durran, D. R. and Gingrich, M. (2014). Atmospheric predictability: Why butterflies are not of practical importance. *J. Atmos. Sci.*, 71:2476–2488.

Durran, D. R., Reinecke, P. A., and Doyle, J. D. (2013). Large-scale errors and mesoscale predictability in pacific northwest snowstorms. *J. Atmos. Sci.*, 70:1470–1487.

Durran, D. R. and Weyn, J. A. (2016). Thunderstorms don't get butterflies. *Bull. Amer. Meteor. Soc.*, 97:237–243.

Ehrendorfer, M. and Errico, R. M. (1995). Mesoscale predictability and the spectrum of optimal perturbations. *J. Atmos. Sci.*, 52:3475–3500.

Emanuel, K. A. (1986). Overview and definition of mesoscale meteorology. In Ray, P. S., editor, *Mesoscale Meteorology and Forecasting*, pages 1–17. Amer. Meteor. Soc.

Errico, R. M. (1985). Spectra computed from a limited area grid. *Mon. Wea. Rev.*, 113:1554–1562.

Fang, X. and Kuo, Y.-H. (2015). A new generic method for quantifying the scale predictability of the fractal atmosphere: Applications to model verification. *J. Atmos. Sci.*, 72:1667–1688.

Fiedler, F. and Panofsky, H. A. (1970). Atmospheric scales and spectral gaps. *Bulletin of the American Meteorological Society*, 51(12):1114–1120.

Fischer, C., Montmerle, T., Berre, L., Auger, L., and Stefânescu, S. E. (2005). An overview of the variational assimilation in the ALADIN/France numerical weather-prediction system. *Quart. J. Roy. Meteor. Soc.*, 131:3477–3492.

Frehlich, R. and Sharman, R. (2008). The use of structure functions and spectra from numerical model output to determine effective model resolution. *Mon. Wea. Rev.*, 136:1537–1553.

Frisch, U. (2004). *Turbulence*. Cambridge University Press.

Fritts, D. C. and Alexander, M. J. (2003). Gravity wave dynamics and effects in the middle atmosphere. *Rev. Geophys.*, 41:1/1003–1/1064.

Gage, K. S. (1979). Evidence for a $k^{-5/3}$ law inertial range in mesoscale two-dimensional turbulence. *J. Atmos. Sci.*, 36:1950–1954.

Gage, K. S. and Nastrom, G. D. (1985). On the spectrum of atmospheric velocity fluctuations seen by MST/ST radar and their interpretation. *Radio. Sci.*, 2:1339–1347.

Garrett, C. and Munk, W. (1972). Space-time scales of internal waves. *Geophys. Fluid Dyn.*, 2:225–264.

Garrett, C. and Munk, W. (1975). Space-time scales of internal waves: A progress report. *J. Geophys. Res.*, 80:291–297.

Gill, A. E. (1982). *Atmosphere-Ocean Dynamics*, volume 30. AcademicPress.

Gkioulekas, E. (2006). *A theoretical study of the cascades of 3D, 2D, and QG turbulence*. PhD thesis, University of Washington.

Gkioulekas, E. and Tung, K. K. (2007). A new proof on net upscale energy cascade in two-dimensional and quasi-geostrophic turbulence. *J. Fluid. Mech.*, 576:173–189.

Gray, M. E. B. (1996). *Geostrophic adjustment following deep convection*. PhD thesis, University of Reading, Department of Meteorology.

Grimshaw, R. (1975). Nonlinear internal gravity waves in a rotating fluid. *J. Fluid Mech.*, 71:497–512.

Hamilton, K., Takahasi, Y. O., and Ohfuchi, W. (2008). Mesoscale spectrum of atmospheric motions investigated in a very fine resolution global general circulation model. *J. Geophys. Res.*, 113:D18110.

Hodur, R. M. (1997). The Naval Research Laboratorys Coupled Ocean/Atmosphere Mesoscale Prediction System (COAMPS). *Mon. Wea. Rev.*, 125:1414–1430.

Hohenegger, C. and Schär, C. (2007). Predictability and error growth dynamics in cloud-resolving models. *J. Atmos. Sci.*, 64:4467–4478.

Holton, J. R. (2004). *An introduction to dynamic meteorology*, volume 4. Elsevier Academic Press.

I. N. Bronstein, K. A. Semendjajew, G. M. and Mühlig, H. (2001). *Taschenbuch der Mathematik*, volume 5. Harri Deutsch.

Keil, C., Heinlein, F., and Craig, G. C. (2014). The convective adjustment time-scale as indicator of predictability of convective precipitation. *Quart. J. Roy. Meteor. Soc.*, 140:480–490.

Khairoutdinov, M. and Emanuel, K. (2013). Rotating radiative-convective equilibrium simulated by a cloud-resolving model. *J. Adv. Model. Earth Syst.*, 5:816–825.

Klein, R. (2009). Scale-dependent models of atmospheric flow. *Annu. Rev. Fluid Mech.*, 42:249–274.

Kolmogorov, A. N. (1941). The local structure of turbulence in in-compressible viscous fluids for very large reynolds numbers. *Dokl. Akad. Nauk. SSSR*, 30:301–305.

Koshyk, J. N., Boville, B. A., Hamilton, K., Manzini, E., and Shibata, K. (1999). Kinetic energy spectrum of horizontal motions in middle-atmosphere models. *J. Geophys. Res.*, 104:27,177–27,190.

Koshyk, J. N. and Hamilton, K. (2001). The horizontal kinetic energy spectrum and spectral budget simulated by a high-resolution troposphere-stratosphere-mesosphere GCM. *J. Atmos. Sci.*, 58:1329–1348.

Kraichnan, R. H. (1967). Inertial ranges in two-dimensional turbulence. *Physics of Fluids*, 10:1417–1423.

Lane, T. P. and Reeder, M. J. (2001). Convectively generated gravity waves and their effect on the cloud environment. *J. Atmos. Sci.*, 58:2427–2440.

Lange, H. and Craig, G. C. (2014). The impact of data assimilation length scales on analysis and prediction of convective storms. *Mon. Wea. Rev.*, 142:3781–3808.

Lange, H., Craig, G. C., and Janjić, T. (2017). Characterizing noise and spurious convection in convective data assimilation. Manuscript submitted for publication.

Leith, C. E. and Kraichnan, R. H. (1972). Predictability of turbulent flows. *J. Atmos. Sci.*, 29:1041–1058.

Leoncini, G., Plant, R. S., Gray, S. L., and Clark, P. A. (2010). Perturbation growth at the convective scale for CSIP IOP18. *Quart. J. Roy. Meteor. Soc.*, 136:653–670.

Lide, D. R. (2005). *CRC Handbook of Chemistry and Physics, Internet Version 2005.* CRC Press, Boca Raton, FL.

Ligda, M. G. H. (1951). Radar storm observations. In *Compendium of meteorology*, pages 1265–1282. Amer. Meteor. Soc., Boston.

Lilly, D. K. (1972). Numerical simulation studies of two-dimensional turbulence: II. Stability and predictability studies. *Geophys. Astrophys. Fluid Dyn.*, 4:1–28.

Lilly, D. K. (1983). Stratified turbulence and the mesoscale variability of the atmosphere. *J. Atmos. Sci.*, 40:749–761.

Lin, Y.-L. (2007). *Mesoscale dynamics.* Cambridge University Press.

Lindborg, E. (1999). Can the atmospheric kinetic energy spectrum be explained by two-dimensional turbulence? *J. Fluid Mech.*, 388:259–288.

Lindborg, E. (2006). The energy cascade in a strongly stratified fluid. *J. Fluid Mech.*, 550:207–242.

Lindborg, E. (2007). Horizontal wavenumber spectra of vertical vorticity and horizontal divergence in the upper troposphere and lower stratosphere. *J. Atmos. Sci.*, 64 (3):1017–1025.

Lindborg, E. (2015). A Helmholtz decomposition of structure functions and spectra calculated from aircraft data. *J. Fluid Mech.*, 762:R4.

Liu, C. and Moncrieff, M. W. (2004). Effects of convectively generated gravity waves and rotation on the organization of convection. *J. Atmos. Sci.*, 61:2218–2227.

Lorenz, E. (1963). Deterministic nonperiod flow. *J. Atmos. Sci.*, 20:130–141.

Lorenz, E. (1969). The predictability of a flow which possesses many scales of motion. *Tellus*, 21:289–307.

Mapes, B. E. (1993). Gregarious tropical convection. *J. Atmos. Sci.*, 50:2026–2037.

Marenco, A., Thouret, V., Nédélec, P., Smit, H., Helten, M., Kley, D., Karcher, F., Simon, P., Law, K., Pyle, J., Poschmann, G., Wrede, R. V., Hume, C., and Cook, T. (1998). Measurement of ozone and water vapor by airbus in-service aircraft: The MOZAIC airborne program, an overview. *J. Geophys. Res.*, 103:2156–2202.

Markowski, P. and Richardson, Y. (2010). *Mesoscale Meteorology in Midlatitudes.* John Wiley & Sons, Ltd.

Melhauser, C. and Zhang, F. (2012). Practical and intrinsic predictability of severe and convective weather at the mesoscales. *J. Atmos. Sci.*, 69:3350–3371.

Merilees, P. E. and Warn, T. (1972). The resolution implications of geostrophic turbulence. *J. Atmos. Sci.*, 29:990–991.

Nastrom, G. D. and Gage, K. S. (1983). A first look at wavenumber spectra from GASP data. *Tellus A*, 35A(5):383–388.

Nastrom, G. D. and Gage, K. S. (1985). A climatology of atmospheric wavenumber spectra of wind and temperature observed by commercial aircraft. *J. Atmos. Sci.*, 42:950–960.

Nastrom, G. D., Gage, K. S., and Jasperson, W. (1984). Kinetic energy spectrum of large- and mesoscale atmospheric processes. *Nature*, 310:36–38.

Neggers, R. A. J., Jonker, H. J. J., and Siebesma, A. P. (2002). Size statistics of cumulus cloud populations in large-eddy simulations. *J. Atmos. Sci.*, 60:1060–1074.

Nicholls, M. E. and Pielke, R. A. (2000). Thermally induced compression waves and gravity waves generated by convective storms. *J. Atmos. Sci.*, 57:3251–3271.

Nicholls, M. E., Pielke, R. A., and Cotton, W. R. (1991). Thermally forced gravity waves in an atmosphere at rest. *J. Atmos. Sci.*, 48:1869–1884.

Nolan, D. S., Rappin, E. D., and Emanuel, K. A. (2007). Tropical cyclogenesis sensitivity to environmental parameters in radiative-convective equilibrium. *Quart. J. Roy. Meteor. Soc.*, 133:2085–2107.

Obukhov, A. M. (1949). Structure of the temperature field in turbulent flows. *Izv. Akad. Nauk SSSR, Ser. Geofiz.*, 13:58–69.

Orlanski, I. (1975). A rational subdivision of scales for atmospheric processes. *Bull. Amer. Meteor. Soc.*, 56(5).

Palmer, T. N., Döring, A., and Seregin, G. (2014). The real butterfly effect. *Nonlinearity*, 27:R123–R141.

Poincaré, H. (1914). *Science and Method.* Cosimo Classics.

Pope, S. B. (2000). *Turbulent Flows.* Cambridge University Press.

Raymond, D. J. (1986). Prescribed heating of a stratified atmosphere as a model for moist convection. *J. Atmos. Sci.*, 43:1101–1111.

Raymond, D. J. (1987). A forced gravity wave model of self-organising convection. *J. Atmos. Sci.*, 44:3528–3543.

Ricard, D., Lac, C., Riette, S., Legrand, R., and Mary, A. (2013). Kinetic energy spectra characteristics of two convection-permitting limited-area models AROME and Meso-NH. *Quart. J. Roy. Meteor. Soc.*, 139:1327–1341.

Richardson, L. F. (1922). *Weather Prediction by numerical process*. Cambridge University Press.

Riley, J. J. and Lelong, M.-P. (2000). Fluid motions in the presence of strong stable stratification. *Ann. Rev. Fluid. Mech.*, 32:613–657.

Riley, J. J. and Lindborg, E. (2008). Stratified turbulence: A possible interpretation of some geophysical turbulence measurements. *J. Atmos. Sci.*, 65:2416–2424.

Rocha, C. B., Chereskin, T. K., and Gille, S. T. (2016). Mesoscale to submesoscale wavenumber spectra in the Drake passage. *J. Phys. Oceanogr.*, 46:601–620.

Rodwell, M. J., Magnusson, L., Bauer, P., Bechtold, P., Bonavita, M., Cardinali, C., Diamantakis, M., Earnshaw, P., Garcia-Mendez, A., Isaksen, L., Källen, E., Klocke, D., Lopez, P., McNally, T., Persson, A., Prates, F., and Wedi, N. (2013). Characteristics of occasional poor medium-range weather forecasts for Europe. *Bull. Amer. Meteor. Soc.*, 94:1393–1405.

Rossby, C.-G. (1937). On the mutual adjustment of pressure and velocity distributions in certain simple current systems, 1. *J. Mar. Res.*, 1:15–28.

Rossby, C.-G. (1938). On the mutual adjustment of pressure and velocity distributions in certain simple current systems, 2. *J. Mar. Res.*, 1:239–263.

Rotunno, R. and Snyder, C. (2008). A generalization of Lorenz's model for the predictability of flows with many scales of motion. *J. Atmos. Sci.*, 65:1063–1076.

Ruzmaikin, A., Lawrence, J., and Cadavid, C. (2003). A simple model of stratospheric dynamics including solar variability. *J. Climate*, 16:1593–1600.

Schubert, W. H., Hack, J. J., Dias, P. L. S., and Hulton, S. R. (1980). Geostrophic adjustment in an axisymmetric vortex. *J. Atmos. Sci.*, 143:1464–1484.

Selz, T. and Craig, G. C. (2015a). Simulation of upscale error growth with a stochastic convection scheme. *Geophys. Res. Lett.*, 42:3056–3062.

Selz, T. and Craig, G. C. (2015b). Upscale error growth in a high-resolution simulation of a summertime weather event over Europe. *Mon. Wea. Rev.*, 143:813–827.

Shutts, G. J. (2005). A kinetic energy backscatter algorithm for use in ensemble prediction systems. *Quart. J. Roy. Meteor. Soc.*, 131:3079–3102.

Shutts, G. J. (2015). A stochastic convective backscatter scheme for use in ensemble prediction systems. *Quart. J. Roy. Meteor. Soc.*, 141:2602–2616.

Shutts, G. J. and Gray, M. E. B. (1994). A numerical modelling study of the geostrophic adjustment process following deep convection. *Quart. J. Roy. Meteor. Soc.*, 120:1145–1178.

Skamarock, W. C. (2004). Evaluating mesoscale NWP models using kinetic energy spectra. *Mon. Wea. Rev.*, 132:3019–3032.

Skamarock, W. C., Klemp, J. B., Duda, M. G., Fowler, L. D., Park, S.-H., and Ringler, T. (2012). A multiscale nonhydrostatic atmospheric model using centroidal Voronoi tesselations and C-grid staggering. *Mon. Wea. Rev.*, 140:3090–3105.

Skamarock, W. C., Park, S.-H., Klemp, J. B., and Snyder, C. (2014). Atmospheric kinetic energy spectra from global high-resolution nonhydrostatic simulations. *J. Atmos. Sci.*, 71:4369–4381.

Stumpf, M. P. H., Michael, and Porter, M. A. (2012). Critical truths about power laws. *Science*, 335(6069):665–666.

Sun, Y. Q., Rotunno, R., and Zhang, F. (2017). Contributions of moist convection and internal gravity waves to building the atmospheric -5/3 kinetic energy spectra. *J. Atmos. Sci.*, 74:185–201.

Sun, Y. Q. and Zhang, F. (2016). Intrinsic versus practical limits of atmospheric predictability and the significance of the butterfly effect. *J. Atmos. Sci.*, 73:1419–1438.

Tan, Z.-M., Zhang, F., Rotunno, R., and Snyder, C. (2004). Mesoscale predictability of moist baroclinic waves: Experiments with parameterized convection. *J. Atmos. Sci.*, 61:1794–1804.

Teubler, F. and Riemer, M. (2016). Dynamics of Rossby wave packets in a quantitative potential vorticity-potential temperature framework. *J. Atmos. Sci.*, 73:1063–1081.

Tulloch, R. and Smith, K. S. (2006). A theory for the atmospheric energy spectrum: Depth-limited temperature anomalies at the tropopause. *Proc. Natl. Acad. Sci. USA*, 103:14690–14694.

Tung, K. K. and Orlando, W. W. (2003). The k^{-3} and $k^{-5/3}$ energy spectrum of atmospheric turbulence: Quasigeostrophic two-level model simulation. *J. Atmos. Sci.*, 60:824–835.

Tung, K. K. and Welch, W. T. (2001). Remarks on Charney's note on geostrophic turbulence. *J. Atmos. Sci.*, 58:2009–2012.

Vadas, S. L. and Fritts, D. C. (2001). Gravity wave radiation and mean responses to local body forces in the atmosphere. *J. Atmos. Sci.*, 58:2249–2279.

Vallis, G. K. (2006). *Atmospheric and Oceanic Fluid Dynamics*, volume 6. Cambridge University Press.

VanZandt, T. E. (1982). A universal spectrum of buoyancy waves in the atmosphere. *Geophys. Res. Lett.*, 9:575–578.

Vincent, R. A. and Eckermann, S. D. (1990). VHF radar observations of mesoscale motions in the atmosphere: Evidence for gravity wave Doppler shifting. *Radio. Sci.*, 25:1019–1037.

Waite, M. L. and Snyder, C. (2013). Mesoscale energy spectra of moist baroclinic waves. *J. Atmos. Sci.*, 70:1242–1256.

Wang, X. and Shen, S. S. (1999). Estimation of spatial degrees of freedom of a climate field. *J. Climate*, 12:1280–1291.

Weyn, J. A. and Durran, D. R. (2017). The dependence of the predictability of mesoscale convective systems on the horizontal scale and amplitude of initial errors in idealized simulations. Early online release doi: 10.1175/JAS-D-17-0006.1.

Zaho, G. and Girolamo, L. D. (2007). Statistics on the macrophysical properties of trade wind cumuli over the tropical western Atlantic. *J. Geophys. Res.*, 112:D10204.

Zhang, F., Bei, N., Rotunno, R., Snyder, C., and Epifanio, C. C. (2007). Mesoscale predictability of moist baroclinic waves: Convection-permitting experiments and multistage error growth dynamics. *J. Atmos. Sci.*, 64:3579–3594.

Zhang, F., Snyder, C., and Rotunno, R. (2002). Mesoscale predictability of the "suprise" snowstorm of 24-25 January 2000. *Mon. Wea. Rev.*, 130:1617–1632.

Zhang, F., Snyder, C., and Rotunno, R. (2003). Effects of moist convection on mesoscale predictability. *J. Atmos. Sci.*, 60:1173–1185.

Zhu, H. and Thorpe, A. (2006). Predictability of extratropical cyclones: The influence of initial condition and model uncertainties. *J. Atmos. Sci.*, 63:1483–1497.

Acknowledgments

First, I want to thank my supervisor George Craig for leading and accompanying me through this initially slightly adventurous project. Your utter joy while sciencing has infected and motivated me over these years. Thanks for supporting my stay at NCAR and never getting tired of listening to new insights into mesoscale energy spectra.

Furthermore, I want to thank Bernhard Mayer for co-examining this thesis.

I'd like to thank Tobias Selz for a lot of things. For standing all these years in an office with me, for always taking the time to discuss recent results, for sharing your code and your vast knowledge and helping wherever you can. I'm looking forward to all the fun stuff we're going to work on - Geronimos time has finally come!

I want to thank Chris Snyder for agreeing to supervise me in the framework of ASP and for giving me the possibility to visit NCAR. I learned a lot from you and am looking forward to working together in the future.

I want to particularly thank Audine Laurian, Max Maahn, Kevin Bachmann, Carolin Klinger and Tobias Selz for putting so much effort into proof-reading this thesis. Christian Keil, Christoph Knote and Matthias Sommer are acknowledged for giving helpful advice and always having an open ear. Thanks to Robert Redl for always helping out fast with any computer-related problem.

I'd like to thank the students and employees of MIM, and particularly my office mates Stephan Rasp, Julia Windmiller und Tobias Selz for generating such a positive, pleasant and productive working atmosphere and finding time for off-topic discussions. Special thanks to Barbara Baumann for making me smile by waving at me in the corridor every time I walked past.

Finally, I'd like to thank my family for supporting me without actually knowing what I was doing all those years in Munich. Very special thanks go to you, Cándido. You never got tired of listening to me, supporting and encouraging me. You kept us dancing in the eye.